SCATTERING OF LOW-ENERGY ELECTRONS FROM THE TUNGSTEN (110) SURFACE

A THESIS

Presented to

The Faculty of the Graduate Division

by

Lester Neal Tharp

In Partial Fulfillment

of the Requirements for the Degree

Doctor of Philosophy in the School of Physics

Georgia Institute of Technology

June, 1968

SCATTERING OF LOW-ENERGY

ELECTRONS FROM THE

TUNGSTEN (110) SURFACE

Approved:

Chairman

Date approved by Chairman: 5-15-68

ACKNOWLEDGMENTS

I would like to thank Dr. Edwin J. Scheibner for his patient guidance throughout my career as a student in Physics and especially for his direction and encouragement during the course of the research leading to this dissertation. I would further like to express my appreciation to Drs. H. A. Gersch and J. W. Hooper for their contributions as members of the reading committee and to the faculty of the School of Physics for their instruction and support.

The research forming the basis for this dissertation was carried out as a part of the program entitled "Surface Properties of Magnetic Materials," directed by Dr. Scheibner in the Physical Sciences Division. This program has been supported by the U. S. Atomic Energy Commission under the Metallurgy and Materials Program of the Division of Research. In particular, I would like to thank Dr. D. K. Stevens, the A. E. C. Technical Monitor, whose continued interest in this program has made my research possible.

I would also like to express my gratitude to Mrs. Betty Jaffe for her attention and care in typing the thesis.

TABLE OF CONTENTS

TABLE OF CONTENTS (Continued)

LIST OF TABLES

LIST OF ILLUSTRATIONS

LIST OF ILLUSTRATIONS (Continued)

SUMMARY

The properties of solid surfaces are uniquely important to many areas of solid state physics, and the development of a means for investigating some aspects of surfaces has been one of the main purposes of this study. Experimental techniques used include low-energy electron diffraction and low-energy electron spectroscopy, which involves energy analyses of the back-scattered electrons. Essential to the interpretation of results obtained with these techniques is an understanding of the fundamentals of the interactions of slow electrons with solids; thus, an investigation of the elastic and inelastic scattering processes for the slow electrons has been undertaken. An apparatus has been designed and constructed which can be used to obtain LEED patterns and secondary electron energy distributions from the same surfaces, and the advantages of this combination of techniques have been demonstrated. Finally, this method has been used to study the (110) surface of a tungsten single crystal with the following results: (1) LEED patterns were used to identify previously reported two-dimensional structures for the surface states considered; (2) secondary electron energy distribution curves were obtained for the various surface states and were used with LEED patterns to characterize these states; and (3) the energy distribution curves were explained in terms of interband transitions, plasmon excitations and Auger type transitions.

CHAPTER I

INTRODUCTION

The Problem

The properties of solid surfaces are uniquely important to many areas of solid state physics, but the evaluation of such properties is difficult to achieve because of problems related to the proper characterization of experimental surfaces. Few attempts have been made to establish a correlation between the surface properties measured and the structures and exact compositions of the surfaces; consequently, the results obtained have often been ambiguous, if not contradictory to similar results obtained by other means or in other laboratories. Thus, one of the main objectives of this research has been the development of a technique which can be used to determine the structure and composition of a surface and which can be conveniently coupled with other experiments for the purpose of monitoring the state of a surface while other physical properties are investigated.

Two techniques have been considered in the present work: low-energy electron diffraction (LEED) which involves the elastic scattering of electrons in the energy range of about five to 500 electron volts from well ordered surfaces; and low-energy electron spectroscopy (LEES) which involves energy analyses of the electrons inelastically scattered from these surfaces. LEED can be used to determine the two-dimensional structures of clean single crystal surfaces or surfaces with ordered adsorbed gas layers. However, because of the dependence on a periodic arrangement of atoms at the surface, this technique can not always be used to unambiguously determine whether or not a contaminant is present on the surface, and no information is given concerning the nature of the contaminant. Inelastic scattering processes, on the other hand, do not depend in detail on surface structures, and the energy distributions of the secondary electrons can be used in addition to LEED patterns for the detection and identification of impurities on or near the surface. The data which are made available by this combination of techniques can generally be used to determine the state of a surface, giving information relating to both structure and composition, whereas elastic or inelastic measurements taken independently do not permit such a characterization.

Essential to the interpretation of results obtained with these techniques is an understanding of the fundamentals of the interactions of slow electrons with solids. These interactions have been considered previously from both the standpoints of elastic diffraction and inelastic scattering, but the emphasis has been on the scattering of high-energy electrons in transmission experiments. Of more interest to the present study is the case of low-energy electrons reflected from a surface, and an investigation of some aspects of the elastic and inelastic scattering processes for the slow electrons has been included.

One of the first problems resolved was the design and construction of the experimental apparatus. The instrument which has resulted consists of a post-acceleration type LEED system modified so that both LEED patterns and secondary electron energy distribution curves can be obtained from the same surfaces. Measurements are made in ultra-high vacuum; provisions have been made for obtaining atomically clean surfaces and for admitting ultrapure gases for adsorption studies.

The experimental sample selected for this study was a tungsten single crystal slab, which was cut and polished with flat surfaces parallel to the (110) crystallographic planes. The methods described above were applied to this sample with the following results: (1) LEED patterns were used to identify previously reported two-dimensional structures for the surface states considered; (2) secondary electron energy distribution curves were obtained for the various surface states and were used in conjunction with LEED patterns to characterize these states; and (3) the structure observed in these energy distribution curves was explained in terms of interband type transitions, plasmon excitations and Auger type transitions.

The concepts, methods and results which have been summarized here are dealt with at length in the following sections of this dissertation. Presented in the remainder of the introduction are some of the historical developments in the fields of LEED and secondary emission, as they apply to the present study, and a summary of results obtained in previous investigations of tungsten; also included are some further comments on the combination of techniques as used for surface studies. Some theoretical background is given in the next chapter, considering separately the problems of elastic diffraction, characteristic energy losses and true secondary emission; the emphasis in this discussion is on the case of low-energy electrons reflected from a solid surface. In Chapter III, the apparatus is described including a discussion of instrumental effects and experimental procedures which are now used. The last chapters are concerned with the actual data obtained from tungsten and their interpretation.

Historical Background

Low-Energy Electron Diffraction

Low-energy electron diffraction has been widely accepted as a technique for studying surface reactions and determining the structures of single crystal surfaces. In LEED studies, samples are bombarded by a monochromatic beam of low-energy electrons; the electrons are back-reflected and, if the surfaces are well ordered, coherent diffraction patterns are formed. Because of the slight penetration of these slow electrons, the technique is very sensitive to surface conditions. However, the exact nature of the scattering of electrons in this energy range can not readily be predicted by existing theories. Most efforts have thus far been limited to the determination of the structures of clean surfaces or surfaces with ordered adsorbed gas layers, and relatively little work has been aimed at an understanding of the fundamental interactions involved.

The LEED technique had its beginning as the result of an accident that occurred in the laboratories of the Western Electric Company (now the Bell Telephone Laboratories) in the Spring of 1925.[1,2] At that time C. J. Davisson and L. H. Germer were continuing an investigation of the angular distribution of slow electrons scattered by a target of polycrystalline nickel. A liquid-air bottle exploded during the course of the work when the target was at a high temperature, and the evacuated experimental tube was broken. The hot target was heavily oxidized by the inrushing air, and, when the oxide was later reduced by prolonged heating in hydrogen and vacuum, it was found that the sample surface had recrystallized so that only a few large crystallites were present. The angular distributions of the electrons reflected from the sample after the recrystallization were much more complex than those corresponding to the polycrystalline surface; although the effect was recognized as a crystalline effect, the fact that the electrons were being diffracted as waves was certainly not understood. However, a short time later Davisson, while on a visit to England, learned of L. de Broglie's hypothesis concerning the wave nature of electrons, which had been proposed in 1924; guided by this theory, Davisson and Germer were quickly able to interpret the observed scattering curves in terms of diffraction patterns, experimentally confirming the de Broglie proposal in 1927.[2] The same confirmation was made independently in Britain by Sir George Thompson, and both Thompson and Davisson received the Nobel Prize in Physics for this work.

After so important a beginning, the LEED technique did not continue to receive much emphasis as compared with high-energy electron diffraction, and, except for a few workers (notably Farnsworth[3] at Brown University), little was done with the technique until it was revived and improved by Scheibner at the Bell Telephone Laboratories in 1956.

In the Davisson and Germer apparatus, the emitted electron currents were detected by a collector which could be scanned through all azimuths and angles. The weighted collector was mounted on a track and moved freely under the influence of gravity; the collector could then be made to scan in the one fixed azimuth by changing the attitude of the evacuated and sealed-off experimental chamber. The sample was mounted on a shaft coupled to an off-axis weight; rotation of the chamber about this axis then caused the sample to rotate, and the azimuth relative to the collector could be changed. The system employed by Farnsworth similarly used a Faraday collector which could be moved about the chamber to record the angular distributions of the electrons. This measurement scheme suffered from the disadvantages that details of the diffraction patterns could be obtained only by painstakingly scanning a large solid angle with the collector, and the time required for such measurements was usually so long that the surfaces being studied could change significantly before the pattern could be mapped out. The combination of the poor state of vacuum technology at that time and the laborious method of detecting the diffraction patterns severely limited the usefulness of LEED in these earlier experiments.

Scheibner, being concerned about the influence on the electronic surface states of the atomic arrangements at the surfaces of semiconductor crystals, became interested in LEED as a tool for investigating such surface problems. Using the post-acceleration scheme described by Ehrenberg,[4] he developed the LEED apparatus[5] which has formed the basis for the experimental systems now commonly used. Scheibner's method differed from that described above in that the diffraction patterns were visually displayed by collecting the elastically scattered electrons in a reasonably large solid angle on a fluorescent screen rather than using a Faraday collector to obtain the angular distributions. Several advantages were realized by this design: the data obtained was now more analogous to x-ray data in that a larger number of reflections could be observed simultaneously; the constant display of a large portion of the diffraction pattern made it possible to follow dynamic changes in the surfaces which influenced these patterns; reflections not along the major azimuths are displayed which might be missed in experiments involving scans along these azimuths.

One of the experimental LEED tubes used by Scheibner is shown in Figure 1(a). The tube was constructed of glass, and the optics consisted of an electron gun, two planar mesh grids, and a fluorescent screen deposited on glass. The patterns could be viewed or photographed through a side window by means of a mirror oriented at 45 degrees to the fluorescent screen. The operation of this instrument can be understood by considering the schematic diagram of Figure 1(b). Electrons emitted from the cathode are accelerated to about 1000 ev, focused into a well-defined beam, and then decelerated to their final low energy in the drift tube. The beam strikes the crystal surface at normal incidence, and a portion of the back-reflected electrons are collected by the fluorescent screen. The first grid is operated at the same potential as the crystal and the drift tube so that the diffracted electrons move in a field-free space. The second grid is operated at about cathode potential in order to eliminate from the observed pattern most of the electrons which are inelastically scattered. Between the last grid and the fluorescent screen is a large positive potential; electrons which have sufficient energy to overcome the suppressor potential are then accelerated to excite the phosphor on the fluorescent screen.

Subsequent redesigns of the LEED apparatus have resulted in only minor improvements. The experimental tube was changed so that the patterns could be viewed directly from the front side of the fluorescent screen rather than through the 45 degree mirror.[6] The planar

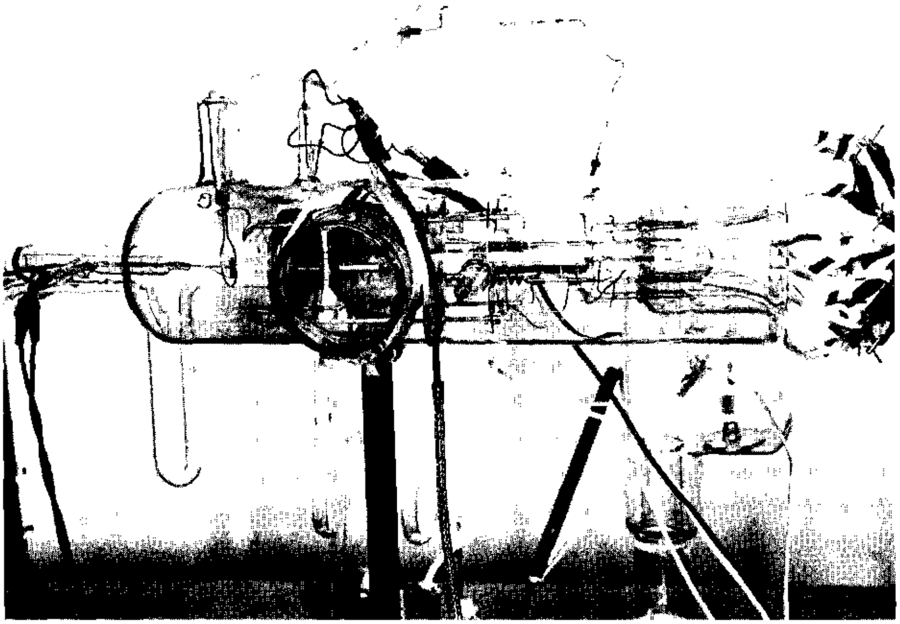

(a)

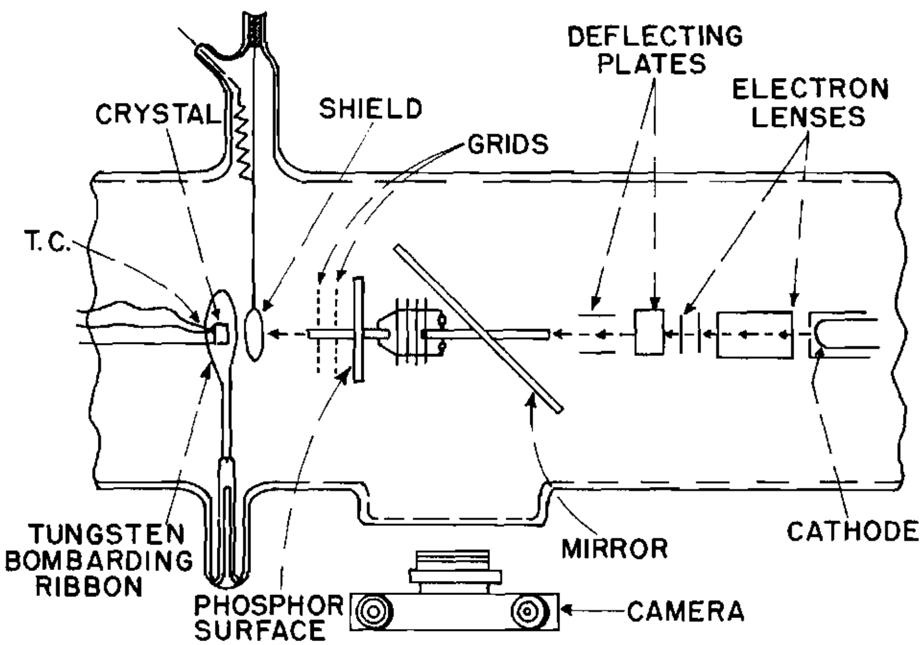

(b)

Figure 1. (a) Glass Encapsulated LEED Optics Used by Scheibner
(b) Schematic Diagram of LEED Optics.

grids and fluorescent screen were replaced by a spherical grid and screen assembly which subtended about one third of a hemisphere.[7] As these changes were being made, some elements of the electron optics were also improved, but the concept of the instrument has remained the same.

LEED has now been used in the experimental solutions of a large number of surface problems, and much data have been collected for metal, semiconductor and insulator crystal surfaces. It has been shown for many metals that the atomic arrangements for the clean surfaces are not appreciably different from what would be expected if the bulk crystal structures were discontinued at some particular plane. On the other hand, the surfaces of covalently bonded crystals such as silicon and germanium tend to be reconstructed, thereby minimizing the surface free energy. In many cases, even a fraction of a monolayer of gas adsorbed on an otherwise clean surface can be detected, and numerous substrate-adsorbate combinations have been investigated. Much of the data on some of the materials studied are summarized in a review by Lander[8] which also considers recent developments in the LEED technique and many of the current problems.

Inelastic Electron Scattering

Secondary electron emission measurements have also proved useful for studying solids and investigating the fundamental interactions of electrons with solids. In these studies, a sample is bombarded with electrons of a predetermined energy, and electrons emitted from the sample are examined with regard to number and energy and angular distributions. Although most previous experiments have been concerned only with measurements of secondary electron yield, the distributions in angle and energy of the secondary electrons have been determined for a number of materials. These distributions have been interpreted in terms of certain features of the band structure of the solid, the collective behavior of the "free" electron gas, and the properties of gases adsorbed on the surface or impurities in the bulk of the sample. However, the results reported by various laboratories have often been inconsistent regarding qualitative observations as well as quantitative interpretations, and a need for careful measurements on well defined surfaces has been indicated.

The history of secondary emission studies is somewhat older than that of elastic diffraction. In fact, the opacity of a metal to bombarding electrons was noted in the 1870's by Crookes, who was concerned with determining the properties of his "radiant matter" or cathode rays. Even so, the phenomenon of secondary electron emission as it is understood today was discovered much later by Austin and Starke[9] in 1902. Developments in this field of endeavor have been reviewed exhaustively,[10-15] and only those points of interest to the present work will be considered below.

In examining the secondary electron energy distributions, three fairly distinct groups of electrons are apparent, as is shown in Figure 2. This particular curve was obtained by analyzing the secondary electron current emitted from a clean tungsten (110) surface which was bombarded by 100-volt primary electrons. The electrons in region I are the elastically reflected primaries. These electrons have been scattered without losing energy to the sample, and it is often assumed that these are the electrons contributing to the observed diffraction patterns. The electrons in region II are rediffused primaries which have undergone losses (these losses usually being less than 60 ev). A number of small, broad peaks appear in this region. These peaks are referred to as characteristic losses, the difference in energy between these peaks and the primary energy being constant, independent of the primary energy. Two mechanisms which have been proposed to account for the observed energy losses are interband transitions and plasma resonances. The electrons in region III are the true secondaries. A number of subsidiary maxima appear on the high-energy side of the true secondary peak, and these maxima can be partly explained in terms of Auger type transitions. The small sharp spike on the low-energy side of this peak represents an instrumental effect to be described later.

Characteristic energy losses were first observed in 1924 by Becker,[16] who was using 200 ev incident electrons in his studies of electron reflection from solids. Similar semiquantitative observations were made by other groups, but Rudberg[17,18] was the first to clearly demon-

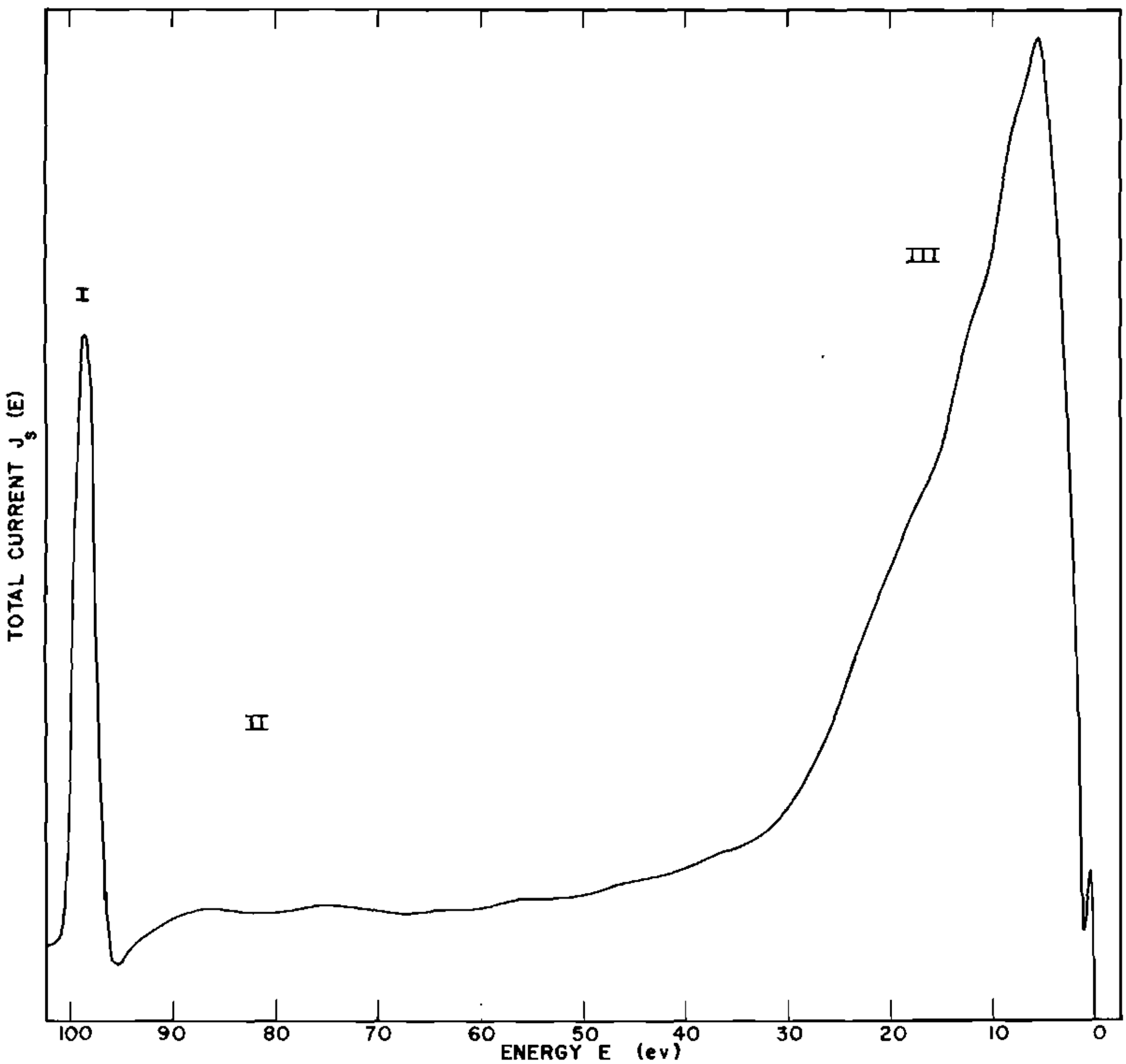

Figure 2. Secondary Electron Energy Distribution Curve for Clean Tungsten (110) Surface. 100 Volt Primary Electrons.

strate (in 1930) that, when slow electrons impinge upon solid surfaces, there are characteristic energy losses which appear as line spectra in the energy distribution curves obtained for the emitted electrons. Rudberg also showed the energy loss values to be independent, in a first approximation, of such parameters as incident electron energy, angle of incidence, and angle of observation.

In Rudberg's work, electrons in the range of 40 to 900 ev were used to bombard the samples; the reflected electrons of different energies were separated in a homogeneous magnetic field and detected in a Faraday collector. The targets used were prepared by evaporation in the vacuum of the instrument onto molybdenum or silver substrates. Ruthemann[19] described a similar instrument designed for incident electron energies of several kev. Ruthemann's experiments also differed from those of Rudberg in that characteristic energy losses were observed in electrons passing through thin films. In 1944, Marton[20] and Hillier and Baker[21] attempted measurements of energy losses in small, identified regions of the sample using experience and techniques related to electron microscopy; magnetic deflection was again used for energy analysis of the emitted electrons. In 1949, Möllenstedt[22] introduced a new method for energy analysis which was based on the very high chromatic aberration of electrostatic lenses. This latter method offered a much better energy resolution than had been achieved previously, and modified versions of this analyzer are still commonly used in experiments centered around high energy primary electrons.

Subsidiary maxima in the true secondary region of the energy distribution curves were first reported by Hayworth.[23] These maxima, which are discussed in a review by Hachenberg and Brauer,[24] represent electrons which are preferentially emitted at certain fixed energies, these energies being independent of the primary energy and characteristic of the sample. Other studies of this phenomena were made by Kollath,[25] who failed to observe the subsidiary maxima, and Lander[26] and Harrower,[27] who did observe the maxima for a number of different materials.

The techniques previously used for obtaining the distributions of the true secondary electrons are much the same as those employed in measurements of characteristic losses. Kollath[25] used a longitudinal magnetic field to separate the secondary electrons in energy, while Lander[26] and Harrower[27] used deflection analyzers of the magnetic and electrostatic types respectively. Retarding field methods have also been tried, but, because the retarding field curves must be differentiated to obtain the energy distributions, many attempts to use this method have proved unsuccessful. The required differentiation is very difficult to accomplish with sufficient accuracy by graphical or analog means, but a recently devised ac differentiation scheme[28,29] has made the retarding field method quite useful, particularly where measurements are restricted to low-energy electrons.

Investigations of phenomena related to secondary emission have been carried out for a variety of samples. The emphasis in these studies has been on identifying the mechanisms contributing to the observed structure in the energy distribution curves, and most such measurements have been concerned with the characteristic energy losses only. The application of secondary emission data to the problem of characterizing solid surfaces has received very little attention.

The Tungsten Sample

Tungsten has long been considered a standard for measurements of surface properties because of the relative ease with which samples of this material can be cleaned by flash heating in vacuum. Tungsten surfaces have been studied using many techniques, including flash-filament desorption,[30] field emission,[30] work function,[30] ion neutralization spectroscopy,[31] low-energy electron diffraction,[32] and secondary electron emission;[27] some of the pertinent results of these studies are summarized below. In addition, it should be pointed out that the experimental convenience offered by this material and the resulting wealth of related data available in the published literature were factors which led to the selection of a tungsten sample for this research.

Low-energy electron diffraction has been used to determine the structures of clean tungsten surfaces for a number of crystallographic orientations and to investigate some aspects of the adsorption of gases on these surfaces. Specific results are as follows:

1. Samples cut from zone refined ingots of tungsten contain carbon as a natural bulk impurity which diffuses toward the surface as a sample is heated. The effect of this surface carbon on the observed LEED patterns has been investigated by Stern[33] for the (110) surface. The carbon can be removed by heating the sample in a residual atmosphere of either oxygen or hydrogen.

2. Diffraction patterns obtained after cleaning the sample in the above manner indicate that the structure of the clean tungsten surface is the same as expected for a parallel layer of atoms in the bulk of the crystal.[32] However, the absence of neighboring atoms at the surface might be expected to result in unusually great amplitudes of thermal vibrations for the surface atoms; this is supported by field emission data[30] which show that atoms on the surface may become quite mobile at temperatures as low as one third the bulk melting temperature.

3. Gases are readily adsorbed on the (110) surface of tungsten with sticking probabilities near unity for coverages of less than a monolayer. Oxygen adsorption on this face has been studied by Germer, Stern and MacRae;[32] May, Germer and Chang[34] have reported on the adsorption of CO and the coadsorption of O_2 and CO. Similar studies have been made by Anderson and Estrup[35] for the adsorption of N_2 and CO on the (100) face.

Only a few inelastic electron scattering measurements have been reported for tungsten, but the results obtained are of interest to the present work. Harrower[27] observed subsidiary maxima on the true secondary peak and characteristic energy losses in his measurements on polycrystalline tungsten ribbons using primary electrons of 100 to 2000 electron volts. He interpreted the characteristic energy losses in terms of interband transitions and the subsidiary maxima as Auger electrons. Characteristic energy losses were also measured by Powell, Robins and Swan.[36] Primary electrons of 850 ev were used to bombard a polycrystalline tungsten wire; the observed losses were not interpreted.

A Combined Technique

Both low-energy electron diffraction and low-energy electron spectroscopy are useful techniques for characterizing solid surfaces and studying the interactions of slow electrons with these surfaces. In previous investigations, these experimental methods have been used independently, and the results obtained have often been difficult to interpret. However, many of the problems associated with the individual techniques are resolved by combining these methods into one instrument.

Among the difficulties encountered in LEED work is the fact that LEED patterns alone do not always provide enough information for unambiguous interpretations to be made concerning the surfaces being studied. For example, the LEED patterns corresponding to the clean tungsten (110) surface and the same surface with a full monolayer of adsorbed oxygen are essentially the same.[32] This means that the diffraction patterns can not be used to distinguish between these two surface states. Furthermore, the precise interpretation of these patterns requires a basic understanding of the diffraction phenomena and associated scattering processes for the low-energy electrons; this understanding has not been achieved so far in studies concerned only with the elastic scattering of the slow electrons.

As mentioned earlier, the results obtained in secondary emission studies have often been inconsistent both in terms of qualitative observations and quantitative interpretations. Most of the work to date has been carried out in modified electron microscopes using transmission through thin films or in deflection spectrometers using reflection from freshly evaporated surfaces. The principal difficulty in these studies seems to have been that of identifying sample surface conditions, as is illustrated by considering Harrower's work on tungsten.[27] The tungsten ribbons used in this study were cleaned in vacuum by heating for long periods at temperatures of about 2300°C. Heating the sample to these temperatures causes the desorption of gases and other volatile impurities, but, as shown using LEED, such heat treatment can result in an ordered accumulation of carbon on or near the surface of the sample. This carbon can have a pronounced effect on the secondary electron energy distribution curves as will be discussed in this paper. In the characteristic loss measurements of Powell, Robins and Swan,[36] the effects of surface conditions were considered, but the experimental surfaces were not sufficiently well characterized.

The combination of LEED and inelastic measurements as used in this study therefore offers a number of advantages. LEED can be used to examine the elastic scattering and to get information about the structure of the surfaces studied. The secondary electron energy distributions can be used to study the various inelastic processes and surface contamination, regardless of the structures assumed. This combined technique has proved quite useful for surface studies and for investigating some aspects of the elastic and inelastic scattering of the slow electrons. An important application of this method may be its use as a tool for characterizing experimental surfaces in conjunction with measurements of other phenomena such as work function, photoemission and optical reflectivity which are sensitive to surface conditions. The detailed specification of surface states potentially afforded by this tool can then be used to guarantee reproducible surface conditions for a series of measurements on different samples. Moreover, such a characterization would make possible a valid comparison of data obtained in different laboratories from similarly characterized surfaces.

CHAPTER II

THEORETICAL DISCUSSION

The scattering of slow electrons incident upon a single-crystal surface must be described in terms of coherent elastic diffraction and incoherent inelastic processes. Energy distributions of electrons back-scattered from a metal (typified by Fig. 2) are composed of electrons reflected without energy loss, electrons which have undergone discrete losses characteristic of the scattering material, and true secondaries emitted from the solid. The scattering mechanisms are in general coupled -- precise interpretations of LEED patterns can be made only by taking into account inelastic losses, and the inelastic intensity distributions are strongly influenced by the conditions for elastic diffraction. In this chapter, the scattering mechanisms and their interrelationships are discussed, first considering the various scattering processes individually; the last section consists of a summary of some of the main theoretical results and a description of the interconnections between the processes as appropriate for interpreting experimental data.

Elastic Diffraction

General Discussion for Slow Electrons

The elastic peak (region I) of the energy distribution curve of

Fig. 2 consists of coherently scattered electrons giving rise to reflections in the LEED patterns and incoherently but elastically scattered electrons appearing in the diffuse background of these patterns. The relative number of the incoherently scattered electrons is largely determined by the degree of crystalline order at the scattering surface and is influenced by such factors as sample temperature, dislocation density, surface contamination and strain. In the case of a perfect crystal, the elastic scattering would be coherent, whereas, for a completely disordered solid, the scattering would be entirely incoherent. For scattering from reasonably well ordered single-crystal surfaces, the diffuse background of the LEED patterns can be substantially reduced using the suppressor grid. This indicates that the elastic contribution to this background is small, and the elastic peak of Fig. 2 may be considered to represent mainly the coherent scattering of the low-energy electrons.

The diffraction of low-energy electrons is both qualitatively and quantitatively different from that of high-energy electrons or x-rays in that the atomic-scattering cross-sections are relatively very large. As pointed out by Lander,[8] the atomic-scattering cross-sections for electron energies $\lesssim 100$ ev are about the same magnitude as the area occupied by an atom in the lattice. A single atomic layer is thus a very efficient scatterer of slow electrons. Two important consequences of this fact are that the slow incident electrons penetrate only slightly into the crystal and multiple scattering is highly probable. Qualitatively, positions of reflections in the diffraction patterns can be calculated on the basis of a strictly two-dimensional lattice consisting of the first layer of atoms. However, any explanation of spot intensities requires that the effect of underlying layers be taken into account, and the high probability for multiple scattering implies a need for a self-consistent description of the diffraction process, thereby invalidating the more usual kinematical approaches for precise intensity analysis.[37]

It must be further emphasized that the penetration depth of the slow electrons is limited by an effective absorption; the intensity of the incident beam decreases as the beam penetrates into the crystal because electrons scattered out of the beam by surface layers can no longer be considered as part of the electron flux incident on underlying layers. The absorption is termed effective in that there is no mechanism the low-energy electrons equivalent to photoelectric absorption.[38] Rather, the electrons are removed from the primary beam by elastic and inelastic scattering processes. If is, therefore, not surprising that the penetration depth depends strongly on the diffraction conditions.

LEED Patterns

The positions of reflections in the LEED patterns can be predicted using simply the Laue conditions in direct analogy with the x-ray case. For a three-dimensional diffraction situation involving a triperiodic crystal, these conditions (which must be satisfied simultaneously) are written

$$(\bar{q} - \bar{q}_o) \cdot \bar{a}_1 = 2\pi h; \quad (\bar{q} - \bar{q}_o) \cdot \bar{a}_2 = 2\pi k; \quad (\bar{q} - \bar{q}_o) \cdot \bar{a}_3 = 2\pi \ell . \qquad (1)$$

Here $\bar{q}_o$ and $\bar{q}$ are respectively the incident and diffracted wavevectors with magnitude $2\pi/\lambda$; the vectors $\bar{a}_1$, $\bar{a}_2$, $\bar{a}_3$ are lattice translation vectors with $\bar{a}_3$ assumed normal to the crystal surface; h, k, ℓ are integers. The electron wavelength λ (in Angstroms) is given by the expression[8]

$$\lambda = \left(\frac{150}{V} \right)^{\frac{1}{2}} , \qquad (2)$$

where V is the incident beam voltage in volts. The conditions in (1) can be interpreted geometrically, and, requiring that $\bar{q}$ and $\bar{q}_o$ have the same magnitude, one arrives at the usual Ewald construction[8,39] illustrated in Fig. 3(a) for electrons backscattered from the crystal. The three-dimensional diffraction conditions are satisfied when any one of the reciprocal lattice points (small open circles) intersects the Ewald sphere of reflection; one then observes a beam of electrons with the primary energy emerging from the crystal as described by the diffracted vector $\bar{q}$.

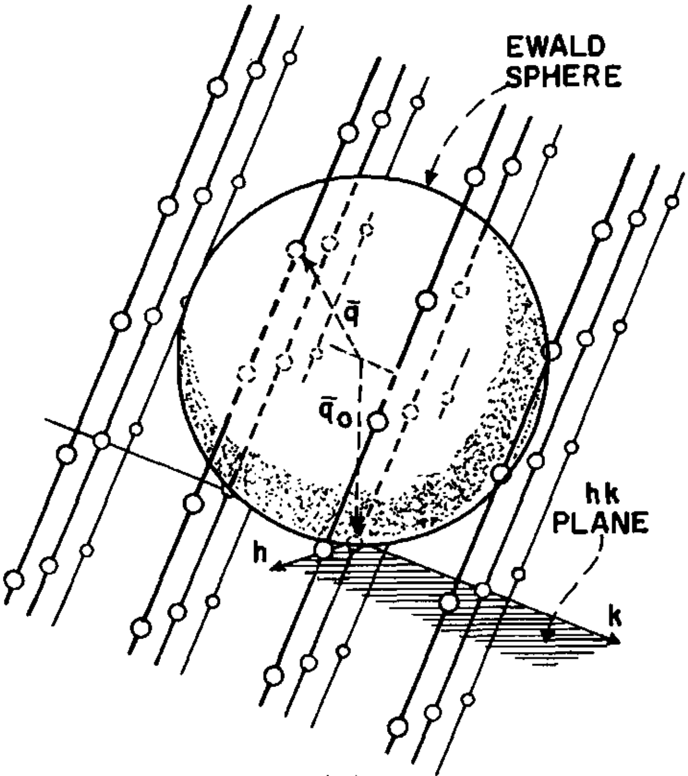

(a)

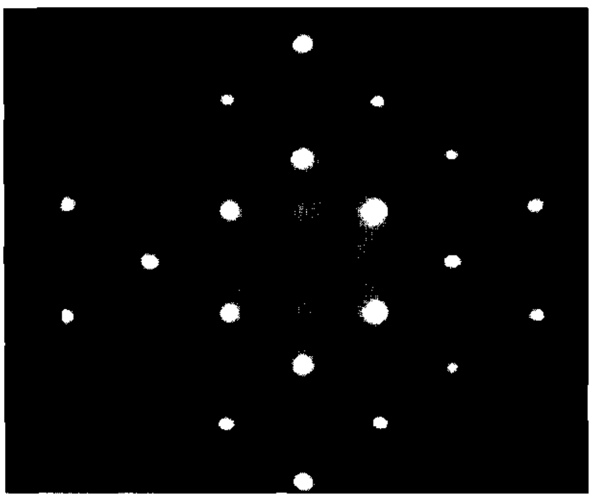

(b)

Figure 3. (a) Ewald Construction for Back-Reflected Low-Energy Electrons. (b) Typical LEED Pattern Obtained from Tungsten (110) Surface. 300 Volt Primary Electrons.

For low-energy electrons the penetration depth is so small that crystal periodicity in the direction perpendicular to the surface is only weakly sampled. This circumstance leads to a relaxation of the third Laue condition, and, in the limit of purely two-dimensional diffraction, the reciprocal lattice points become uniform rods oriented normal to the surface as indicated in the figure. However, considering that several layers may contribute to the observed scattered intensities, the reciprocal lattice should properly be described as consisting of rods strongly modulated in density along their length with maxima near the 3-D reciprocal lattice points. Interpretations based on this simple picture are complicated by the fact that the degree of modulation of the reciprocal lattice rods varies with penetration depth, which, in turn, may depend sharply and often irregularly on factors such as incident beam voltage and crystal orientation.[37]

The application of the geometrical construction is thus limited to locating the various reflections in diffraction patterns. This is done by assuming two-dimensional diffraction involving only the first layer of atoms, constructing the 2-D reciprocal lattice for this surface layer, identifying the points at which the reciprocal lattice rods intersect the sphere of reflection, and determining the angles between the allowed diffraction vectors $\bar{q}$ and the incident vector $\bar{q}_o$. The allowed diffracted vectors can then be projected onto a spherical surface and compared with observed diffraction patterns such as given in Fig. 3(b) for a clean tungsten (110) surface bombarded with 300 ev electrons.

For surfaces with adsorbed gas layers or other contaminants, the LEED patterns may be considerably more complicated than shown in Fig. 3(b). Foreign atoms on a crystal surface can assume 2-D structures characterized by translation vectors much larger than for the substrate crystal, and, because of the reciprocal relationship between structures and diffraction patterns, many extra reflections are observed. These problems of extra features and registry between surface and substrate structures are discussed by Lander[8] and can not be profitably reviewed here.

A final note must be made concerning surface crystallography. For three-dimensional diffraction, reciprocal lattice points are indexed using the Miller indices h, k, ℓ corresponding to the plane spacing $d_{hk\ell}$. In the case of LEED, the patterns exhibit a strong plane grating character in that the allowed reflections are visible at nearly all wavelengths. This means that the third Laue condition can be essentially disregarded, and patterns can be indexed using the 2-D indices h, k. The notation is then quite analogous with conventions relied upon in 3-D crystallography except that fractional order indices describing the expanded surface nets are frequently encountered.[8] An excellent reference on this subject is provided by Wood.[40]

Intensity Analysis

Diffraction intensities in LEED have not as yet received a satisfactory theoretical description. Problems encountered in the theoretical work include a lack of detailed understanding of the crystal inner potential, high probability for multiple scattering, strong absorption due to both elastic and inelastic processes, polarization and exchange effects, and unknown atomic-scattering factors. The atomic-scattering factors can not be calculated precisely because of severe limitations in the applicability of the first Born approximation for the energy range of interest. In spite of these difficulties, there has been some apparent success in explaining observed intensities in a few instances, and several approaches to this problem are mentioned briefly below.

Proceeding again by analogy with x-ray diffraction methods of analysis, one seeks to formulate structure factors in terms of which one may explain experimental intensity data and get information about the periodic distribution of scattering density near the surface of a crystal. In most of the recent work, attempts have been made to use structure factors calculated on the basis of the kinematical theory of diffraction. Using the kinematical approach it is assumed that an electron is scattered only once, there is no interaction between the incident and scattered beams, and that intensity and wavelength are conserved. These assumptions lead to the form factor which, for normally incident electrons, can be written[8]

$$F_{hk}(\lambda, \theta) = \sum_j f_j(\lambda, \theta) \exp 2\pi i \left[hx_j + ky_j + (1 + \cos\theta_{hk}) z_j / \lambda \right], \qquad (3)$$

where f_j is the atomic-scattering factor for the jth atom and the summation is over all atoms. Note that this expression for the form factor has been specialized for slow electrons in that periodicity in the direction normal to the surface is not explicitly required. However, the expression does not take into account the obvious strong absorption, the possibility of multiple scattering or the other effects of polarization, exchange and crystal inner potential.

A modified kinematical approach which introduces corrections to Eq. (3) based on higher order terms in the Born expansion is described by Palmberg and Peria.[41] The strong absorption is considered by assuming that the summation [as in Eq. (3)] includes only atoms in the first few layers; inner potential corrections are made crudely by adding to the incident beam energy the average value of the inner potential. These modifications do not significantly improve the accuracy of the results in most cases, mainly because dynamical effects are not considered.

One can include a more explicit description of the absorption by introducing into Eq. (3) a transmission amplitude factor per atom layer[8] $\tau(\alpha, t)$. α is a complicated function representing inelastic losses, and t is a factor taking into account elastic losses by reflection. In some instances it has been found that the intensity data can be explained by summing the scattering amplitude over atoms clearly visible from above the surface in a conventional crystal structure model.[8] This simple correction to the structure factor then becomes

$$F_{hk}(\lambda, \theta) = \sum_{j} t_j(\tau)\, f_j(\lambda, \theta) \exp 2\pi i \left[hx_i + ky_i + (1 + \cos\theta_{hk})\, z_j / \lambda \right] , \quad (4)$$

where $t_j(\tau)$ is the transmission amplitude factor per atom, which may be taken as unity or zero (or more reasonable values assigned), depending on visibility from above the surface. It must be emphasized that these descriptions represent a drastic oversimplication in that they treat the penetration depth or total absorption as being independent of incident beam energy; this is not a realistic assumption for slow electrons.

Hirabayaski and Takeishi[42] have developed a dynamical theory of slow electron diffraction which is an extension of von Laue's theory of the diffraction of electrons by a single atom layer.[43] In this approach, the Schrödinger equation is reduced to a set of coupled ordinary differential equations using the two-dimensional Fourier transform of the scattering potential. Wave functions are obtained which can then be used to compute scattered intensities. The effect of inelastic scattering is accounted for by introducing a complex potential energy, as often done in optics. The main limitation of the theory is that interferences between reflections were considered in detail only in a two-beam approximation.

A multiple-scattering treatment of LEED intensities has been carried out by McRae.[37] The treatment is based on Lax's multiple-scattering equations[44] and provides a self-consistent description which effects a separation between the problem of the diffraction of electrons by a crystal and the atomic-scattering problem. This separation is important in that atomic-scattering phase shifts obtained separately can be used as input for a computation, and effects such as spin and charge correlation in atomic scattering can be incorporated conveniently in the calculations.

Although a complete and fully satisfactory calculation of LEED intensities has not yet been published, it is perhaps noteworthy that outstanding contributions in this field have been made during the past two years (as indicated by the publication dates of the principal references cited). Interest in precise intensity interpretations is growing both on the part of theorists and experimentalists, so that a rapid increase in understanding is to be expected within the next few years.

Characteristic Energy Losses

Backscattering of Slow Electrons

The discussion is now turned to a consideration of those processes whereby electrons in the incident beam lose discrete amounts of energy in single-electron or collective excitations. These characteristic losses are represented by the small broad peaks in region II of Fig. 2; the differences in energy between these peaks and the primary energy are constant, independent of the primary energy, and characteristic of the scattering substance.

As in the case of elastic diffraction, inelastic cross-sections for low-energy electrons are relatively large. Inelastic losses per layer in the energy range of about 100 ev are reported by Lander to be of the order of 50 per cent.[8] These data are confirmed by results for scattering by gaseous atoms and molecules,[45] which show maximum cross-sections in the energy range between 50 and 100 ev. The total inelastic cross-section for scattering by a gas is largely comprised of cross-sections for single ionization; for solids, plasmon and phonon losses must also be considered. Because of the large inelastic cross-sections, these inelastic processes will tend to limit the penetration depth of a beam of electrons incident upon a crystal, and multiple losses arising from multiple excitations are to be expected.

Two mechanisms proposed to account for losses observed in the present study are interband transitions and plasma oscillations. These processes differ in that an interband transition involves the pair-wise interaction between an electron in the incident beam and one of the crystal electrons, whereas plasma resonances are collective excitations of the electron cloud involving charge density fluctuations in some particular small volume of the sample. On the other hand, energy loss values for the two processes are of the same magnitude, and it is often difficult to distinguish between them in experimental data.

Observing characteristic losses in a back-reflection experiment is complicated by the fact that the maximum angle of deflection for an electron losing energy by exciting an interband transition or plasmon is generally quite small. This can be seen by simply requiring conservation of momentum for the interaction as pictured schematically in Fig. 4.

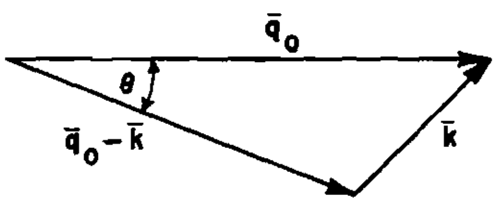

Figure 4. Schematic Drawing of Inelastic Scattering Event with Linear Momentum Conserved.

$\bar{q}_o$ is the wavevector of the incident electron, $\bar{k}$ is the wavevector of the excitation, and $\bar{q}_o - \bar{k}$ describes the electron after the scattering event. The angle of deflection θ is given by

$$\tan\theta = \frac{k_\perp}{q_o - k_\parallel} \quad , \tag{5}$$

where $k_\perp$ and $k_\parallel$ are the components of $\bar{k}$ normal and parallel to $\bar{q}_o$ respectively. An upper limit k_{max} can be imposed on the value of k either from conservation of energy or, in the case of plasmon excitation, by noting that the concept of collective oscillations loses meaning for plasmon wavelengths as small as the average interelectron spacing.[46] Taking the worst case with $k_\parallel = 0$ and $k_\perp = k_{max}$, the maximum angle of deflection θ_{max} becomes

$$\theta_{max} = \tan^{-1} \frac{k_{max}}{q_o} . \tag{6}$$

A typical value of θ_{max} is obtained for 100 ev electrons ($q_o = 5.4 \times 10^8\ cm^{-1}$) by setting $k_{max} = k_c$, where k_c is the critical wavevector derived from the interelectron spacing ($k_c = 1.85 \times 10^8 cm^{-1}$ for tungsten). These numbers give $\theta_{max} = 18.7°$, and from Eq. (6) it is clear that much smaller values are obtained for higher energy incident electrons. The essential result is that the angle of deflection is not sufficient to reverse the direction of slow electrons incident upon a thick sample. This means that, if the electrons are to undergo such losses and also be backscattered from the sample so as to be collected and measured, two scattering events are required. An electron in the incident beam can experience an inelastic collision (most likely an incoherent process) and subsequently be elastically diffracted by the lattice. Alternatively, the electrons which are first coherently backscattered by the crystal (and which would appear in the diffraction maxima of the LEED pattern) can lose energy in the inelastic process and not be scattered appreciably out of the diffracted beams. Experimentally the sequence of the scattering events is quite significant. If the electrons lose energy after elastic diffraction by the crystal, one should find these electrons in a diffuse cluster around the expected diffraction maxima, while the electrons which are diffracted after the inelastic scattering would give rise to new reflections in the LEED patterns (apparently of very low intensity).

Single-Electron Excitations

Single-electron excitations in a metal represent processes in which electrons in the metal are raised from states at or below the Fermi surface to unoccupied states in the same or in higher order Brillouin zones; these excitations are accompanied by corresponding losses of energy and momentum on the part of primary electrons incident upon the solid. These transitions, which result from the two-body Coulomb interaction between the primary and metal electrons, may be divided into several different cases depending on the energy bands involved and the momentum selection rules which must be satisfied:

1. Intraband Transitions -- Electrons in a particular band (usually only the conduction band) are excited to unoccupied states

in the same band. The transitions are essentially free-electron interactions described by a momentum conservation law involving only the initial and the final momenta of the two interacting electrons.

2. Interband Transitions -- Electrons are excited from states at or below the Fermi surface (including the lower-lying atomic levels) to vacant states in any of the Brillouin zones. Momentum is conserved directly in the two-body interaction and there is no momentum transferred to the lattice.

3. Umklapp Processes -- These are interband type transitions which involve mainly those electrons originating in the upper-lying bands near the Fermi surface. Momentum is not conserved directly in the two-body interaction; rather, there is an exchange of momentum with the lattice as a whole. The momentum conservation law includes the reciprocal lattice vector, and transitions are possible in which the wavevector of a metal electron is changed by a large amount even though the wavevector change of the corresponding primary electron is extremely small.

The essential features of the interband type transitions to be dealt with here are the values of the energy losses sustained by the primary electrons and the dependence of the excitation probabilities on primary energy. Following the guides of experimental data, the discussion is aimed mainly at umklapp processes involving conduction band electrons. Early studies of these processes were made by

Fröhlich,[47] Rudberg and Slater,[48] and Wooldridge.[49] These earlier calculations have been corrected and extended in more recent work reported by Dekker and van der Ziel,[50, 51] Baroody[52] and Viatskin[53]; it is on these later calculations that the discussion below is based.

The excitations to be considered involve the transfer of a few electron volts from one of the primary electrons to one of the metal electrons, and will be regarded as arising from the unscreened Coulomb interaction between the two electrons. It is convenient to assume at the outset that the energy of the primary electron is large enough to consider it as free, so that its energy is $\hbar^2 K^2/2m$ and its wave function $\exp[i\bar{K}\cdot\bar{R}]$. The wave function of the lattice electron with wave-vector $\bar{k}$ is represented by $\psi_{\bar{k}}(\bar{r})$ and is assumed to be normalized per unit volume.

If there were no interaction between the two electrons, the wave function of the system would be

$$\Psi = e^{i\bar{K}\cdot\bar{R}}\,\psi_{\bar{k}}(\bar{r})\,e^{\frac{-iEt}{\hbar}} , \tag{7}$$

where the total energy E is given by

$$E = E(\bar{k}) + \frac{\hbar^2 K^2}{2m} . \tag{8}$$

However, because of the interaction $V = e^2/|\bar{R} - \bar{r}|$, transitions are possible such that the lattice electron goes from state $\bar{k}$ to $\bar{k}'$ and the primary from $\bar{K}$ to $\bar{K}'$. The wave function representing the two electrons at time t can then be written

$$\Psi(t) = \sum_{\bar{k}''} \sum_{\bar{K}''} A_{\bar{k}''\bar{K}''}(t)\, e^{i\bar{K}''\cdot\bar{R}}\, \psi_{\bar{k}''}(\bar{r})\, e^{\frac{-iE''t}{\hbar}} , \tag{9}$$

where

$$E'' = E_{(\bar{k}'')} + \frac{\hbar^2 K''^2}{2m} . \tag{10}$$

Treating the interaction V as a perturbation, the Schrödinger equation for the two-particle system is written

$$\{ H_o + \lambda V \} \Psi(t) = i\hbar \frac{\partial}{\partial t} \Psi(t) . \tag{11}$$

Substituting the expansion for $\Psi(t)$, one obtains (see following page)

$$\sum_{\bar{k}''}\sum_{\bar{K}''} A_{\bar{k}''\bar{K}''}(t)\, e^{i\bar{K}''\cdot\bar{R}}\, \psi_{\bar{k}''}(\bar{r})\, e^{\frac{-iE''t}{\hbar}} \tag{12}$$

$$= \frac{\lambda}{i\hbar}\sum_{\bar{k}''}\sum_{\bar{K}''} A_{\bar{k}''\bar{K}''}(t)\, \frac{e^2}{|\bar{R}-\bar{r}|}\, e^{i\bar{K}''\cdot\bar{R}}\, \psi_{\bar{k}''}(\bar{r})\, e^{\frac{-iE''t}{\hbar}}$$

Multiplying both sides by $e^{-i\bar{K}'\cdot\bar{R}}\,\psi_{\bar{k}'}(\bar{r})$ and integrating over the volume of the crystal, Eq. (12) can be written

$$\dot{A}_{\bar{k}'\bar{K}'} = \frac{\lambda}{i\hbar}\sum_{\bar{k}''}\sum_{\bar{K}''} A_{\bar{k}''\bar{K}''}\int_{\bar{r}}\int_{\bar{R}} \frac{e^2}{|\bar{R}-\bar{r}|}\, e^{i(\bar{K}''-\bar{K}')\cdot\bar{R}}\, \psi_{\bar{k}''}\psi^{*}_{\bar{k}}\, e^{\frac{-i(E''-E')t}{\hbar}}\, d\bar{r}d\bar{R}. \tag{13}$$

As usual, one expands the $A_{\bar{k}'\bar{K}'}$'s

$$A_{\bar{k}'\bar{K}'} = \sum_{s} \lambda^{s} A^{(s)}_{\bar{k}'\bar{K}'}\ , \tag{14}$$

and substituting into Eq. (13) one gets

$$\sum_{s}\lambda^{s} \dot{A}^{(s)}_{\bar{k}'\bar{K}'} = \frac{1}{i\hbar}\sum_{\bar{k}''}\sum_{\bar{K}''}\sum_{s}\lambda^{s+1} A^{(s)}_{\bar{k}''\bar{K}''}\int_{\bar{r}}\int_{\bar{R}} \frac{e^2}{|\bar{R}-\bar{r}|}\, e^{i(\bar{K}''-\bar{K}')\cdot\bar{R}} \quad \times \tag{15}$$

$$\psi_{\bar{k}''} \psi_{\bar{k}'}^{*} e^{\frac{-i(E''-E')t}{\hbar}} d\bar{r}\, d\bar{R} .$$

Taking terms not involving λ one finds

$$\dot{A}^{(o)}_{\bar{k}', \bar{K}'} = 0 , \tag{16}$$

and one assumes that initially the system is in a state defined by wave-vectors $\bar{k}$ and $\bar{K}$ so that

$$A_{\bar{k}', \bar{K}'} = \delta_{\bar{k}, \bar{k}'} \delta_{\bar{K}, \bar{K}'} . \tag{17}$$

Now the first order terms can be calculated with the result

$$\dot{A}^{(1)}_{\bar{k}', \bar{K}'} = \frac{1}{i\hbar} \int_{\bar{r}} \int_{\bar{R}} \frac{e^2}{|\bar{R} - \bar{r}|} e^{i(\bar{K} - \bar{K}') \cdot \bar{R}} \psi_{\bar{k}} \psi_{\bar{k}'}^{*} e^{\frac{-i(E - E')t}{\hbar}} d\bar{R}\, d\bar{r}. \tag{18}$$

Assuming that the interaction commences at $t = 0$, one can write

$$A^{(1)}_{\bar{k}', \bar{K}'}(t) = \frac{1}{i\hbar} \int_{o}^{t} \int_{\bar{r}} \int_{\bar{R}} e^{i(\bar{K} - \bar{K}') \bar{R}} \frac{e^2}{|\bar{R} - \bar{r}|} \psi_{\bar{k}} \psi_{\bar{k}'}^{*} e^{\frac{-i(E - E')t}{\hbar}} d\bar{R}\, d\bar{r}\, dt . \tag{19}$$

Using the identity[50, 54]

$$\int_{\bar{R}} \frac{e^2}{|\bar{R}-\bar{r}|} e^{i(\bar{K}-\bar{K}')\cdot\bar{R}} d\bar{R} = \frac{4\pi e^2}{q^2} e^{i\bar{q}\cdot\bar{r}}, \tag{20}$$

where $q = \bar{K} - \bar{K}'$, Eq. (19) can be reduced to

$$A_{\bar{k}',\bar{K}'}(t) = \frac{1}{i\hbar} \int_0^t \int_{\bar{r}} \frac{4\pi e^2}{q^2} e^{i\bar{q}\cdot\bar{r}} \psi_{\bar{k}} \psi^*_{\bar{k}'} e^{\frac{-i(E-E')t}{\hbar}} d\bar{r}\, dt. \tag{21}$$

Carrying out the integration over time one obtains finally

$$A_{\bar{k}',\bar{K}'}(t) = \frac{4\pi e^2}{q^2} \frac{e^{\frac{i(E-E')t}{\hbar}} - 1}{E-E'} I, \tag{22}$$

where

$$I = \int_{\bar{r}} e^{i\bar{q}\cdot\bar{r}} \psi_{\bar{k}}(\bar{r}) \psi^*_{\bar{k}'}(\bar{r}) d\bar{r}. \tag{23}$$

The transition probability for the transition $\bar{k}, \bar{K} \rightarrow \bar{k}', \bar{K}'$ is defined by $|A_{\bar{k}',\bar{K}'}|^2$ and may be expressed

$$\left| A_{\bar{k}',\bar{K}'}(t) \right|^2 = \frac{32\pi^2 e^4}{q^4} \; \frac{\left\{ 1 - \cos\frac{(E' - E)t}{\hbar} \right\}}{(E' - E)^2} \; \left| I \right|^2 \quad . \tag{24}$$

Note that for large values of t, the transition probability has a strong maximum for $E' - E = 0$ or when energy is conserved in the two-body interaction.

Restricting the discussion now to the case of weakly bound lattice electrons, one observes that the wave functions describing these electrons are solutions of the Schrödinger equation with a periodic potential. This means that the wave functions must satisfy the relation

$$\psi_{\bar{k}}(\bar{r} + \bar{G}) = \psi_{\bar{k}}(\bar{r}) e^{i\bar{k} \cdot \bar{G}} \quad , \tag{25}$$

where $\bar{G}$ is a lattice vector. Next, it is convenient to rewrite Eq. (23) as

$$I = \sum_{\bar{G}} \int_{\Delta r} e^{i\bar{q} \cdot (\bar{r} + \bar{G})} \; \psi_{\bar{k}}(\bar{r} + \bar{G}) \, \psi^{*}_{\bar{k}'}(\bar{r} + \bar{G}) \, d\bar{r} \tag{26}$$

where the integration is over the unit cell at the origin and the summation includes all lattice vectors. Using Eq. (25), one can write Eq. (26) as

$$I = I_o \sum_{\bar{G}} e^{i(\bar{k} - \bar{k}' + \bar{q}) \cdot \bar{G}} \quad . \tag{27}$$

In this last expression, I_o is the value of the integral of Eq. (23) taken over the unit cell at the origin. The sum has a non-zero value only when the terms from all of the lattice points are in phase. This gives the momentum selection rule

$$\bar{k}' = \bar{k} + \bar{q} + 2\pi \bar{H} \tag{28}$$

with $\bar{H}$ a reciprocal lattice vector.* When this selection rule is satisfied, the sum in Eq. (27) is just N, the number of unit cells in the crystal.

The energy transferred from the primary to the lattice electron can be determined by solving the energy conservation relation implied by Eq. (24) simultaneously with the momentum selection rule above. This energy loss is given by

* The summation leading to the momentum selection rule [Eq. (28)] is over unit cells in the crystal and not over scattering centers. This means that certain values of $\bar{H}$ may be forbidden because of cancellation due to out-of-phase contributions from scattering centers within the individual unit cells. This cancellation is in direct analogy with the situation for x-ray diffraction.[55] For the case of a body-centered cubic crystal, only values of $\bar{H}$ described by Miller indices whose sums are even integers are permitted.

$$\Delta E = \frac{\hbar^2}{2m}(K^2 - K'^2) = E(\bar{k}') - E(\bar{k}) . \tag{29}$$

Assuming for the purpose of this approximate calculation that the lattice electron is essentially free, the energy loss ΔE can be written

$$\Delta E = \frac{\hbar^2}{2m}(k'^2 - k^2) = \frac{\hbar^2}{2m}(4\pi^2 H^2 + q^2 + 4\pi\bar{q}\cdot\bar{H} + 4\pi\bar{k}\cdot\bar{H} + 2\bar{q}\cdot\bar{k}), \tag{30}$$

the last term being obtained by direct substitution of Eq. (28). Averaging this expression for ΔE over the initial states $\bar{k}$ and assuming a free-electron density of states, one obtains

$$\Delta E = \frac{\hbar^2}{2m}(4\pi^2 H^2 + q^2 + 4\pi\bar{q}\cdot\bar{H}) . \tag{31}$$

It may be noted at this point that the transitions corresponding to $\bar{H} = 0$ are ordinary momentum-conserved interband and intraband type transitions and that only for non-zero values of $\bar{H}$ are the umklapp processes involved. For the case $\bar{H} = 0$ the energy loss reduces to

$$\Delta E_o = \frac{\hbar^2}{2m} q^2 , \tag{32}$$

and, to the extent that $\bar{q}/2\pi$ may be neglected in comparison with the smallest non-vanishing reciprocal lattice vector, Eq. (32) for $\bar{H} \neq 0$ becomes

$$\Delta E_H \approx \frac{2\pi^2 \hbar^2}{m} H^2 . \tag{33}$$

Returning to the calculation of transition probabilities, one notices that Eq. (24) expresses the probability for a transition from $\bar{K}$ to $\bar{K}'$ and $\bar{k}$ to $\bar{k}'$ as a function of time, whereas one desires to have the probability per unit time for the incident electron to make a transition from $\bar{K}$ to a new state with wavevector magnitude between K' and $K' + dK'$ and direction in $d\Omega'$, while a metal electron simultaneously jumps from $\bar{k}$ to $\bar{k}'$. This new transition rate is derived from $|A_{\bar{k}'\bar{K}'}(t)|^2$ in the usual way:[50, 56] (1) Eq. (24) is multiplied by the number of states with wavevector in $d\Omega'$ and magnitude in the range K' to $K' + dK'$, i.e., by $mK'dE'd\Omega'/(2\pi)^3\hbar^2$; (2) the resulting expression is integrated with respect to dE'; and (3) the probability is differentiated with respect to time to give the probability per unit time. Carrying out these operations one easily obtains the transition rate

$$\frac{4me^4 K'}{\hbar^3 q^4} |I|^2 d\Omega , \tag{34}$$

which can be further changed to yield the probability per unit distance along its path that the incident electron will make a transition from $\bar{K}$ to $\bar{K}'$ lying in $d\Omega'$, with a metal electron going from $\bar{k}$ to $\bar{k}'$, by just dividing Eq. (34) by the velocity of the primary electron, $\hbar K/m$. This gives

$$P(\bar{k}, \bar{K} \rightarrow \bar{k}', \bar{K}')\, d\Omega' = \frac{4m^2 e^4 K'}{\hbar^4 q^4 K} |I|^2 \, d\Omega' . \qquad (35)$$

Finally, integrating this expression over solid angle, it is possible to show the dependence of the excitation rate on primary energy by a rough calculation which is valid only for small values of $\bar{q}$. Before carrying out the indicated integration, it is convenient to make note of several approximate relationships.

Letting θ be the angle between $\bar{K}'$ and $\bar{K}$, one has that

$$q^2 - q^2_{min} = q^2 - (K - K')^2 = 2KK'(1 - \cos\theta) \approx K^2\theta^2 , \qquad (36)$$

where q_{min} represents the smallest value of $\bar{q}$ for fixed values of $\bar{K}$ and $\bar{K}'$; the approximate equality on the right side of this expression holds for the many collisions for which the angle of deflection θ is small, as discussed at the beginning of this section. From energy conservation one has

$$E(\bar{k}') = E(\bar{k}) + \frac{\hbar^2}{2m}(K^2 - K'^2) \, . \tag{37}$$

Again, for small $\bar{q}$, the momentum law can be rewritten

$$\bar{k}' = \bar{k} + 2\pi\bar{H} \, , \tag{38}$$

so that Eq. (37) gives

$$q_{min} = K - K' = \frac{2m\epsilon}{\hbar^2(K+K')} \approx \frac{m\epsilon}{\hbar^2 K} \; ; \tag{39}$$

here ϵ is given by

$$\epsilon = E(\bar{k} + 2\pi\bar{H}) - E(\bar{k}) \, , \tag{40}$$

and the small difference between K and K$'$ is neglected in the final term of Eq. (39). Using Eq. (36), the element of solid angle $d\Omega'$ can be approximated

$$d\Omega' = \frac{q\,dq\,d\phi}{K^2} \, , \tag{41}$$

ϕ being the azimuthal angle. Referring back to Eqs. (23) and (27) one finds that, for small $\bar{q}$, the term exp $i(\bar{q} \cdot \bar{r})$ can be expanded in a

McLaurin's series, and, retaining only the first two terms, one has

$$e^{i\bar{q}\cdot\bar{r}} = 1 + i\bar{q}\cdot\bar{r} \ . \tag{42}$$

The integral over the unit cell, I_o, can now be written

$$I_o = \int_{\Delta r} [1 + i\bar{q}\cdot\bar{r}]\,\psi_{\bar{k}}\,\psi^{*}_{\bar{k}+2\pi\bar{H}}\,d\bar{r} \tag{43}$$

$$= i\bar{q}\cdot\int_{\Delta r} \bar{r}\,\psi_{\bar{k}}\,\psi^{*}_{\bar{k}+2\pi\bar{H}}\,d\bar{r}$$

and $|I|^2$ becomes

$$|I|^2 = q^2 N^2 \left| \int \bar{r}\,\psi_{\bar{k}}\,\psi^{*}_{\bar{k}+2\pi\bar{H}}\,d\bar{r} \right|^2 . \tag{44}$$

Substituting Eqs. (41) and (44) into Eq. (35), the excitation rate can be written

$$\int P\,d\Omega' = \iint \frac{4m^2 e^4 K' N^2}{\hbar^4 qK^3} \left| \int \bar{r}\,\psi_{\bar{k}}\,\psi^{*}_{\bar{k}+2\pi\bar{H}}\,dr \right|^2 dq\,d\Phi \tag{45}$$

$$\propto \frac{1}{E_p} \int_{q_{min}}^{q_{max}} \frac{dq}{q}$$

$$\propto E_p^{-1} \ln (q_{max} / q_{min}) \; ,$$

where E_p is the primary energy. Allowing values of $\bar{q}$ up to

$$q_{max} \approx \pi H \approx (q_{min} K)^{\frac{1}{2}} \; , \tag{46}$$

and neglecting small contributions from larger values of $\bar{q}$[52], one finds

$$\int P d\Omega' \propto 1/2 \, E_p^{-1} \ln (2E_p / \epsilon) \; . \tag{47}$$

This expression shows a relatively slow increase in the total transition rate with decreasing energy and is in agreement with the result obtained by Baroody[52] in a more detailed calculation. One may then conclude that umklapp processes are as important for slow incident electrons as for high-energy primaries. On the other hand, it must be noted that Eq. (47) does not express the possibility of a threshold energy below which the primary electron is not able to excite the transition, as would be expected from physical arguments. Further, the range of validity of the calculation must be restricted to primary energies of about 500 ev and above for $\epsilon \sim 10$ ev because of the assumption of $q_{min} << \pi H$. Even so, one might expect that the angular and energy distributions which may be derived from Eq. (35) would be qualitatively correct for electrons with energies above the threshold value.

Bulk Plasma Resonances

Plasma resonances in a metal are collective oscillations of the electron cloud which arise because of the long range nature of the Coulomb interaction between a primary electron and lattice electrons. These collective excitations were first explained by Bohm and Pines[57] in 1952 and have since been the subject of numerous theoretical investigations.[15, 46, 58-62] Several approaches have proved useful in examining this collective behavior of the electron gas, including the collective description of Bohm and Pines and the dielectric model[62] to be considered below. In the latter case, it is assumed that the ensemble of conduction electrons in a metal may be characterized by a dielectric constant which is a function both of the frequency and wavevector of the electromagnetic disturbance. The dielectric approach offers the advantage that one is able to describe both collective and individual electron interactions within the same framework. However, it must be noted that the success of this theory hinges on the fact that the range of the interaction is large compared with interelectronic spacings.

Of specific interest here are the form of the excitation probability per unit path length and the energy loss values of low-energy primary electrons. Following Ritchie's derivation,[62] the metal is treated as an infinite, continuous, homogeneous neutral plasma with complex dielectric constant $\epsilon_{\bar{k},\omega}$. It is convenient to describe an incident electron as a point charge moving along a well defined path with velocity $\bar{v}$. This moving charge gives rise to a charge density[63]

$$\rho(\bar{r}, t) = -e\delta(\bar{r} - \bar{v}t) . \tag{48}$$

The field generated in the plasma is given by Poisson's equation,

$$\epsilon\nabla^2 \phi(\bar{r}, t) = -4\pi\rho(\bar{r}, t). \tag{49}$$

In Fourier space Poisson's equation may be written for independent variables $\bar{k}$ and ω

$$\phi_{\bar{k},\omega} = \frac{4\pi\rho_{\bar{k},\omega}}{k^2\epsilon_{\bar{k},\omega}} . \tag{50}$$

The potential ϕ is regarded as a perturbation acting on the electrons of the metal. This perturbation causes transitions from occupied to unoccupied levels; electrons making such transitions acquire energy $\hbar\omega$

and momentum $\hbar\bar{k}$ with corresponding losses by the primary electrons.

The probability for the absorption of energy $\hbar\omega$ and momentum $\hbar\bar{k}$ per unit path length for the primary electron is given by

$$P_{\bar{k},\omega} = \frac{1}{\hbar\omega} W_{\bar{k},\omega} \tag{51}$$

with $W_{\bar{k},\omega}$ the energy absorbed by the medium per unit volume in $\bar{k}$ space, per unit frequency interval and per unit path length. The total energy absorbed per unit path length is given by

$$\frac{dw}{dx} = \iint W_{\bar{k},\omega} d\bar{k}\, d\omega \quad , \tag{52}$$

and the energy loss per unit path length in the medium is written

$$\frac{-dw}{dx} = eE_x \Big|_{\bar{r} = \bar{v}t} = \frac{e}{v} \bar{v} \cdot \bar{E} \Big|_{\bar{r} = \bar{v}t} . \tag{53}$$

Here $\bar{E}$ is the electric field due to the medium alone,

$$\bar{E} = \mathrm{Re}(- \nabla \Phi) \Big|_{\bar{r} = \bar{v}t} . \tag{54}$$

The potential ϕ can now be derived from the charge distribution of Eq. (48). By definition,

$$\rho(\bar{r}, t) = \frac{1}{(2\pi)^4} \int \int \rho_{\bar{k}, \omega} e^{i(\bar{k} \cdot \bar{r} + \omega t)} d\bar{k}\, d\omega = -e\delta(\bar{r} - \bar{v}t) . \quad (55)$$

Using the identity[64]

$$\delta(\bar{x} - \bar{x}') = \frac{1}{(2\pi)^3} \int e^{i\bar{k} \cdot (\bar{x} - \bar{x}')} d\bar{k}, \quad (56)$$

one may write

$$\delta(\bar{r} - \bar{v}t) = \frac{1}{(2\pi)^3} \int e^{i\bar{k} \cdot (\bar{r} - \bar{v}t)} d\bar{k} \quad (57)$$

$$= \frac{1}{(2\pi)^3} \int \int e^{i(\bar{k} \cdot \bar{r} + \omega t)} \delta(\bar{k} \cdot \bar{v} + \omega)\, d\bar{k}\, d\omega .$$

Comparing the form of Eq. (57) with the expression for the charge distribution $\rho(\bar{r}, t)$ given in Eq. (55) one observes that $\rho_{\bar{k}, \omega}$ is given by

$$\rho_{\bar{k}, \omega} = -2\pi e\, \delta(\bar{k} \cdot \bar{v} + \omega) . \quad (58)$$

Poisson's equation then becomes

$$\Phi_{\bar{k},\omega} = \frac{-8\pi^2 e}{\epsilon_{\bar{k},\omega}} \frac{\delta(\bar{k}\cdot\bar{v}+\omega)}{k^2} , \tag{59}$$

Finally, the potential $\Phi(\bar{r}, t)$ is written

$$\Phi(\bar{r}, t) = \frac{1}{(2\pi)^4} \int\int \Phi_{\bar{k},\omega} e^{i(\bar{k}\cdot\bar{r}+\omega t)} d\bar{k}\, d\omega \tag{60}$$

$$= -\frac{1}{(2\pi)^4} \int\int e^{i(\bar{k}\cdot\bar{r}+\omega t)} \frac{8\pi^2 e}{\epsilon_{\bar{k},\omega}} \frac{\delta(\bar{k}\cdot\bar{v}+\omega)}{k^2} d\bar{k}\, d\omega .$$

Taking the gradient of the last expression one obtains

$$-\nabla\Phi = \frac{i}{(2\pi)^4} \int\int \bar{k}\, e^{i(\bar{k}\cdot\bar{r}+\omega t)} \frac{8\pi^2 e}{\epsilon_{\bar{k},\omega}} \frac{\delta(\bar{k}\cdot\bar{v}+\omega)}{k^2} d\bar{k}\, d\omega . \tag{61}$$

This gives for the energy loss per unit path length of Eq. (53)

$$\frac{-dw}{dx} = \mathrm{Re}\left\{ \frac{e}{v}\ \bar{v} \cdot (-\nabla\Phi) \Big|_{\bar{r}=\bar{v}t} \right\} \tag{62}$$

$$= \mathrm{Re}\left\{ \frac{ie^2}{2\pi^2 v} \int\int \bar{k}\cdot\bar{v}\, e^{i(\bar{k}\cdot\bar{r}+\omega t)} \frac{1}{\epsilon_{\bar{k},\omega}} \frac{\delta(\bar{k}\cdot\bar{v}+\omega)}{k^2}\, d\bar{k}\, d\omega \right\} \Big|_{\bar{r}=\bar{v}t}$$

The condition $\bar{r} = \bar{v}t$ may be included explicitly by carrying out the integration over ω ,

$$\frac{-dw}{dx} = \mathrm{Re}\left\{ \frac{ie^2}{2\pi^2 v} \int \bar{k}\cdot\bar{v}\, e^{i\bar{k}\cdot(\bar{r}-\bar{v}t)} \frac{1}{\epsilon_{\bar{k},-\bar{k}\cdot\bar{v}}} \frac{1}{k^2}\, d\bar{k} \right\} \Big|_{\bar{r}=\bar{v}t} \tag{63}$$

$$= \mathrm{Re}\left\{ \frac{ie^2}{2\pi^2 v} \int \bar{k}\cdot\bar{v} \frac{1}{\epsilon_{\bar{k},-\bar{k}\cdot\bar{v}}} \frac{1}{k^2}\, d\bar{k} \right\} .$$

Expanding this equation again into the integral form one has

$$\frac{-dw}{dx} = \mathrm{Re}\left\{ \frac{-ie^2}{\pi^2 v} \int\int_0^\infty \frac{\omega}{\epsilon_{\bar{k},\omega}} \frac{\delta(\bar{k}\cdot\bar{v}+\omega)}{k^2}\, d\omega\, d\bar{k} \right\} , \tag{64}$$

or

$$\frac{-dw}{dx} = \frac{-e^2}{\pi^2 v} \int \int_0^\infty \omega \, \mathrm{Re} \left(\frac{i}{\epsilon_{\bar{k},\omega}} \right) \frac{\delta(\bar{k} \cdot \bar{v} + \omega)}{k^2} \, d\omega \, d\bar{k} \; . \tag{65}$$

The probability per unit path length $P_{\bar{k},\omega}$ is related to the energy loss $\frac{dw}{dx}$ by the definitions of Eqs. (51) and (52) and may be written

$$P_{\bar{k},\omega} = \frac{e^2}{\pi^2 \hbar v} \, \mathrm{Im} \left(\frac{1}{\epsilon_{\bar{k},\omega}} \right) \frac{\delta(\bar{k} \cdot \bar{v} + \omega)}{k^2} \tag{66}$$

As may be seen from this expression, the detailed dependence of the excitation probability is determined by the form assumed for the complex dielectric constant.

A form for the complex dielectric constant $\epsilon_{\bar{k},\omega}$ is derived in detail in Appendix A for the case of nearly free electrons. Taking the result of this calculation, one has from Eq. (A-36)

$$\epsilon_{\bar{k},\omega} = 1 + \frac{2m^2 \omega_p^2}{\hbar^2 k^2} \sum_n F(E_n) \left\{ \frac{1}{k^2 + 2\bar{k} \cdot \bar{k}_n + \frac{2m}{\hbar} (\omega - i\gamma)} \right. \tag{67}$$

$$\left. + \frac{1}{k^2 - 2\bar{k} \cdot \bar{k}_n - \frac{2m}{\hbar} (\omega - i\gamma)} \right\} ,$$

where ω_p is the classical plasma frequency given in Eq. (A-37). Combining the denominators of Eq. (67), $\epsilon_{\bar{k},\omega}$ may be written

$$\epsilon_{\bar{k},\omega} = 1 - \omega_p^2 \sum_n F(E_n) \left\{ (\omega - i\gamma + \frac{\hbar}{m} \bar{k} \cdot \bar{k}_n)^2 - \frac{\hbar^2 k^4}{4m^2} \right\}^{-1} . \tag{68}$$

Expanding the denominator of this expression and assuming ω to be large compared with other terms, one obtains

$$\left\{ (\omega - i\gamma + \frac{\hbar}{m} \bar{k} \cdot \bar{k}_n)^2 - \frac{\hbar^2 k^4}{4m^2} \right\}^{-1} \approx \frac{1 + \frac{\hbar^2 k^4}{4m^2\omega^2} - \frac{2\hbar}{\omega m} \bar{k} \cdot \bar{k}_n + \frac{3\hbar^2}{\omega^2 m^2} (\bar{k} \cdot \bar{k}_n)^2}{(\omega - i\gamma)^2} . \tag{69}$$

Substituting this expansion into Eq. (68) and replacing the sum over states by an integral, one writes for a free electron density of states,

$$\epsilon_{\bar{k},\omega} = 1 - \frac{\omega_p^2}{(\omega - i\gamma)^2 (2\pi)^2 N} \int_0^{k_o} \int_0^{\pi} \left\{ 1 + \frac{\hbar^2 k^4}{4m^2\omega^2} - \frac{2\hbar}{m\omega} k k_n \cos\theta_n \right. \tag{70}$$

$$\left. + \frac{3\hbar^2}{m^2\omega^2} k^2 k_n^2 \cos^2\theta_n \right\} k_n^2 \sin\theta_n \, d\theta_n \, dk_n .$$

In this equation N is the free electron density, and k_o is the Fermi momentum which is related to N by

$$N = \frac{2k_o^3}{3(2\pi)^2} \quad . \tag{71}$$

Carrying out the indicated integrations, one finds

$$\epsilon_{\bar{k},\omega} = 1 - \frac{\omega_p^2}{(\omega - i\gamma)^2} \left\{ 1 + \frac{\hbar^2 k^4}{4m^2\omega^2} + \frac{3\hbar^2 k^2 k_o^2}{5m^2\omega^2} \right\} \tag{72}$$

$$= \frac{(\omega - i\gamma)^2 - \omega_p^2 (1+\delta)}{(\omega - i\gamma)^2} \quad ,$$

where δ is defined to be

$$\delta = \frac{\hbar^2}{m^2\omega^2} \left(\frac{k^4}{4} + \frac{3}{5} k^2 k_o^2 \right) . \tag{73}$$

For substitution into the equation for the probability per unit path length, one needs $\mathrm{Im}\left(\frac{1}{\epsilon}\right)$, which is obtained directly from Eq. (72).

$$\mathrm{Im}\left(\frac{1}{\epsilon_{\bar{k},\omega}}\right) = \mathrm{Im}\left\{\frac{(\omega - i\gamma)^2}{(\omega - i\gamma)^2 - \omega_p^2(1+\delta)}\right\} \tag{74}$$

$$= \mathrm{Im}\left\{\frac{(\omega^2 - 2i\gamma\omega)\,(\omega^2 - \omega_p^2(1+\delta) + 2i\gamma\omega)}{[\,\omega^2 - \omega_p^2(1+\delta)\,]^2 + 4\gamma^2\omega^2}\right\}$$

$$= \frac{2\gamma\omega_p^2\,\omega(1+\delta)}{[\,\omega^2 - \omega_p^2(1+\delta)\,]^2 + 4\gamma^2\omega^2}$$

Combining this result with Eq. (66) one has finally for $P_{\bar{k},\omega}$

$$P_{\bar{k},\omega} = \frac{e^2}{\pi^2\hbar v}\;\frac{\delta(\bar{k}\cdot\bar{v}+\omega)}{k^3}\;\frac{2\gamma\omega_p^2\,\omega(1+\delta)}{[\,\omega^2 - \omega_p^2(1+\delta)\,]^2 + 4\gamma^2\omega^2}\;. \tag{75}$$

The result derived in Eq. (75) is the probability per unit path length for collective excitations of the nearly free electron gas. As can be seen from this equation, $P_{\bar{k},\omega}$ shows a strong resonance when

$$\omega^2 = \omega_p^2(1+\delta)\;, \tag{76}$$

for small values of the damping constant γ. This resonance condition is satisfied within the above approximations if ω and ω_p are related by

$$\omega^2 = \omega_p^2 + \frac{\hbar^2}{m^2}\left(\frac{k^4}{4} + \frac{3k^2 k_o^2}{5}\right), \tag{77}$$

which is the same plasma dispersion relation derived by Bohm and Pines[57] using the collective approach. The energy loss sustained by a primary electron exciting a bulk plasmon is then given by $\hbar\omega$ and exhibits the dependence on the value of the wavevector of the excitation as predicted by Eq. (77).

Returning to Eq. (75), the dependence of the excitation probability on the energy of the primary electron can now be examined. Dividing the wavevector of the excitation, $\bar{k}$, into $k_{\parallel}$ and $k_{\perp}$, components parallel and perpendicular to the incident electron velocity $\bar{v}$, one may integrate $P_{\bar{k},\omega}$ over $k_{\parallel}$ to get

$$P_{k_\perp,\omega} = \frac{e^2}{\pi^2 \hbar v}\; \frac{2v\omega_p^2\,\omega(1+\delta)}{[\omega^2 - \omega_p^2(1+\delta)]^2 + 4\gamma^2\omega^2} \int \frac{\delta(k_{\parallel}v + \omega)}{k_\perp^2 + k_{\parallel}^2}\, dk_{\parallel} \tag{78}$$

$$= \frac{e^2}{\pi^2 \hbar v^2}\; \frac{2\gamma\omega_p^2\,\omega(1+\delta)}{[\omega^2 - \omega_p^2(1+\delta)]^2 + 4\gamma^2\omega^2}\; \frac{1}{\left(k_\perp^2 + \frac{\omega^2}{v^2}\right)}\,.$$

The dependence of $P_{k_\perp, \omega}$ on primary energy may now be written

$$P_{k_\perp, \omega} \propto \frac{1}{v^2 k_\perp^2 + \omega^2} = \frac{m}{2E_p k_\perp^2 + m\omega^2} \quad . \tag{79}$$

As the term $m\omega^2$ is generally many orders of magnitude larger than the multiplicative factor $2k_\perp^2$, one finds that the transition rate is nearly constant or increases very slowly with decreasing primary energy.* This again suggests that this excitation is of importance for slow electrons, but, as in the case of the single-electron excitations, no threshold for excitation is predicted, and the applicability of the results would be restricted to primary energies well above the experimental threshold value.

The free-electron model of the complex dielectric constant can not generally be applied to metals for which the plasmon frequency is affected by the presence of single-electron excitations. Such discrete transitions were not considered in either the derivation of the dielectric constant or in Eq. (70), which was obtained assuming a free-electron density of states. When such transitions are important, one must use a form for $\epsilon_{\bar{k}, \omega}$ given by Nozières and Pines[59]

---

* For an excitation energy $\hbar\omega = 20$ ev, $m\omega^2 = 3.3 \times 10^{29}$ gm/s^2, whereas using $k_\perp = k_c = 1.85 \times 10^8$ cm^{-1} as for Eq. (6), one obtains $2k_\perp^2 = 6.8 \times 10^{16}$ gm/s^2.

$$\epsilon_{\bar{k},\omega} = 1 - \frac{4\pi e^2}{m} \sum_n \frac{f_{on}(\bar{k})}{\omega^2 - \omega_{on}^2} . \tag{80}$$

In this expression the $f_{on}(\bar{k})$ are transition probabilities or oscillator strengths for transitions characterized by excitation energy $\hbar\omega_{on}$. The effect of this coupling of single-particle and collective excitations can then be considered by substituting Eq. (80), in place of Eq. (72), into the expression for the transition probability, and the plasmon dispersion relation can be obtained simply by noting the resonance condition implied by Eq. (66), namely

$$\epsilon_{\bar{k},\omega} \approx 0 \tag{81}$$

for ω equal to the collective excitation frequency. Combining equations (80) and (81) one gets

$$1 = \frac{4\pi e^2}{m} \sum_n \frac{f_{on}(\bar{k})}{\omega^2 - \omega_{on}^2} , \tag{82}$$

and this expression can be used to predict the energy loss value for the primary electron in the collective excitation for known interband type transitions. In practice, however, the oscillator strengths for the single-electron transitions are not known, and the use of Eq. (82) is limited to showing that the general effect of higher lying interband transitions is to depress the plasmon frequency toward lower values, whereas transitions with excitation energies less than the plasmon energy tend to raise the plasmon frequency toward higher values. For a more detailed analysis it is necessary to obtain the frequency dependence of the complex dielectric constant separately from optical reflectivity data or other means, as emphasized by Raether.[65] This coupling of interband transitions and collective oscillations is particularly significant in the first transition series metals for which there is no satisfactory theoretical formulation, and the use of optical data in interpreting the characteristic losses in this case has been discussed in detail by Jordan and Scheibner.[66]

The advantage of the dielectric theory of energy losses as discussed above is that the relationship between single-particle and collective excitations is clearly displayed in the form chosen for the complex dielectric constant. Further, the resonance condition predicted indicates how one should properly consider the complex dielectric constant obtained from optical data in order to clarify the interpretation of characteristic energy losses. The theory is applicable to the case of low-energy primary electrons, except for the threshold restriction already mentioned and to the extent that the incident particle may be described as following a well defined trajectory with fixed velocity v.

Such an assumption is realistic only for electrons with energies great enough not to be changed appreciably by losses in the medium, i.e., electrons with energies of several hundred ev or greater undergoing losses of 10 to 20 ev. However, it is not clear what effect the applicability of this approximation has on the results for the case of single scattering events, and results might be expected to be qualitatively correct for much slower electrons. Multiple excitations, on the other hand, require further consideration.

Surface Plasma Resonances

The calculations on bulk resonances assumed an infinite solid; effects of bounding surfaces were not considered. A similar analysis may be carried through for a finite solid, and, as shown by Ritchie,[62] the effect of the surfaces is to produce resonances similar to the bulk collective excitations, but occurring at a lower characteristic frequency. These oscillations of reduced energy result from a decrease in the electric field in the medium very near the surface due to depolarizing effects associated with the surface.

Ritchie's calculations were concerned with fast electrons incident upon a thin foil. The foil was treated as a continuous, neutral plasma infinite in two dimensions, and bounded by parallel planes oriented normal to the incident beam with separation distance a. Again, the dielectric theory was used to determine the excitation probability for the surface resonance. Approximations inherent in the calculation restrict the validity of results to high-energy primary electrons, and, for this reason, the derivation of this excitation probability is not discussed in detail. However, since it appears that the results may be at least qualitatively correct for slow electrons and since a more applicable treatment has not been described, it is appropriate to summarize some of the key features of Ritchie's calculation.

The approach taken is quite similar to that used in describing the excitation of bulk resonances. The incident electron is described as a point charge moving along a well defined path with velocity $\bar{v}$, and one calculates the potential throughout all space due to this charge, including the modifying effect of the foil. The energy loss in the medium is defined by Eq. (53), and may be expressed in terms of the potential Φ and as an integral over $\bar{k}$ and ω, in analogy with Eq. (60). Finally, using the definitions for the excitation probability, Eqs. (51) and (52), one is able to obtain the excitation probability per unit path length, per unit volume in $\bar{k}$ space, and per unit frequency interval, which, for the surface resonance, corresponds to Eq. (66).

The essential difference in this description and the one for the bulk resonance lies in the calculation of the potential in terms of the charge distribution representing the incident particle. It is convenient to use the linearized Bloch hydrodynamical equations to describe the behavior of the perturbed conduction electrons.[67, 68] Assuming irrotational motion, these equations for points inside the foil may be written

$$\gamma\psi + \frac{\partial\psi}{\partial t} = -\frac{e}{m}\Phi + \frac{P\rho}{m\rho_o} \tag{83}$$

$$\frac{\partial\rho}{\partial t} = \rho_o \nabla^2 \psi \tag{84}$$

$$\nabla^2 \Phi = 4\pi e \rho + 4\pi e\, \delta(x - vt)\, \delta(y)\, \delta(z) \quad , \tag{85}$$

Here, Φ, ψ and ρ are regarded as perturbations around the undisturbed state; γ is a damping constant; $-\nabla\psi$ is the velocity of the perturbed electrons; P/ρ_o is the pressure change per unit number density in the undisturbed plasma; the x direction is parallel to $\bar{v}$ and normal to the foil; and P is given by the expression

$$P = \left(\frac{3h^3}{8\pi}\right)^{2/3} \frac{\rho_o^{2/3}}{3m} \; . \tag{86}$$

The equations (83), (84) and (85) are respectively the force, continuity and Poisson's equations. Outside the foil one uses only Poisson's equation

$$\nabla^2 \Phi = 4\pi e\, \delta(x - vt)\, \delta(y)\, \delta(z) \; . \tag{87}$$

Following the guide of the previous calculation, one would next transform these equations into their respective expressions in Fourier space. However, because of the planar boundaries, this transform can be carried through only in two dimensions, and the Bloch equations are reduced to a set of linear, ordinary differential equations in the variable x. Boundary conditions which must be satisfied are that the electric potential and electric field intensity must be continuous and the normal component of the electron velocity must vanish at the foil surfaces. The solutions to these equations are obtained in a straightforward manner, except that the boundary conditions are rather cumbersome. Ritchie's result for the excitation probability may be expressed in the limit of a thick foil as

$$P_{k_\perp, \omega} = \frac{e^2 a}{\hbar \pi^2 v^2} \left\{ \frac{\mathrm{Im}(1/\epsilon)}{(k^2_\perp + \omega^2/v^2)} \right. \tag{88}$$

$$\left. - \frac{2k_\perp}{a(k^2_\perp + \omega^2/v^2)^2} \, \mathrm{Im}\left(\frac{(1-\epsilon)^2}{\epsilon(1+\epsilon)} \right) \right\} .$$

In this expression, a is the foil thickness, ϵ is the complex dielectric constant, and $k_\perp$ is the component of $\bar{k}$ normal to $\bar{v}$. It is of interest to compare the form of Eq. (88) with the expressions obtained for the bulk excitation probability, Eqs. (66) and (78); it is apparent that the first term in Eq. (88) is the excitation probability per unit path length for an infinite solid multiplied by the equivalent path length in the medium, a. The second term then represents the boundary correction.

As in the case of the bulk resonance, one may now examine the detailed dependences of the excitation probability and obtain the plasmon dispersion relations by substituting the proper form for the complex dielectric constant. In this regard, it must be noted that a considerable difficulty is encountered in attempting a quantum mechanical derivation of the dielectric constant for a finite solid. If one assumes that the electrons move in a field to which they all give rise, as in Appendix A, then one finds for a finite foil that the Fourier components of the field are not proportional to the same Fourier components of the sources [see for comparison Eq. (A-21)]. Hence, the dielectric constant as it is usually defined does not exist in this case. However, it may be shown that the quantum corrections to the classical expression are not large for free electrons (particularly when high-energy primaries are considered), and one may write[62, 69]

$$\varepsilon = 1 - \frac{\omega_p^2}{\omega^2 - i\gamma\omega} . \tag{89}$$

This result is also obtained very easily from Eq. (72) by neglecting the quantum contributions which give rise to the $\bar{k}$ dependent dispersion.

Returning now to the expression for the excitation probability, one notices that there are two conditions under which resonances would be expected to occur. The first resonance condition, affecting the first term of Eq. (88), is $\epsilon = 0$, which corresponds to the excitation of the bulk plasmon already considered; the second condition, corresponding to the surface excitation, is $\epsilon = -1$. Imposing the latter on the expression for ϵ and neglecting the small term due to damping, one obtains immediately the expression for the free-electron surface plasmon frequency,

$$\omega = \frac{\omega_p}{\sqrt{2}} , \tag{90}$$

where ω_p is, of course, the classical oscillation frequency for the electron gas.

For those metals which can not be described by the free-electron model, one may choose to use a dielectric constant of the form given in Eq. (82). However, problems associated with unknown oscillator strengths for the interband transitions still remain. A precise analysis would therefore require that the frequency dependence of the complex dielectric constant be obtained by means, such as optical data.[66]

It has been implicitly assumed throughout this discussion that the planar surfaces of the metal are bounded by vacuum. If, on the other hand, one assumes that the foil is bounded by a dielectric, such as a thin oxide layer, a significant change in the surface plasmon excitation results, as shown by Stern and Ferrell.[70] They predicted that the effect of an oxide layer would be to cause a smearing out and consequent decrease in intensity for the characteristic loss peak corresponding to the excitation of the surface resonance described by Eq. (90). Further, they showed that a new loss should appear due to the excitation of a surface resonance at a frequency

$$\omega' = \frac{\omega_p}{\sqrt{1+\epsilon'}} \quad , \tag{91}$$

where ϵ' is the dielectric constant of the surface oxide layer; oxide thicknesses on the order of 20 Å should be sufficient to give rise to the new loss at a lower frequency, but the decrease in intensity of the clean surface loss could conceivably occur for even lower coverages. Moreover, this quenching of the clean surface resonance has important application in the interpretation of experimental energy loss data, to be discussed later.

True Secondary Emission

Multiple Inelastic Collisions

The true secondary electrons appear in the large low-energy peak (region III) of the secondary electron energy distribution of Fig. 2.

This peak generally accounts for at least 80 percent of the total electron current emitted from the solid for primary electrons with 100 ev energy and above. Included in this region of the distribution are electrons with energies up to about 50 ev, although there is no clear separation between the true secondary electrons and rediffused primaries normally associated with the characteristic loss region of the curve. However, a distinction can be made between peaks representing electrons in these two regions in that true secondary electrons have constant energy with varying primary energy, whereas the energy of electrons undergoing characteristic energy losses varies with the primary energy such that the difference between the primary and "loss" energy values remains constant.

The distribution of the true secondary electrons is relevant to the interpretation of experimental data. However, the shape of the broad multiple-scattering peak and other features of the distribution are topics of another investigation[71,72] currently in progress which will form the basis for a subsequent thesis.[73] Consequently, it is not necessary to give an exhaustive description of these processes here; rather some of the general features of the secondary distribution are discussed in order to identify the mechanisms involved and to permit the later interpretation of experimental results.

Reviews of the secondary distributions have been given by McKay,[10] Dekker[14] and Hachenberg and Brauer.[24] The general shape of the true secondary peak is the same for all metals; it is characterized by a maximum in the range of 3 to 5 ev. This broad peak is considered to result from electrons undergoing multiple inelastic collisions in the solid, and the shape of this peak thus indirectly represents the probability that an electron involved in such collisions will escape from the solid. Previous calculations have dealt mainly with the multiple-scattering nature of the secondary emission processes; the details of the actual interaction mechanisms (especially the collective excitations) have not been considered.

Discrete Processes

Superimposed on the high-energy side of the true secondary peak are a number of subsidiary maxima, also shown in Fig. 2. These maxima represent electrons preferentially emitted from the solid as a result of discrete processes such as Auger emission or umklapp processes. Subsidiary maxima have been considered in earlier studies by Hayworth,[23] Lander,[26] Harrower[27] and others[74]; the peaks were explained by Lander[26] on the basis of Auger transitions in the bulk.

In an Auger process, an electron is excited from a low-lying energy level (A) by a collision with one of the primary electrons. The empty level may then be filled by the absorption of an electron from an upper level (B), and the energy released appears in the form of an Auger electron ejected from a nearby upper level (C). The energy of the emitted electron is thus a function of the energy values for the participating levels and may be written

$$E = (E_A - E_B) - E_C \quad , \tag{92}$$

where $(E_A - E_B)$ is the de-excitation energy and E_C is the energy (measured relative to the vacuum level) of the level from which the Auger electron is ejected.

One must also consider the possibility of Auger transitions involving the atomic energy levels of foreign species adsorbed on the surface or present as bulk impurities. These transitions would be similar to the Auger neutralization processes described by Hagstrum.[31] In the Auger neutralization process one of the adsorbed gas atoms is ionized by the impact of one of the primary electrons. The ion, thus formed, is then neutralized directly to its ground state by one of the bulk metal electrons, and an Auger electron is ejected from one of the metal levels in analogy with the bulk Auger process. The energy of the emitted electron is again determined from Eq. (92) except that $(E_A - E_B)$ must now be taken to represent the de-excitation energy in the adsorbed ion.

In addition to the two-electron Auger processes, there are possible transitions related to the single-electron excitations which give rise to preferentially emitted electrons in the secondary distribution. Specifically, in the umklapp processes discussed earlier, a primary electron loses an amount of energy to one of the metal electrons, the latter usually originating in one of the upper lying bands. The energy exchanged in the interaction is given approximately by Eq. (33), and one finds that this energy is often sufficient for the metal electron to escape and be observed in the experimental secondary distributions. The energy of this emitted electron would then be the energy lost by the primary electron minus the energy required to raise the metal electron from its initial state to the vacuum level. It may be further noted from the momentum change predicted for the metal electron [Eq. (38)], that the angular distribution of umklapp electrons should be very highly anisotropic, whereas the angular distributions for electrons involved in the multiple inelastic collisions are generally regarded as being rather smooth.

Summary

In this chapter several aspects of the electron scattering problem have been reviewed with emphasis on the interpretation of electron scattering experiments. Such interpretations are complicated by the relatively large number of interacting phenomena which contribute to features observed in the scattered distributions. Further, the interconnections existing between the various elastic and inelastic processes are frequently not recognized, even though these interrelationships may have a pronounced effect on the observed distributions. It is, therefore, appropriate to summarize here some of the main theoretical points and to outline the interconnections as required to understand experimental data. It should be noted, however, that not all topics mentioned in this section are considered or applied in the sections which follow.

The penetration depth of slow electrons incident upon a solid surface is very slight due to large cross-sections for both elastic and inelastic scattering. As a result, the scattered distributions are quite sensitive to surface conditions, and slow electron scattering provides a unique tool for investigating surface properties. On the other hand, the strong absorption leads to a high probability for multiple scattering and the penetration depth may depend sharply and irregularly on incident beam energy and direction because of diffraction contributions to the absorption.

The elastic diffraction of low-energy electrons has not as yet received a satisfactory theoretical description. Problems encountered in the theoretical work are numerous; briefly stated, approximations relied upon in descriptions of high-energy electron scattering are not applicable in the slow electron case, and the presence of strong dynamical effects, such as absorption, introduces serious errors in any discussion of intensities based on the kinematic theory. Diffraction intensities have thus not been fully exploited in surface studies. However, atomic structures of clean single-crystal surfaces and surfaces with ordered adsorbed gas layers can often be determined by interpreting the corresponding LEED patterns on the basis of two-dimensional diffraction in the kinematic approximation as discussed in connection with Fig. 3.

The connection between the inelastic scattering mechanisms and diffraction intensities for slow electrons has been recognized as important,[8] but even the more exact treatments[37] consider these inelastic effects only in an average manner as an effective absorption or ignore them entirely.

Electrons incident on a solid may lose discrete amounts of energy by exciting single-electron transitions or collective resonances. The energy loss value is generally less than 50 ev and is characteristic of the sample and independent of the incident beam energy and direction. Requiring conservation of linear momentum, one finds that the maximum angle of deflection for the primary electron undergoing such a characteristic loss is not sufficient to reverse its direction; this means that, before this electron can be reflected and thus escape from the thick sample into the detector, at least two scattering events are required. The primary electrons may lose energy in the inelastic process and subsequently be elastically diffracted, or, alternatively, the electrons may be first elastically diffracted by the crystal and then lose energy in the excitation, escaping from the sample without further scattering. In either case, the angular distributions of the electrons recorded in the loss peak corresponding to the inelastic process would be determined to first order by the conditions for elastic diffraction; for example, electrons first diffracted and then losing energy in the inelastic event would form a diffuse ring about the expected diffraction maxima, and the positions of these diffuse clusters in the pattern would be determined by the diffraction conditions and not by details of the inelastic processes.

Several different types of single-electron excitations may occur: intraband transitions, interband transitions and umklapp processes. The first two excitations are momentum conserved, and the energy exchanged in the interaction is given by Eq. (32). Umklapp processes involve an exchange of momentum with the lattice as a whole, and the momentum conservation law contains the reciprocal lattice vector; the energy loss, in this case, is given approximately by Eq. (33). The form of the excitation probability for the single-electron transitions indicates that these processes are important for slow as well as fast primary electrons; no excitation threshold is predicted, but experimental observations indicate that such a threshold should be included.

Primary electrons exciting bulk collective resonances lose an amount of energy $\hbar\omega$, where ω may be determined from Eq. (77) if the electrons participating in the resonance are nearly free. The effect of bounding surfaces in a finite solid is to introduce a surface resonance occurring at a lower characteristic frequency, which for the free electron case is given by Eq. (90). Excitation probabilities indicate that these processes are important for slow primary electrons, but calculations need to be extended to describe very slow primary electrons and to include a threshold for excitation.

Interband type transitions and plasmon resonances have usually been treated independently, although these processes are for some materials strongly coupled. In such a case the plasmon frequency is shifted significantly because of interband transitions; higher lying interband transitions shift the plasmon frequency to lower values, and lower lying interband transitions shift the plasmon frequency toward higher values, as can be seen from Eq. (82). This effect leads to obvious complications in the interpretation of experimental energy loss data since oscillator strengths for the single-electron excitations are not normally known; interpretations for samples exhibiting this coupling are facilitated by considering the energy loss function obtained from optical reflectivity data.

Subsidiary maxima in the true secondary distribution result from the bulk Auger effect, Auger neutralization of adsorbed species and umklapp processes. The energies of the Auger electrons emitted are determined by the participating energy levels in the solid and atomic levels of adsorbed ions, as expressed in Eq. (92). The energies of the umklapp electrons may be determined from the energy loss value given in Eq. (33) minus the energy required to raise the ejected electron from its initial state to the vacuum level. It is important to note that the excitation of umklapp processes necessarily implies an energy and momentum loss for the primary electron and the ejection of one of the metal electrons; this means that one should be able to correlate peaks in the characteristic loss region of the secondary electron energy distribution with subsidiary maxima in the secondary region representing the corresponding umklapp electrons.

CHAPTER III

EXPERIMENTAL APPROACH

The nature of the various elastic and inelastic scattering mechanisms may in part be deduced from an interpretation of the energy distributions of electrons back-scattered from well defined solid surfaces. It was, therefore, the objective of the experimental part of this study to set up apparatus and develop techniques for obtaining these secondary electron energy distributions for slow electrons reflected from the (110) surface of tungsten. In this chapter the instrumentation is described, and procedures for obtaining the experimental distributions are presented; in addition, the sample preparation procedures for the tungsten crystal are outlined, and the characterization of surface states using LEED patterns is discussed.

Apparatus and Procedures

Electron Optics

The LEED patterns and secondary electron energy distributions were obtained using a post-acceleration type low-energy electron diffraction optics; this optics is similar to the earlier version pictured in Figure 1, except that the planar grids and screen have been replaced by spherical elements and an extra grid has been added to achieve better energy resolution. This optics can be used in the normal fashion to obtain LEED patterns from the surfaces of interest, or, with the addition of the third grid and changes in the electronics to be described, the optics can be used as a spherical retarding field analyzer to obtain energy distribution curves for electrons back-reflected from the sample into the solid angle subtended by the optics.

The electron optics and associated electronics are illustrated schematically in Fig. 5. The optics, which was manufactured by Varian Associates, consists of an electron gun, three spherical tungsten mesh grids and a spherical fluorescent screen. Characteristics to be noted are as follows. The electron gun is made up of an indirectly heated, bariated nickel cathode, a draw-out aperture, and a three element, concentric tube, uni-potential lens; this gun produces a focused beam of electrons with an energy range of about 5 to 500 ev and with a spot size of approximately 0.5 mm. The spherical grids have a radius of 2 1/2 inches and subtend about one third of a hemisphere; they are 100 mesh woven from 1 mil. nickel plated tungsten wire and have high transparency. The fluorescent screen has a radius of 2 3/4 inches and is coated with G.E. P-4 phosphor. The fluorescent screen and the three grids each have a hole punched in the center to allow for the drift tube of the electron gun.

A special optics power supply package was designed which provides the fixed and programmed voltages necessary for observing LEED

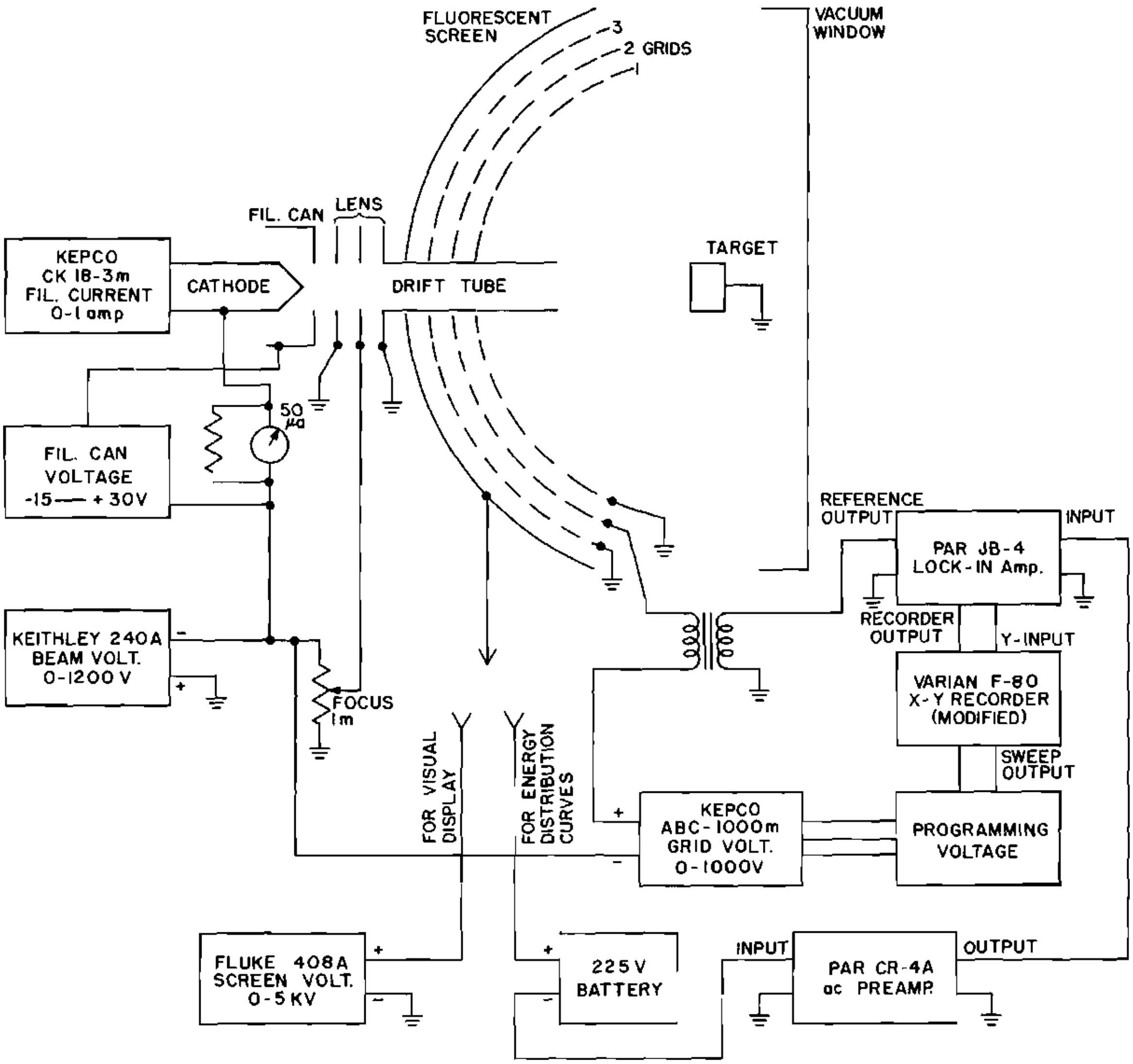

Figure 5. Schematic Diagram of LEED Optics and Electronics for Obtaining Diffraction Patterns and Electron Energy Distribution Curves.

patterns and obtaining the energy distribution curves. The negative cathode potential is supplied by a Keithley Model 240-A high voltage dc power supply which has a digitally selected output of 0-1200 volts. The current for heating the filament (approximately 1 amp) is supplied by a Kepco Model CK 18-3M dc supply which can be operated in a constant current mode or programmed to maintain constant emission current. Additional circuitry was provided to give the proper voltages for draw-out and focusing the electron gun and for reading cathode emission, as indicated in Fig. 5. For observing LEED patterns the fluorescent screen voltage is supplied by a Fluke Model 408 high voltage dc supply. The suppressor grid voltage is supplied by the grid voltage programming supply which can be controlled manually, giving a constant suppressor voltage for observing LEED patterns, or which can be programmed to give a linear voltage sweep for obtaining the energy distribution curves. This supply consists of a Kepco Model ABC 1000M high voltage supply which is floated at cathode potential and which can be programmed by an external signal. The Varian Model F-80 X-Y recorder was modified to provide externally a signal that is proportional to the displacement of the recorder carriage in the X-direction, and this signal is used to program the Kepco supply. The modification consists of the addition of a potentiometer which is driven by the carriage of the recorder and circuitry coupling this potentiometer with the Kepco supply. Thus, if the recorder is set to sweep linearly with respect to time, the suppressor grid potential will correspondingly be swept linearly from cathode potential toward zero. This scheme for coupling the recorder and power supply was necessitated by the fact that the suppressor grid supply must float at cathode potentials of greater than 500 volts, which exceeds the floating capability of most recorders.

For obtaining LEED patterns, the operation of the electron optics is as follows. Electrons are accelerated in the electron gun to form a focused beam incident on the grounded sample with the desired energy. These electrons are elastically and inelastically scattered, and the portion of the secondary electrons emitted into the solid angle subtended by the first grid are collected in the optics assembly. The first grid and drift tube are maintained at ground potential so that electrons incident on the sample and reflected into the grid assembly move in a region free of electrostatic fields, the potential on the second or suppressor grid is set at a negative value near cathode potential so that electrons which have lost energy are eliminated from the pattern. Electrons which have sufficient energy to overcome this barrier are passed through the third grid and accelerated by the large positive potential on the fluorescent screen to excite the phosphor and give a visible diffraction pattern. This pattern can be observed visually or photographed through the front vacuum window.

The cut-off characteristic of the suppressor grid is not ideally sharp. A realization of the ideal characteristic would mean that setting the suppressor grid potential equal to the cathode potential should eliminate even the elastically scattered electrons from the pattern. However, in practice one finds for the usual two-grid optics that this complete repelling of the reflected current requires that the suppressor grid be set several volts below cathode potential because of the nature of the equipotential surfaces associated with the grid and because of field penetration arising from the large positive voltage on the fluorescent screen. In order to reduce the effect of field penetration, the optics used in this study was modified to include a third shield grid between the suppressor grid and the fluorescent screen. This shield grid is normally operated at ground potential, and, using this grid, it was found that the cut-off characteristic is improved and that the three-grid LEED optics could also be used to obtain energy distribution curves for the secondary electrons.

To understand the procedure used to generate the energy distribution curves, one must first note that the curve obtained by plotting the current collected by the fluorescent screen as a function of suppressor voltage is a retarding field curve; that is, this curve represents electrons with energy greater than some value E plotted against E. This type of curve does not display conveniently much of the fine structure due to energy loss phenomena, and one would like to have the derivative of the retarding field curve, which would be a plot of current per unit energy versus electron energy. The required derivative may be obtained by graphical means or using analog computer methods, but, as shown in the early stages of this study, these methods do not yield results of sufficient accuracy and reproducibility to be useful in examining the electron interaction mechanisms. However, the problem of differentiating the retarding field curve was finally solved by adapting to the configuration of the LEED optics an ac differentiation scheme previously described by Leder and Simpson[28] and Spicer and Berglund.[29] According to this scheme, a small sinusoidal signal is added to the suppressor grid potential with the result that the collected secondary electron current is slightly modulated. One then finds that the ac component of the collected current with the same frequency as the modulating signal is proportional to the first derivative of the retarding field curve. Further, the higher order derivatives of this curve may be obtained simply by detecting the higher order harmonics present in the current collected by the fluorescent screen.

The decomposition of the retarding field curve into its various derivatives is equivalent to taking a Taylor's series expansion of the curve about a reference point which is treated as a variable parameter. This expansion may be indicated schematically as

$$F(E) = F_{(E_o)} + \left.\frac{dF}{dE}\right|_{E=E_o} (E-E_o) + \frac{1}{2} \left.\frac{d^2F}{dE^2}\right|_{E=E_o} (E-E_o)^2 + \cdots . \tag{93}$$

To obtain the derivatives at some fixed energy value, one chooses E_o to be that particular value and notes that the difference $(E - E_o)$ is the sinusoidal modulating signal present on the suppressor grid. Assuming that the modulating signal is small, the first derivative may be determined within a multiplicative factor by experimentally measuring the ac component of F(E) at the reference frequency. Similarly, the second derivative would be proportional to the signal strength of the second harmonic because of the $(E - E_o)^2$ term. To generate the complete curves corresponding to these derivatives, one thinks of scanning E_o slowly over all energy values of interest, which is effected experimentally by scanning the suppressor voltage from cathode potential toward zero.

Returning to the schematic diagram of Fig. 5, the actual operation of the LEED optics as a regarding field analyzer may be explained. The electron gun is set to give a focused beam of electrons incident on the sample with the desired energy. The drift tube, first and third grids and sample are kept at ground potential as for observing LEED patterns. A modulating signal is derived from the reference output of a Princeton Applied Research Model JB-4 lock-in amplifier. This signal is added to the suppressor grid potential through an audio output transformer included for voltage isolation. A typical ac signal at the grid is one volt peak-to-peak at 80 cps. The fluorescent screen is used to collect the modulated secondary electrons, and, in this case, the Fluke high voltage supply is replaced by a 225 volt battery. To obtain the first derivative of the retarding field curve, the component of the collected current at the reference frequency is amplified by the Princeton Applied Research Model CR-4A preamplifier and detected using the PAR lock-in amplifier. The output of the lock-in amplifier is fed into the Y-axis input of the X-Y recorder, and the energy distribution curves are plotted as the recorder sweeps (simultaneously causing the suppressor grid voltage to be swept linearly from cathode potential toward zero).

Following the above procedure one obtains secondary electron energy distribution curves that generally have the form illustrated in Figure 2. The detailed features of these curves are determined by the various elastic and inelastic scattering processes and by several instrumental effects, including contact potential differences and the energy resolution of the gun and grid system.

Referring again to Fig. 2, one effect of the finite energy resolution of the electron optics is seen as the apparent energy half-width of the elastically reflected primary peak (region I). The half-width increases linearly with electron energy as shown in Fig. 6. This behavior is discussed by Simpson[75] and is shown to be characteristic of electrostatic analyzers in general. From Fig. 6, one determines that the relative resolution $\Delta E/E$ is approximately 0.02, and the zero energy extrapolation gives a ΔE of 0.3 ev which may be compared with the quoted energy spread for the Varian electron gun of 0.2 ev.

For the configuration of the LEED optics, the limited resolution

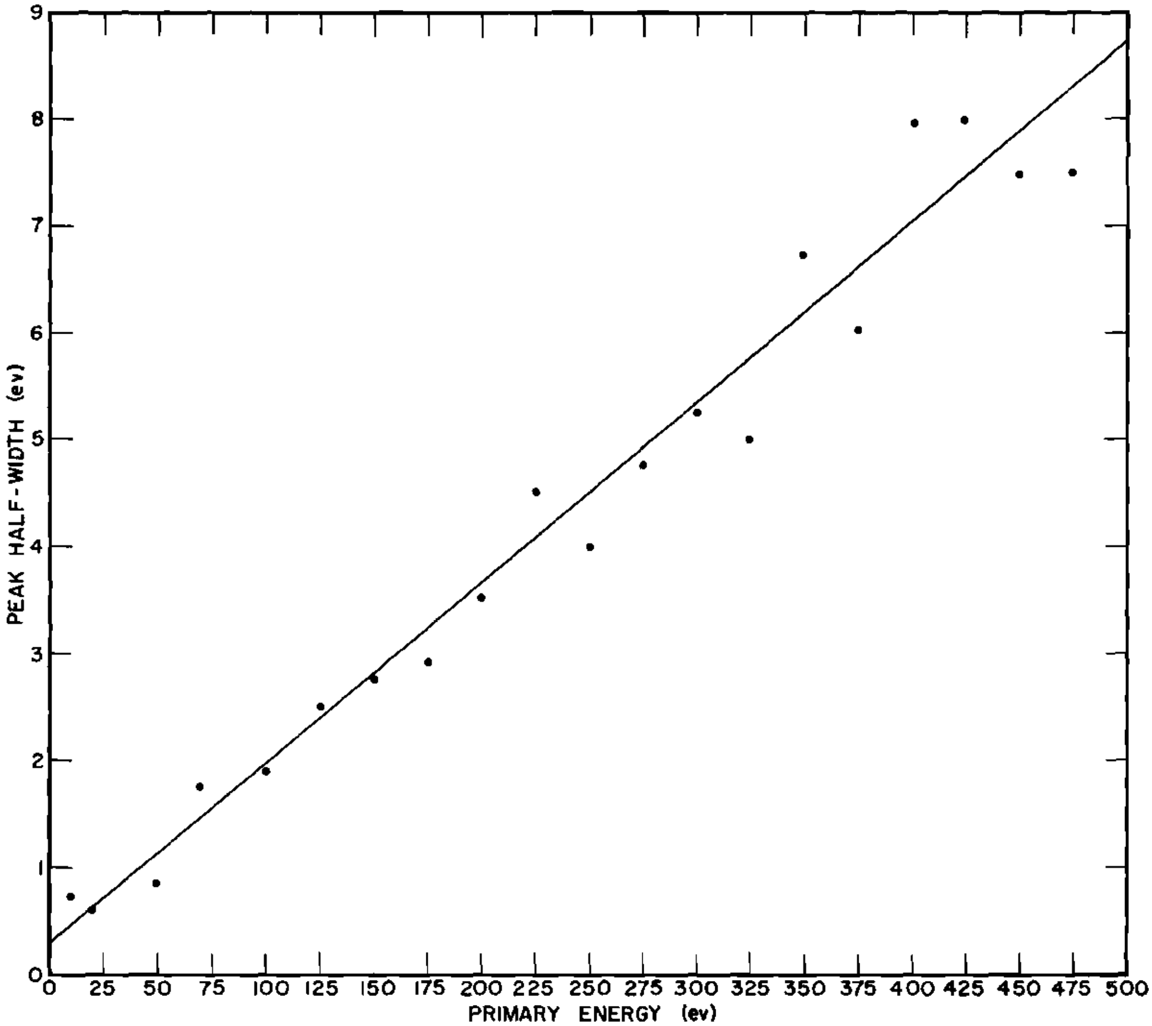

Figure 6. Energy Resolution of Electron Optics as a Function of Electron Energy.

arises from the fact that equipotential surfaces generated by the repeller grid are not perfectly spherical, but conform somewhat to the pattern of the grid wires. This means that even radially incident electrons have components of momentum both normal and parallel to these equipotential surfaces. The potential barrier is effective only in reducing the normal component of momentum, but this is sufficient to prevent the electrons from penetrating the grid and being collected. Moreover, electrons which appear to be non-normally incident are stopped by lower values of the suppressor voltage than are electrons which appear to be normally incident. Thus, the effects of this spacial variation of the equipotential surface on a radially incident, monochromatic beam of electrons would be to give an apparent broadening to the distribution and to effectively shift the maximum in the distribution toward lower energy values. This shift of the maximum in the distribution also increases with electron energy, and it may be seen in the curve of Fig. 2 which shows a maximum for the reflected primary peak of 98 ev, when, in fact, the correct electron energy should be approximately 100 ev. Finally, it must be noted that field penetration arising from the fluorescent screen potential acts such as to shift the apparent energies toward larger values, but, with the addition of the third shield grid, this effect is essentially eliminated.

The complete energy distribution curves reveal a difference in contact potential between the cathode and the sample and a second contact potential difference between the sample and the first grid of the LEED optics. The first difference results in a decrease of the actual energy of the electron beam incident on the sample as compared with the energy value computed from a measure of the accelerating voltage; however, this effect is not easily separated from the shift in energy values resulting from the limited energy resolution of the optics. The second difference has the effect of shifting the zero of energy for electrons emitted from the sample relative to the actual zero of energy measured by the analyzer; this difference in contact potential is displayed as the width of the sharp peak on the low-energy side of the true secondary peak of Fig. 2. The peak itself represents tertiary electrons emitted from the first grid as a result of collisions by low-energy secondaries. The tertiary peak is observed in these data because the work function of the sample was greater than the work function of the grid; if this situation were reversed, the tertiary electron peak would have been hidden under the true secondary peak. The analyzer zero has been indicated as zero on the curve of Fig. 2; the zero of energy for the electrons emitted from the sample occurs approximately at the dip between the tertiary electron peak and the true secondary peak.

Vacuum System and Accessories

In order to obtain and maintain known surface states for the tungsten sample, all measurements were made in ultrahigh vacuum using the system pictured in Fig. 7. This stainless steel system, which was cus-

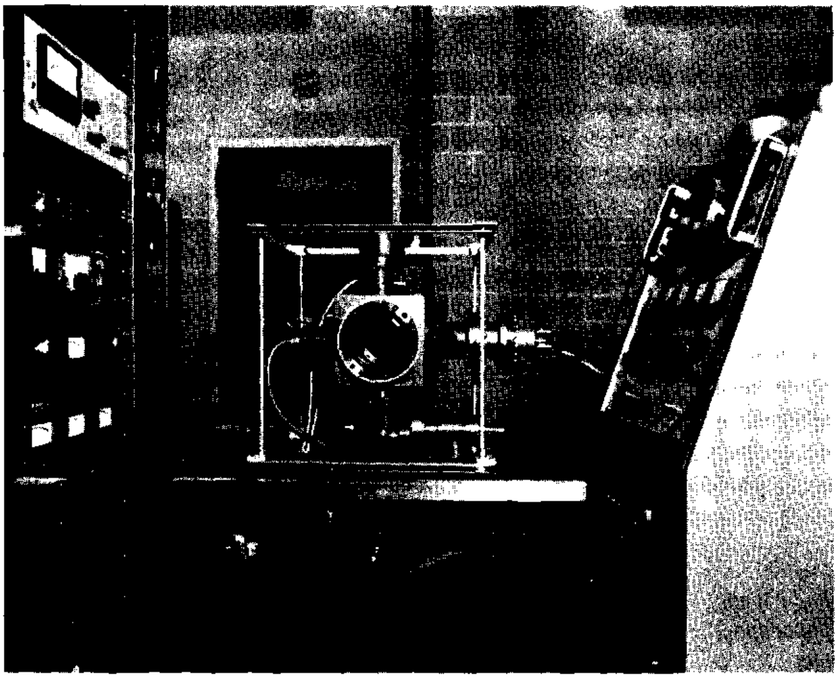

(a)

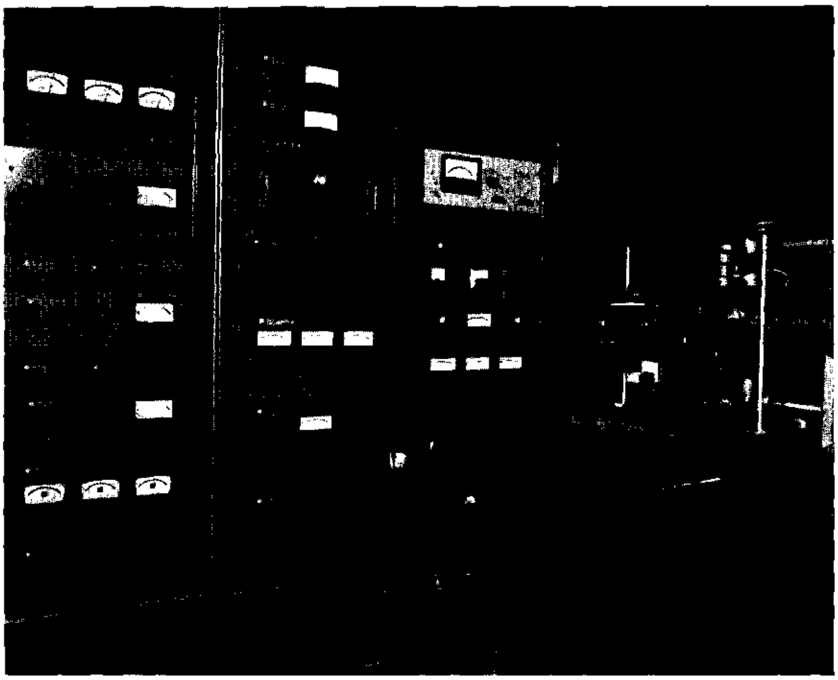

(b)

Figure 7. Photographs of Apparatus (a) Showing Experimental Chamber and (b) Showing Electronics Console.

tom fabricated by Varian Associates, was designed to provide a clean, low-pressure environment with provisions for sample cleaning and admitting known quantities of high-purity gases for adsorption studies. Accessories added to the system include an automatic servo-operated gas delivery system and a quadrupole type residual gas analyzer.

The pumping system, illustrated schematically in Fig. 8, consists of three Varian vac-ion pumps giving a total pumping speed of 138 ℓ/s. An 80 ℓ/s pump is used to evacuate the experimental chamber. A second pump with a speed of 50 ℓ/s is used to evacuate the gas delivery system, or it may be used in parallel with the 80 ℓ/s pump to provide additional pumping speed for the experimental chamber. The third pump with a speed of 8 ℓ/s is used to keep the line clean connecting the main system with the sorption type roughing pumps. All three pumps can be valved off from the chamber for admitting gases at higher pressures. Components used in the system are designed to withstand a 250° C bakeout, and pressures of 2×10^{-10} torr may be achieved in routine operation. Total pressure measurements are made using a Varian nude ionization gauge and controller.

Provisions for sample cleaning include a positive ion bombardment gun with controller and a high current power supply for direct resistance heating of experimental samples. For tungsten only the direct resistance heating was needed; cleaning procedures to be described involved reactions of impurities with selected gases at elevated tempera-

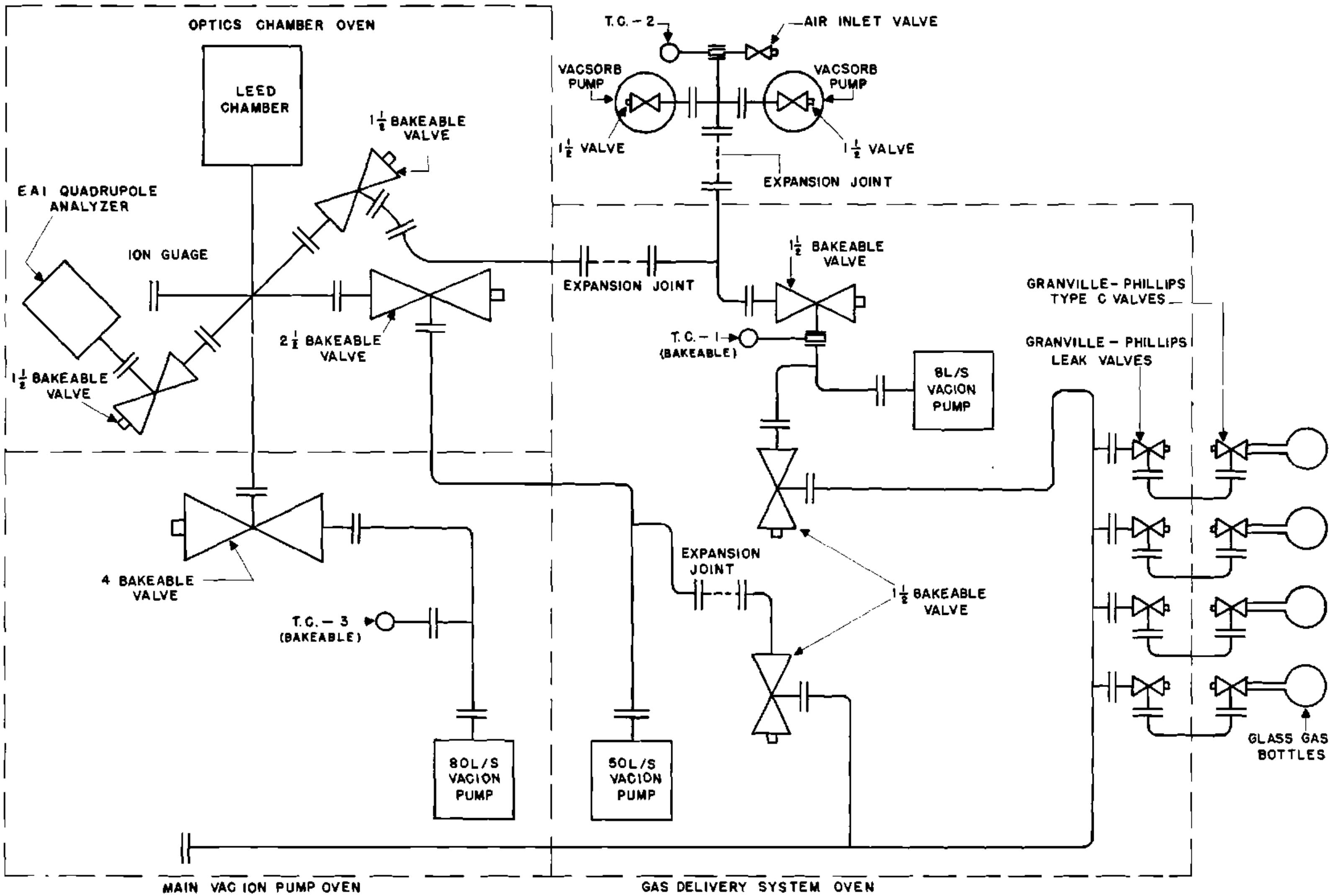

Figure 8. Schematic Diagram of LEED Vacuum System.

tures and flash filament desorption of adsorbed species.

To facilitate the admission of ultra-pure gases, the vacuum system was equipped with a servo-controlled gas delivery system built around four Granville-Phillips automatic pressure controlled valves. These valves could be controlled automatically using the Varian ionization gauge to maintain constant total pressure for a single gas, or they could be controlled manually in conjunction with the residual gas analyzer to maintain a distribution of several gases in the residual background.

The quadrupole residual gas analyzer was manufactured by Electronic Associates, Inc. This instrument, which is a Series 200 with an axial beam ionizer, was found to be extremely useful for monitoring the system residual background, for checking the purity of gases admitted to the system, and for examining the distribution of gases desorbed from the tungsten sample at elevated temperatures.

For operation of the electron optics both as a LEED device and as an energy analyzer, it was necessary to reduce the stray magnetic fields in the region of the experimental chamber. Sources of these fields are pump magnets and the earth's field, and the magnitude varied fairly smoothly from 1.5 gauss at the bottom of the chamber to 0.5 gauss at the top. This field compensation may be crudely achieved using small trim magnets, but more satisfactory operation was achieved with cube coils which could be used to null out the stray fields uniformly.

Sample Surface Conditions

Sample Preparation

The tungsten sample used in this study was cut from a zone refined single-crystal rod obtained from Metals Research Ltd. A 1/2 inch long section of the 1/4 inch diameter rod was oriented roughly by x-ray diffraction using a special crystal holder described by Bond.[76] From this rod, single-crystal slabs with thicknesses of about 2 mm were cut using a diamond saw; these slabs were oriented with surfaces approximately parallel to the (110) crystallographic planes.

In addition to adjustments for orientation changes, the Bond crystal holder provides a reference surface so that flat surfaces may be conveniently ground on experimental samples. Thus, for orientation corrections, the tungsten slabs were individually mounted in the Bond holder and oriented by x-ray diffraction; the surfaces were then ground on fine emery cloth until both of the planar surfaces on each slab were parallel to the (110) crystallographic planes within an error of less than one-half a degree. The thicknesses of the finished samples were approximately 0.5 mm.

The mechanical polishing operation leaves damaged layers near the surfaces of the crystals, so that it was necessary to chemically polish the crystal slabs to remove damaged material. The etching solution used was made by dissolving 10 gm potassium ferricyanide and 10 gm potassium hydroxide in 100 ml warm water. This solution was recommended for developing grain boundaries on polycrystalline tungsten samples,[77] but, in the absence of grain boundaries in the single-crystal slabs, the solution produced bright, smooth surfaces.

Three of the polished single-crystal samples were heliarc welded to 40 mil diameter tungsten wires for mounting in the Varian LEED crystal manipulator. These samples were again chemically polished as before. One of these samples was used in preliminary measurements, one was inadvertently damaged, and the third was used for the measurements reported in this dissertation.

Surface Characterization

Once the tungsten sample was installed in the ultrahigh vacuum system, volatile impurities and adsorbed gases could be removed from the surfaces by flash heating to temperatures above 2000°C. This procedure has previously been used[27] under the assumption that the surfaces are left atomically clean. However, samples cut from zone refined ingots of tungsten contain carbon as a natural bulk impurity which diffuses toward the surface as a sample is heated.

The presence of carbon on the tungsten (110) surface is characterized by the diffraction pattern shown in Fig. 9(a). This pattern was obtained after the sample had been heated extensively (above 2000° C). The six bright reflections forming parts of the sides of a diamond shaped figure are characteristic of the clean surface for 220 ev incident electrons; this portion of the pattern may be compared with the clean

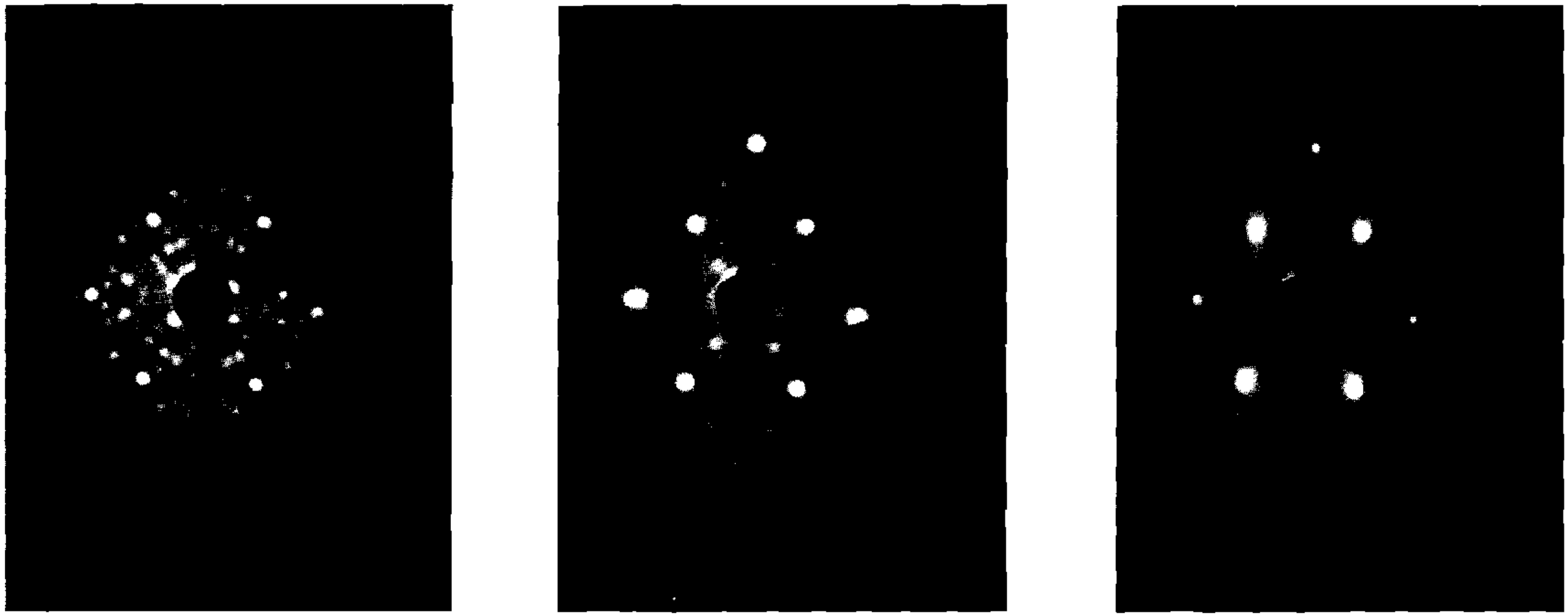

(a) (b) (c)

Figure 9. LEED Patterns of Tungsten (110) Surface for 220 Volt Electrons at Successive Stages of Cleaning. (a) Shows Carbon Contamination, (b) Shows Adsorbed Oxygen, (c) Shows Clean Tungsten

surface pattern shown in Fig. 9(c). Reflections contributing to the complex but well ordered background in the pattern of Fig. 9(a) may be attributed to the superimposed lattice of an impurity, but, of course, none of the features in the pattern indicate that this impurity is carbon. However, when the crystal is flash heated above 2000° C with this pattern present and the mass spectrum of the desorbed species continuously displayed using the residual gas analyzer, one observes an increase in the mass peak corresponding to m/e = 12, the peak characteristic of carbon. Further, if oxygen is admitted to the system with the carbon contaminated sample at an elevated temperature and the sample is subsequently flash heated, one finds a strong increase in the carbon monoxide peak, m/e = 28. These observations were confirmed by Stern,[33] who also investigated the reactions of hydrogen with carbon on the tungsten (110) surface.

The reaction of oxygen with the carbon impurity to form carbon monoxide can be used to remove the carbon from the tungsten (110) surface. This is accomplished by heating the crystal to 1000°C for about 20 min in a residual background of 5×10^{-8} torr of oxygen and then flash heating the crystal to a temperature of 1700°C to desorb the carbon monoxide. During the final heating, the sample must reach a high enough temperature so that the carbon monoxide is desorbed, but the flashing must be sufficiently mild so that carbon does not again diffuse to the surface. The clean surface thus obtained is characterized by the

LEED pattern shown in Fig. 9(c).

If the clean tungsten surface is exposed to oxygen, new diffraction features develop as can be seen by comparing the LEED pattern of Fig. 9(b) with the clean surface pattern. These new half-order reflections are characteristic of the oxygen adsorption structure and vary in intensity with oxygen coverage. As oxygen is adsorbed, the intensity of these reflections increases to a maximum (about half the intensity of the clean surface reflections) at a coverage of about one-half a monolayer. As coverage is further increased, the intensity of the half-order reflections decreases, with additional features appearing at about three-fourths of a monolayer of oxygen. Finally, when a full monolayer coverage is reached the half-order reflections have completely disappeared, and the pattern observed is essentially identical to that corresponding to the clean surface.

The two-dimensional structures giving rise to the diffraction patterns of Fig. 9 may be inferred following the procedure outlined in Chapter II. The structure of the impurity carbon on the tungsten (110) surface was determined by Stern,[33] and the oxygen adsorption structures on this surface were investigated by Germer, Stern and MacRae.[32] The structures which one determines in this way are sometimes not unique in that more than one 2-D structure may give rise to the same diffraction patterns, but arguments based on adsorption kinetics can frequently be used to narrow the consideration to a single structure.

Furthermore, the LEED patterns can be used to characterize these ordered, adsorbed states provided one has first established a procedure for cleaning the surfaces and provided that the LEED patterns can be correlated with other measurements to identify the adsorbed species. In this study residual gas analysis has been used to monitor the composition of desorbed species, and some features in the inelastic energy distributions have been used along with LEED patterns to characterize these surfaces.

CHAPTER IV

RESULTS AND DISCUSSION

The apparatus and procedures described in the previous chapter may be used routinely to obtain LEED patterns and secondary electron energy distributions. These data provide a means of characterizing experimental surfaces so that interpretations of the elastic and inelastic scattering may be undertaken without the added complexity of variations in experimental data arising from unknown surface conditions. It is thus the purpose of this chapter to explain the features of the energy distribution curves, such as illustrated in Fig. 2, in terms of the scattering mechanisms discussed in Chapter II. In this discussion, the elastic diffraction of the slow electrons is not considered; rather, the emphasis is on those processes giving rise to characteristic loss peaks and subsidiary maxima in the true secondary distribution. Further, the effects of surface conditions on some features of the energy distributions are described to demonstrate the potential application of inelastic scattering as a tool for surface studies complementary to LEED.

Characteristic Energy Losses

A section of an energy distribution curve for 150 volt electrons scattered from the clean tungsten (110) surface is shown in Fig. 10.

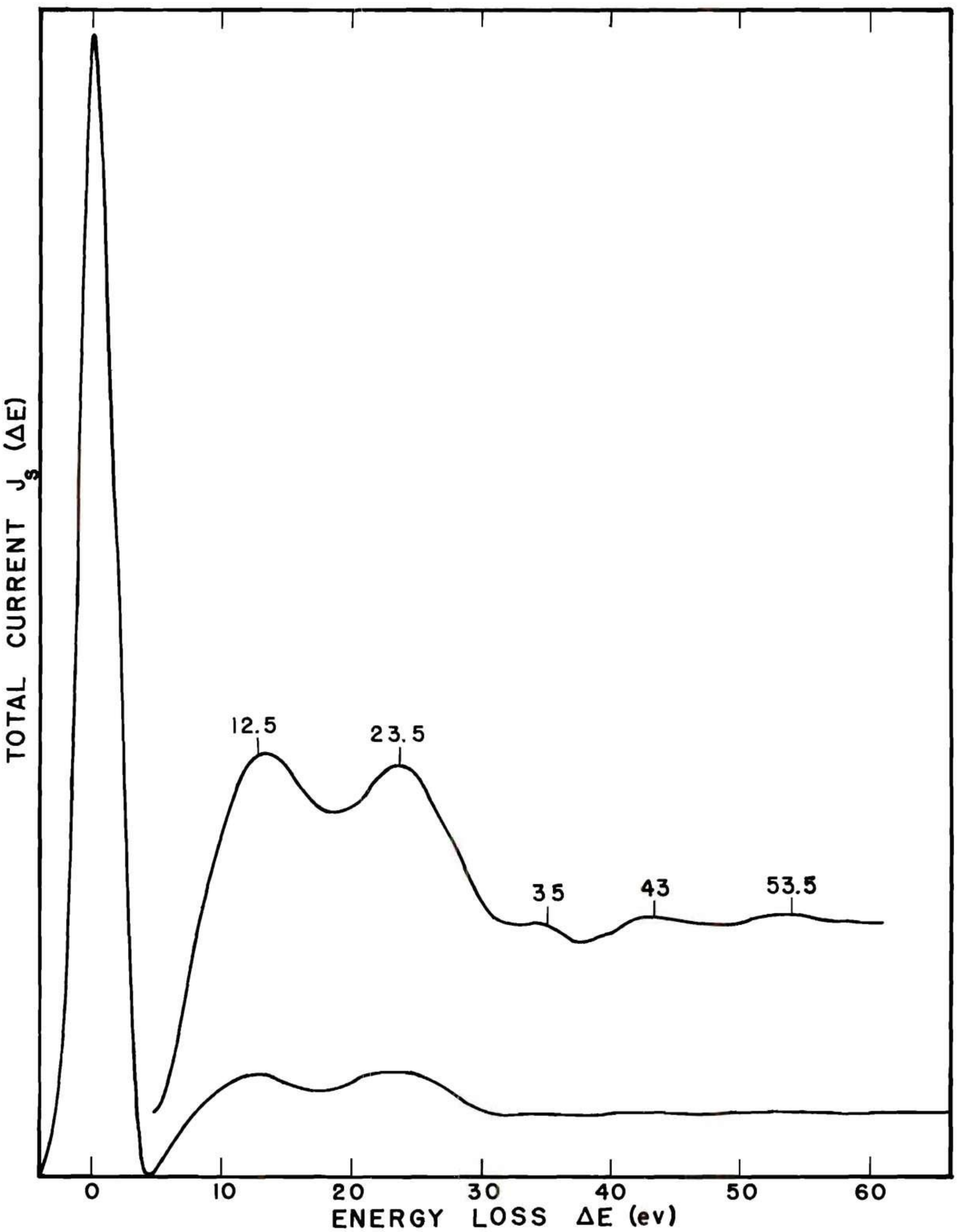

Figure 10. Energy Distribution for Clean Tungsten (110) Surface with Amplified Characteristic Loss Region. 150 Volt Primary Electrons.

The characteristic loss region of this curve is amplified to emphasize the losses, and energy loss values are indicated for the various peaks. Both plasma resonances and single-electron excitations give rise to the observed losses, but, before proceeding with the identification of the loss peaks, it is convenient to look at the energy losses to be expected for tungsten on the basis of the theoretical results of Chapter II.

The free-electron energies for the collective excitations may be determined from Eqs. (77) and (90) for the bulk and surface plasmons respectively. These relations may be applied to materials for which the plasmon frequencies are not modified by band-band transitions (i. e., metals with nearly free valence electrons and tightly bound core electrons) and would not be expected to apply in the case of tungsten. However, the values of energy losses predicted by the free-electron expressions agree reasonably well with experimental values which, as Pines[58] has suggested, may be the result of cancellation between the effects of low-frequency and high-frequency single-electron excitations. Furthermore, the oscillator strengths of these single-electron transitions are not known for tungsten, so the free-electron equations are used as a qualitative guide in identifying the collective losses. From Eq. (77) one predicts a loss $\hbar\omega$ corresponding to the excitation of a bulk plasmon using the expression for ω_p given in Eq. (A-37),

$$\omega_p = \left(\frac{4\pi e^2 n}{m} \right)^{1/2} , \tag{94}$$

where n is the electron density and m is taken to be the free-electron mass. For tungsten's body centered cubic lattice with a lattice constant of 3.16 Å and two atoms per unit cell, one obtains an electron density of 3.8×10^{23} electrons/cm^3 assuming that for each atom the four 5d- and two 6s-electrons participate as free-electrons in the collective oscillation. This gives a plasmon frequency of 3.48×10^{16} sec^{-1}, and, neglecting the small dispersion, the energy loss for the primary electron is 22.9 ev. For a planar surface bounded by vacuum, the surface resonance frequency would be related to ω_p by Eq. (90) in the free-electron model, and the corresponding loss by the incident electron is 16.2 ev.

Characteristic energy loss values associated with the excitation of single-electron transitions may be determined from Eq. (33). This expression can be rewritten in terms of the lattice constant A as

$$\Delta E_n \approx \frac{2\pi^2 \hbar^2}{mA^2} n^2 , \tag{95}$$

where $n^2 = n_1^2 + n_2^2 + n_3^2$ and n_1, n_2, n_3 are integers. These integers are analogous to the Miller indices used in x-ray diffraction, and it might be assumed, as already mentioned, that for certain values of these indices the excitations would be forbidden due to cancellation of out-of-phase contributions to the structure factor from scattering centers within the individual unit cells. However, this assumption applies mainly to perfect crystals and would not be expected to hold for scattering from surfaces. Thus, one obtains for tungsten with A = 3.16 Å, $\Delta E_n = 15\ n^2$ ev and, taking $[n_1 n_2 n_3]$ = [100], [110], [111], [200], one predicts energy losses of 15, 30, 45, 60 ev respectively.

Comparing these predictions with the experimental losses noted in Fig. 10, one finds that the loss value of 22.9 ev for the bulk plasmon excitation agrees well with the loss value of 23.5 ev measured for the second loss peak in the figure. The first loss peak on this curve has a loss value of 12.5 ev which may correspond to the theoretical value for the surface plasmon of 16.2 ev. Although the agreement here is not as good as for the bulk plasmon, this peak corresponds to a surface effect as will be shown. Several of the predicted loss peaks due to interband type transitions also agree reasonably well with the values of the last peaks shown in Fig. 10. The theoretical loss values and a number of measured values are summarized in Table 1 for both the plasma resonances and single-electron transitions in tungsten. In this table the peaks are grouped in columns according to the energy loss values and not necessarily according to the energy loss mechanisms responsible for the peaks.

The energy loss value alone is generally insufficient information for determining whether a particular loss peak is the result of a

Table 1. Theoretical and Measured Energy Loss Values for Both Interband Type Transitions and Plasma Resonances in Tungsten.

Source	Energy Loss Values (ev)					Explanation
Eqs. (77) and (90) (Calculated)	16.2	22.9				Plasma Resonance
Eq. (95) (Calculated)	15		30	45	60	Umklapp Process
Present Work (Fig. 10) (Measured)	12.5	23.5	35	43	53.5	Clean (110) Surface
Harrower[27] (Measured)	14.8	26.8		46.4	58.0	Polycrystalline Ribbon
Powell et al.[36] (Measured)	10.6	24.3		43.3	52.8	Polycrystalline Wire

single-electron transition or the excitation of a plasma resonance. As noted above, an umklapp type loss is predicted with an energy of 15 ev, and the computed value for the surface plasmon loss is 16.2 ev. A loss peak is measured at 12.5 ev, and this peak could result from the umklapp transition, a surface plasmon, or both. However, this peak has been identified with the surface plasmon because of a strong dependence of the relative intensity of this peak on incident beam voltage and variations in the intensity with changes in surface conditions.

A sequence of energy distribution curves for clean tungsten was obtained for different incident beam energies. The characteristic loss regions of these curves were amplified and are displayed in Fig. 11. For an incident energy of 150 ev, the surface and bulk plasmon peaks are roughly the same size. However, as the voltage of the primary electrons is increased, there is a tendency for the bulk plasmon peak to grow in intensity relative to the surface peak. This implies that as the electron energy increases, and consequently the penetration depth, there is a tendency for bulk modes to be excited with higher probability than the surface modes. One would expect this behavior, as may be seen by referring to the excitation probability for bulk and surface resonances given in Eq. (88). The bulk plasmon excitation rate is proportional to the equivalent path length in the solid, which, in this case, would be related to the penetration depth; the surface excitation, on the other hand, is independent of the distance traveled in the material.

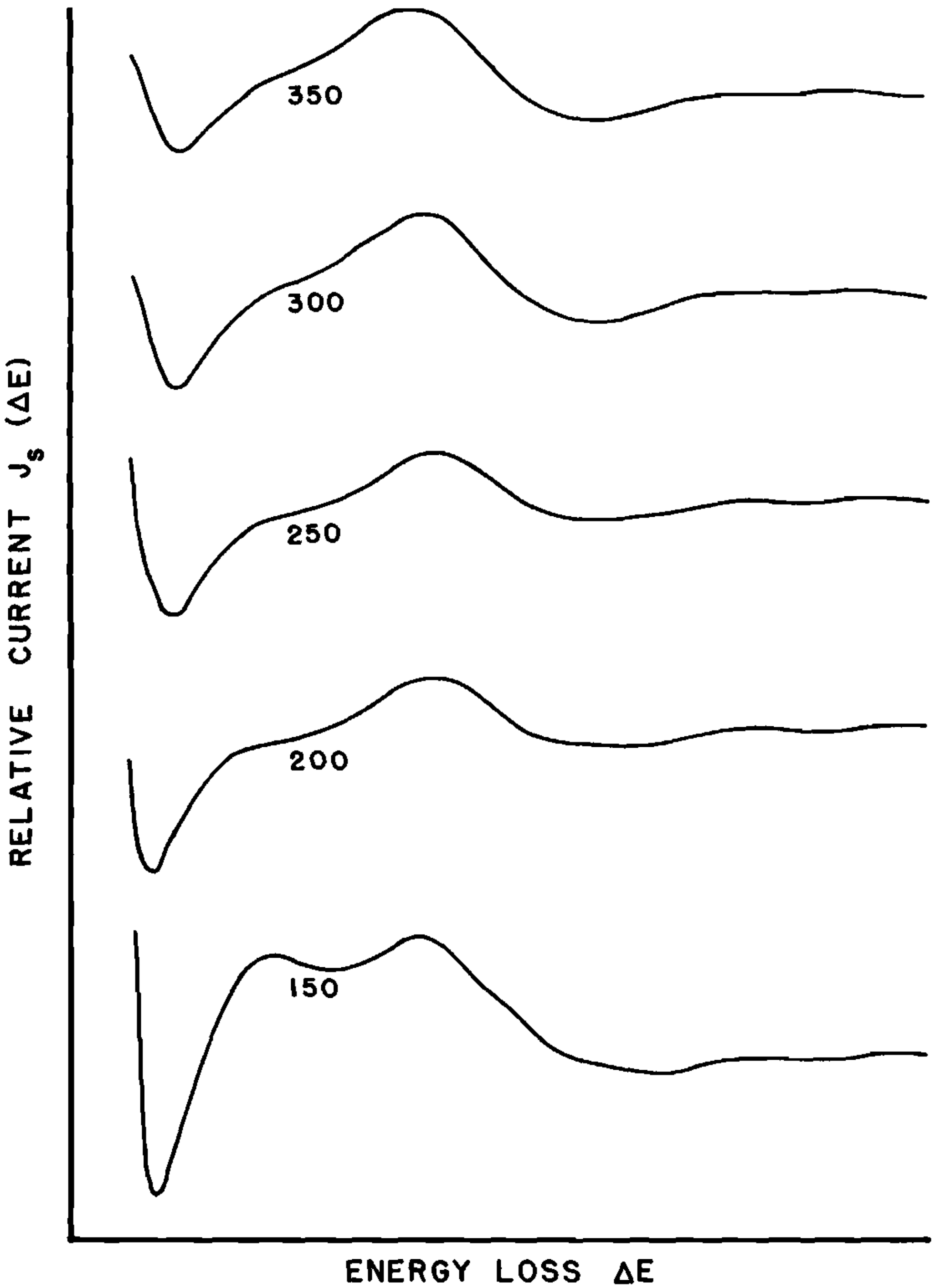

Figure 11. Sequence of Energy Loss Curves for Clean Surface Showing the Relative Intensities of the Bulk and Surface Plasmon Peaks for Incident Beam Energies Varying from 150 to 350 ev.

This means that, as the penetration depth is increased, the excitation probability for the bulk resonance should increase, and the excitation probability for the surface resonance should remain constant.

The relationship of bulk and surface plasmon intensities shown in Fig. 11 is complicated slightly by the fact that the total integrated intensity of the plasmon peaks decreases with increasing primary energy, as is evident in the figure. This decrease is attributed to the dependence of the total plasmon peak intensity on the intensity of the elastically reflected primary peak which may be explained as follows. The angular dispersion of even slow electrons losing energy in plasmon excitations is small, so that two scattering events are required for the electrons to be back-reflected and collected in the LEED optics. If the electrons are first elastically diffracted to form the diffraction maxima and secondly are scattered out of the diffracted beams by plasmon excitation, then the intensity of the electrons losing energy in the excitation would be proportional to the intensity of electrons included in the diffracted beams. This means that the intensity of the plasmon loss peaks would be proportional to the intensity of the elastically diffracted primary peak. If, on the other hand, the electrons first lose energy in the inelastic event and are then elastically diffracted, the diffraction conditions satisfied would differ from the diffraction conditions satisfied by the primary electrons, and the proportional relationship would not be expected. In a sequence of energy distributions similar to Fig. 11 but showing elastic peaks along with the characteristic loss peaks it was observed that the intensity of the plasmon peaks was proportional to the intensity of the elastic peak. For the energy range considered in Fig. 11, the intensity of the elastic peak showed a general decrease with increasing primary energy, and the plasmon peak intensities decreased correspondingly. It must be noted, however, that this observation was purely qualitative because of difficulties in determining the integrated intensities of the plasmon peaks due to unknown background contributions. Moreover, the question involving the sequence of the elastic and inelastic scattering events can be adequately resolved only by making measurements of angular distributions as outlined in Chapter II.

Further evidence for the proportional dependence of the plasmon loss intensity on the elastically reflected primary intensity is presented in Fig. 12. This figure shows the effects of oxygen adsorption on the elastic peak and the plasmon peaks. The oxygen coverage was approximately one monolayer as indicated by LEED patterns. With oxygen exposure the intensity of the elastic peak more than doubled with corresponding increases in the intensities of the plasmon peaks.

It may also be noted in Fig. 12 that the intensity of the surface plasmon peak has increased with oxygen exposure relative to the intensity of the bulk plasmon peak, which at first thought seems to contradict Stern and Ferrell's prediction[70] that the surface plasmon intensity

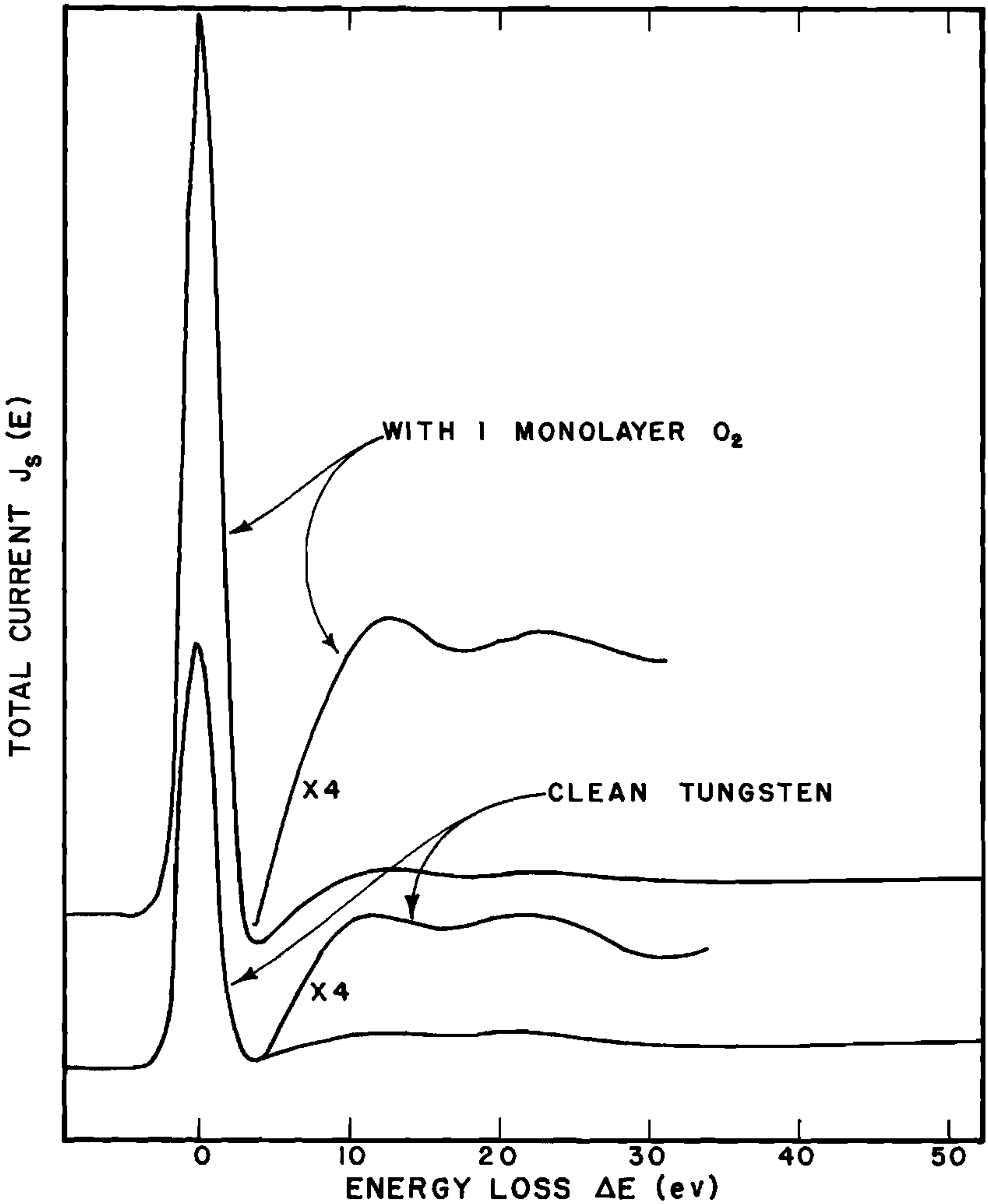

Figure 12. Energy Loss Curves for 130 Volt Electrons Showing the Effect of Adsorbed Oxygen on the Elastically Reflected Primary Peak and the Plasmon Peaks.

should decrease with the formation of a dielectric film at the surface. In this regard several points must be considered. First, according to Stern and Ferrell's calculation, the quenching of the surface plasmon loss peak should occur for oxide film thicknesses on the order of 20 Å. This condition at the surface is not even crudely approximated by the adsorption of a single monolayer of oxygen so that the effect of the oxygen layer could in this case be negligibly small. On the other hand, observations on other materials made in this laboratory[66] have indicated that partial quenching of the surface resonance may occur for oxygen coverages in the monolayer range, and the possibility of this effect must not be discounted entirely. In either case, it is clear that Stern and Ferrell's description of the surface coating in terms of a dielectric constant does not apply for monolayer coverages, and one would not apriori expect to observe the decreases in intensity for coverages in this range. A second point concerns the strong increase in the intensity of the elastically reflected primary peak; this increase reflects a strong increase in the probability that electrons incident on the sample would be elastically diffracted. Furthermore, since the changes introduced by oxygen adsorption affect mainly the surface layer, one may conclude that the increased elastic scattering is also associated with the surface. An immediate consequence of this conclusion is that the penetration depth should decrease as explained in Chapter II, and one would then expect an increase in the probability for the excitation of the surface resonance relative to the probability for bulk excitations. Combining these ideas, the total intensity of both bulk and surface plasmon loss peaks should increase with oxygen adsorption because of the increase in the elastically scattered current, and the increase of the surface loss peak should be greater than that of the bulk loss because of decreased penetration arising from higher scattering by the surface layer.

In addition to the bulk and surface plasmon loss peaks measured at 23.5 and 12.5 ev respectively, a third peak is observed at 35 ev which can be explained in terms of the excitations of two plasmons. The relative intensity of this peak decreases with increasing beam voltage in the same manner as that of the surface plasmon. In fact, this peak can be observed only in the range of beam voltages between 100 and 200 volts. Although an interband type transition loss is predicted at 30 ev, the observed behavior suggests that this peak results from the excitation of both a bulk and a surface plasmon. An electron exciting these two resonances would be expected to lose an energy of 36 ev which agrees reasonably well with the measured loss value of 35 ev. Also the relative intensity of a peak representing electrons which have undergone these two losses would be expected to vary with the intensity of either of the two single-loss peaks. The intensity of the bulk plasmon peak does not change strongly in the energy range considered, but it was observed that the double-loss peak and the surface plasmon peak vary correspondingly.

The energy loss values of 43 and 53.5 ev measured for the last two peaks in Fig. 10 agree fairly well with the losses of 45 and 60 ev predicted from Eq. (95). No combinations of the bulk and surface plasmon loss values corresponding to multiple excitations can be used to predict the observed values for these two peaks which are interpreted as representing umklapp transitions. This interpretation is substantiated by the observation of maxima in the true secondary distribution with energies corresponding to lattice electrons ejected from the valence band in the umklapp processes, as discussed in the next section.

The above interpretations of the energy losses measured in this study may be compared with the interpretations made by other authors of the losses for tungsten summarized in Table 1. Harrower's measured loss values[27] were all interpreted by him as representing single-electron excitations. This same interpretation of Harrower's data was applied by Viatskin[53] in his theoretical discussion of the interband type transitions. In neither case were plasmon excitation losses considered. Further, in Harrower's data the same decrease in intensity of his 14.8 ev loss peak was observed as was pointed out here in connection with Figure 11; this effect was not discussed and would not be expected in the case of a single-electron excitation. Powell, Robins and Swan's data[36] were presented without any interpretation, but, in a review of these data, Klemperer and Shepherd[15] compared their 24.3 ev loss with the theoretical value for the bulk plasmon excitation. Possible mechanisms to explain the other loss peaks were not mentioned, although, going back to the data published by Powell et al., one may readily see that their 10.6 ev loss peak exhibits the dependence of intensity on the growth of a surface coating predicted by Stern and Ferrell[20] for the surface plasmon.

It may be noted from Table 1 that there are differences in the energy values of the loss peaks (other than the multiple loss peak) determined in the present work for the clean tungsten surface and those reported by the other authors. These differences may in part be attributed to differences in the measurement schemes employed,[15] and may be partly due to variations in sample surface conditions. In the work of Harrower, secondary electron energy distributions were obtained for electrons reflected from polycrystalline ribbons. These samples were cleaned in vacuum by heating for long periods at temperatures of about 2300°C and flash heating before each measurement to a temperature of about 2100°C. It has been shown using LEED that such heat treatment can result in an ordered accumulation of carbon on and near the surface of the sample. Measurements of energy distributions for the tungsten (110) surface characterized by the carbon contaminated LEED pattern of Fig. 9(a) did not reveal significant shifts in the energy loss values, but measurements by Powell et al., for more severe surface contamination did show variations of several electron volts. In this case polycrystalline wires of tungsten were used, and heat treatment alone was relied upon for cleaning. A further difference in the measurements is that both Powell et al., and Harrower used mainly primary energies in the range of 500 ev and above, whereas measurements reported here are for primary energies in the 100 ev range; at higher incident energies shifts in loss values of less than 2 ev have been observed. Moreover, the fact that their measurements were made at higher incident energies presumably accounts for their not having observed the multiple loss peak due to excitation of both bulk and surface plasmons.

Subsidiary Maxima

Subsidiary maxima in the true secondary region of an electron energy distribution for tungsten are shown in Fig. 13. This curve was obtained for the clean (110) surface bombarded by 130 ev primary electrons. Approximate energy values have been indicated for some of the more prominent peaks which appear superimposed on the large peak due to multiple inelastic processes. These subsidiary maxima may be explained in terms of Auger transitions and umklapp processes.

In an umklapp type transition, an incident electron loses an amount of energy given by Eq. (95), and this energy is transferred to one of the lattice electrons which usually originates in one of the upper lying energy levels. This lattice electron may then be ejected from the solid, and the energy measured in the analyzer would be the energy lost by the primary electron minus the energy required to raise the lattice

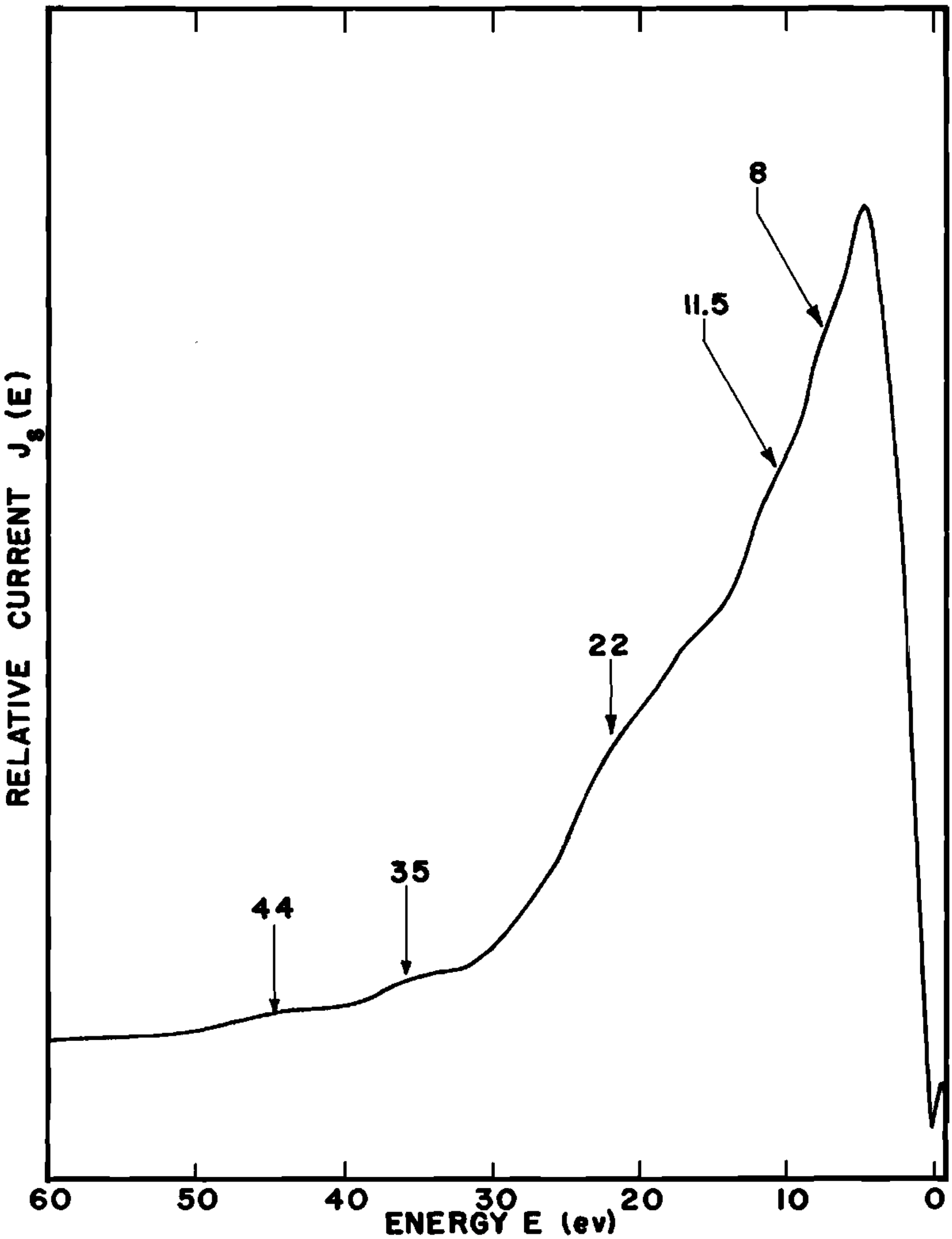

Figure 13. True Secondary Peak for Clean Tungsten (110) Surface Showing Subsidiary Maxima. 130 Volt Primary Electrons.

electron from its initial state to the vacuum level. Energy losses associated with umklapp processes in tungsten were determined in the previous section to be 15, 30, 45 and 60 ev. Experimental losses corresponding to the 45 and 60 ev excitations were observed at 43 and 53.5 ev respectively; the absence of observed single-electron excitation losses corresponding to the 15 and 30 ev values suggests that these excitations either do not occur or that they occur with a relatively lower probability.

Assuming that the lattice electrons originate in the valence band, initial energy levels may be estimated from Mattheiss' band structure calculations for tungsten.[78] His calculations show strong peaks in the density of states at energies of 6.1, 3.9 and 2.3 ev below the Fermi level, or, using a work function of 4.7 ev for the (110) surface,[79] his peaks occur at energies of 10.8, 8.6 and 7.0 ev below the vacuum level. If, for example, an incident electron loses 45 ev to one of the lattice electrons in an umklapp process and if the lattice electron is initially in a state near the center of the distribution predicted by Mattheiss, then the ejected electron would be measured to have an energy of 36.4 ev. Values for the other theoretical losses could be similarly predicted, but a more meaningful prediction is made by considering energy values of umklapp electrons corresponding to the measured loss values. For the measured losses of 43 and 53.5 ev, this gives energy values for the ejected electrons of 34.4 and 44.9 ev respectively; these values compare very well with the measured subsidiary maxima shown in Figure 13 at 35 and 44 ev. Difficulties in applying this interpretation arise from the facts that the band structure calculations are not exact so that the initial levels can not be determined with certainty and, secondly, there is no apriori means of determining which of the peaks in the density of states should be used to represent the initial level of the ejected electron.

Similar difficulties are encountered in attempting to predict the energies of Auger electrons emitted from the solid. In the Auger process, a vacancy is created in one of the lower energy levels by interaction with one of the primary electrons, this vacancy is filled by an electron from one of the upper levels, and the energy is released in the form of an Auger electron emitted from a nearby upper level. The energy measured for the emitted electron, as expressed in Eq. (92), is the de-excitation energy minus the energy required to raise the Auger electron from its initial state to the vacuum level. The electronic structure of tungsten is quite complicated in that there are five energy levels lying less than 75 ev below the vacuum level,[80] not to mention the three strong peaks in the valence band described above. Combinations of these levels may be used to predict Auger electron energies of almost any value desired in the range covered by Fig. 13. In order to restrict the consideration of possible combinations, a detailed analysis of Auger transition probabilities is required, and such an analysis lies beyond the scope and purpose of this discussion. It is, therefore, sufficient to include here a tabulation of some of the combinations of levels which can be used to predict the three Auger peaks indicated in Figure 13.

The difficulty pointed out in the preceeding paragraph may be illustrated by considering the Auger peak at 11.5 ev. This peak can be explained by assuming that an electron is first removed from the 4f 7/2 level in tungsten; this level occurs 28.56 ev below the vacuum level, using atomic energy levels tabulated by Börnstein[80] from x-ray spectra. If this vacancy were filled by an electron from the $(5d6s)_{III}$ peak in Mattheiss' density of states, which is 10.6 ev below the vacuum level, then the de-excitation energy would be 17.96 ev, and an electron ejected from the $(5d6s)_{I}$ level (6.8 ev) would be measured with an energy of 11.16 ev. Alternatively, if the vacancy were created in the 4f 5/2 level (31.28 ev) and filled by an electron from the $(5d6s)_{III}$ level, then an Auger electron emitted from the $(5d6s)_{II}$ level (8.6 ev) would have an energy of 12.08 ev. As may be seen in Fig. 13, the breadth of the 11.5 Auger peak is sufficient to admit both possibilities. The experimental energy values for observed subsidiary maxima and suggested interpretations are summarized in Table 2 for Auger and umklapp processes. Also included in this table are experimental values measured by Harrower,[27] which show generally good agreement with the corresponding losses reported here.

Table 2. Subsidiary Maxima in the Secondary Electron Distribution for Tungsten.

Present Work (ev)	Harrower[27] (ev)	Theoretical (ev)	Transitions
8		7.4	$(4f_{7/2})-2(5d6s)_{III}$
11.5		10.1	$(4f_{5/2})-2(5d6s)_{III}$
		9.4	$(4f_{7/2})-(5d6s)_{III}-(5d6s)_{II}$
		11.2	$(4f_{7/2})-(5d6s)_{III}-(5d6s)_{I}$
		11.6	$(4f_{7/2})-2(5d6s)_{II}$
		12.3	$(4f_{5/2})-(5d6s)_{III}-(5d6s)_{II}$
13.5	13	12.8	$(5p_{3/2})-2(5d6s)_{III}$
		13.4	$(4f_{7/2})-(5d6s)_{II}-(5d6s)_{I}$
		13.9	$(4f_{5/2})-(5d6s)_{III}-(5d6s)_{I}$
		14.5	$(4f_{5/2})-2(5d6s)_{II}$
		15.0	$(4f_{7/2})-2(5d6s)_{I}$
		15.0	$(5p_{3/2})-(5d6s)_{III}-(5d6s)_{II}$

Table 2. Subsidiary Maxima in the Secondary Electron Distribution for Tungsten. (Continued)

Present Work (ev)	Harrower[27] (ev)	Theoretical (ev)	Transitions
18		16.1	$(4f_{5/2})$-$(5d6s)_{II}$-$(5d6s)_{I}$
		16.6	$(5p_{3/2})$-$(5d6s)_{III}$-$(5d6s)_{I}$
		17.2	$(5p_{3/2})$-$2(5d6s)_{II}$
		17.7	$(4f_{5/2})$-$2(5d6s)_{I}$
		18.8	$(5p_{3/2})$-$(5d6s)_{II}$-$(5d6s)_{I}$
22	21.8	20.4	$(5p_{3/2})$-$2(5d6s)_{I}$
		22.3	$(5p_{1/2})$-$2(5d6s)_{III}$
		24.5	$(5p_{1/2})$-$(5d6s)_{III}$-$(5d6s)_{II}$
30		26.1	$(5p_{1/2})$-$(5d6s)_{III}$-$(5d6s)_{I}$
		26.7	$(5p_{1/2})$-$2(5d6s)_{II}$
		28.3	$(5p_{1/2})$-$(5d6s)_{II}$-$(5d6s)_{I}$
		29.9	$(5p_{1/2})$-$(5d6s)_{I}$

Table 2. Subsidiary Maxima in the Secondary Electron Distribution for Tungsten. (Continued)

Present Work (ev)	Harrower[27] (ev)	Theoretical (ev)	Transitions
35	37.8	Umklapp electron from loss at 43 ev	
44	46	Umklapp electron from loss at 53.5 ev	
57		52.2	$(5s_{1/2})-2(5d6s)_{III}$
		54.4	$(5s_{1/2})-(5d6s)_{III}-(5d6s)_{II}$
		56.0	$(5s_{1/2})-(5d6s)_{III}-(5d6s)_{I}$
		56.6	$(5s_{1/2})-2(5d6s)_{II}$
		58.2	$(5s_{1/2})-(5d6s)_{II}-(5d6s)_{I}$
		59.8	$(5s_{1/2})-2(5d6s)_{I}$

It has been observed that the details of the subsidiary maxima in the true secondary distribution are quite sensitive to surface conditions, whereas the characteristic energy loss peaks were by comparison insensitive except in the case of gross surface contamination. The effect of adsorbed oxygen on the subsidiary maxima is shown in Fig. 14; this curve may be compared with the clean tungsten distribution in Fig. 13. The curve of Fig. 14 was obtained for the (110) surface with a monolayer of adsorbed oxygen. A definite peak has appeared at an energy of 7 ev. To show that this peak is characteristic of oxygen adsorbed on the tungsten surface, the inelastic distributions were compared with LEED patterns corresponding to various coverages of oxygen, and it was observed that the intensity of the peak increased with coverage. The significance of this small but definite change in the Auger distribution may be realized by noting, as previously stated, that the LEED patterns for the clean tungsten (110) surface and the surface with a full monolayer of adsorbed oxygen are essentially the same and can not be used to distinguish between the two conditions; the 7 ev peak in the secondary distribution, on the other hand, clearly distinguishes the clean and oxygen covered surfaces and can be used with LEED patterns as an additional criterion for characterizing the tungsten surface.

The interpretation of the oxygen peak in the secondary distribution has been based on the idea of an Auger neutralization of the

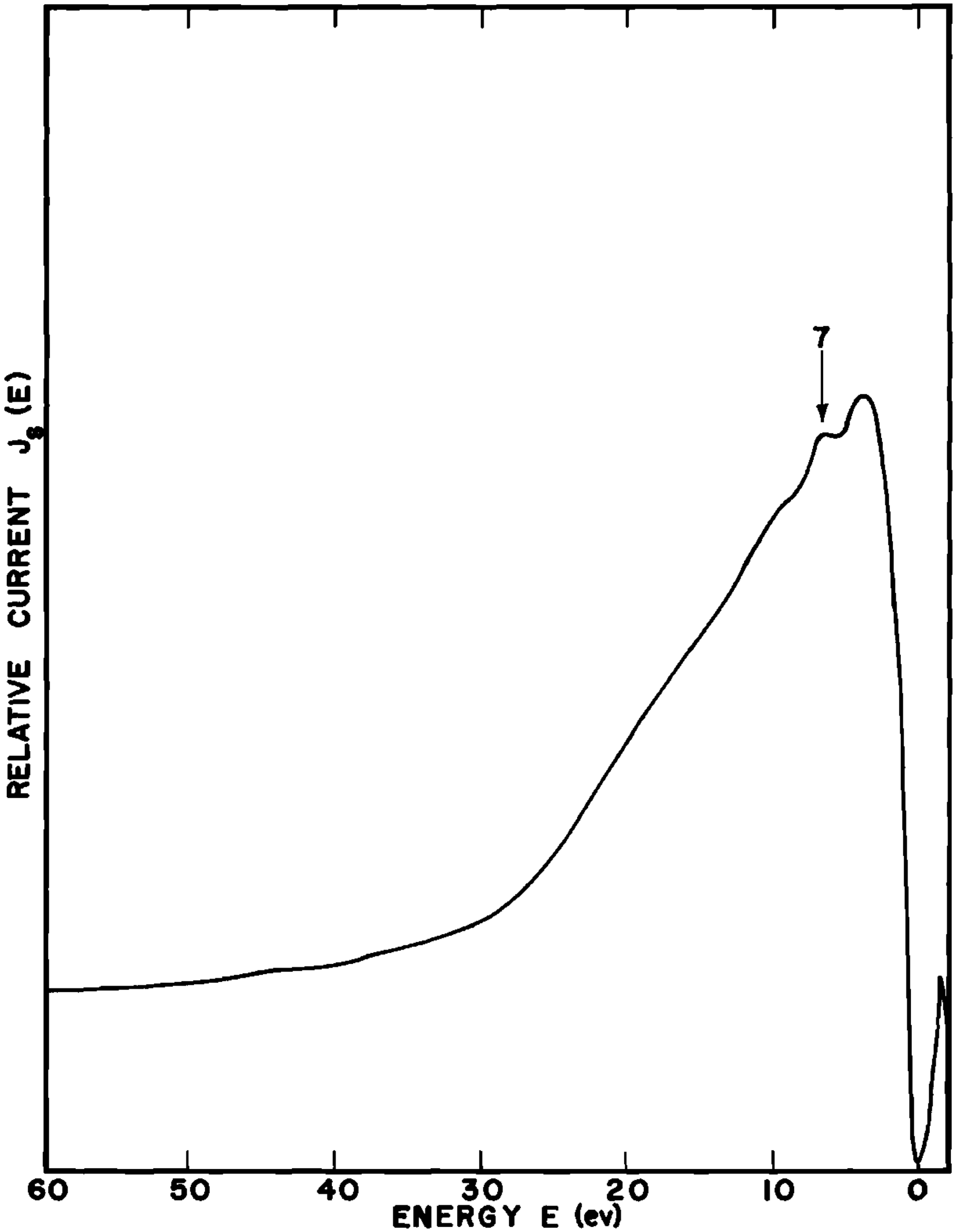

Figure 14. True Secondary Peak for 130 Volt Primary Electrons Showing the Effect of Adsorbed Oxygen on the Subsidiary Maxima.

adsorbed ion as discussed by Hagstrum[31] and as described briefly in Chapter II. This process is similar to Auger emission from the solid except that levels of the oxygen are considered in addition to the tungsten levels for explaining the energies of the emitted electrons. A complication is introduced in that interpretations must involve details of the adsorption bond which have not been considered. These experimental data are thus presented without further explanation for the purpose of demonstrating the sensitivity of these inelastic features to changes in the conditions at the surface.

As already pointed out, the carbon present as a bulk impurity in a new tungsten crystal tends to diffuse toward the surface at elevated temperatures. This results in an ordered layer of carbon on the surface and an accumulation of carbon below the surface. This surface carbon gives rise to a somewhat more pronounced change in the secondary distribution as shown in Fig. 15. This curve was obtained for the (110) surface using 220 volt primary electrons. The presence of the carbon structure is characterized by the LEED pattern included in the figure which was discussed in the previous chapter. The carbon peak in the distribution occurs at 19 ev and completely dominates the true secondary distribution. The surface carbon is effectively removed by exposing the sample to oxygen and heating, but the carbon a few layers below the surface seems to be little disturbed. After the cleaning procedure, the LEED patterns observed are those characteristic of the clean tung-

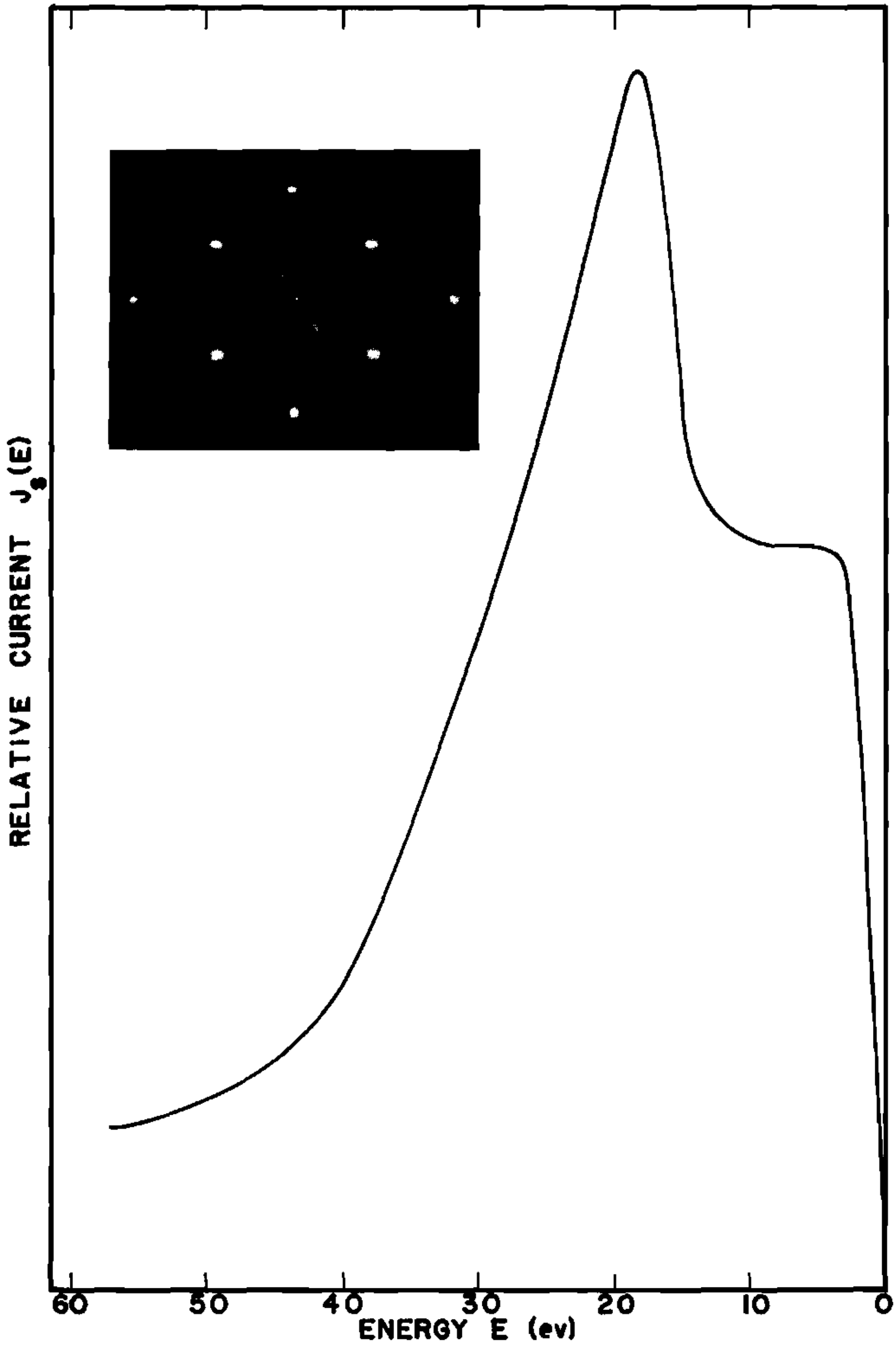

Figure 15. True Secondary Peak Showing the Effect of Surface Carbon Contamination, as Evidenced by the LEED Pattern. 220 Volt Primary Electrons.

sten (110) surface. There are no extra reflections that might indicate the presence of carbon below the surface, even for electron energies as high as 350 ev. One might then conclude that the tungsten lattice near the surface is free of carbon or that the carbon is present but randomly distribution. LEED patterns can not be used to resolve the question.

After repeated cleaning of the tungsten surface by the procedure described in Chapter III, a sequence of energy distributions was obtained for incident beam energies ranging from 50 to 350 ev. The low-energy secondary regions of some of these curves are displayed in Fig. 16. The Auger spectra for incident electrons with energies below 200 ev and the LEED patterns indicated that the surface was clean. However, the steady build up of the 19 ev Auger peak (the peak previously noted to be characteristic of the carbon impurity) with increasing incident electron energy and correspondingly increasing penetration indicates the possibility of considerable carbon several layers below the surface. After extensive heating at temperatures above 2300°C and subsequent cleaning of the surface, the peak at 19 ev disappeared. It is thought that the concentration of carbon was built up by hours of heating to temperatures around 1000°C and that at very high temperatures the carbon diffused to the surface and was removed by exposure to oxygen. The main point to be made is that the Auger distributions could be used to detect the presence of the carbon which did not show up in the LEED patterns, presumably because the carbon was randomly distributed in the tungsten lattice.

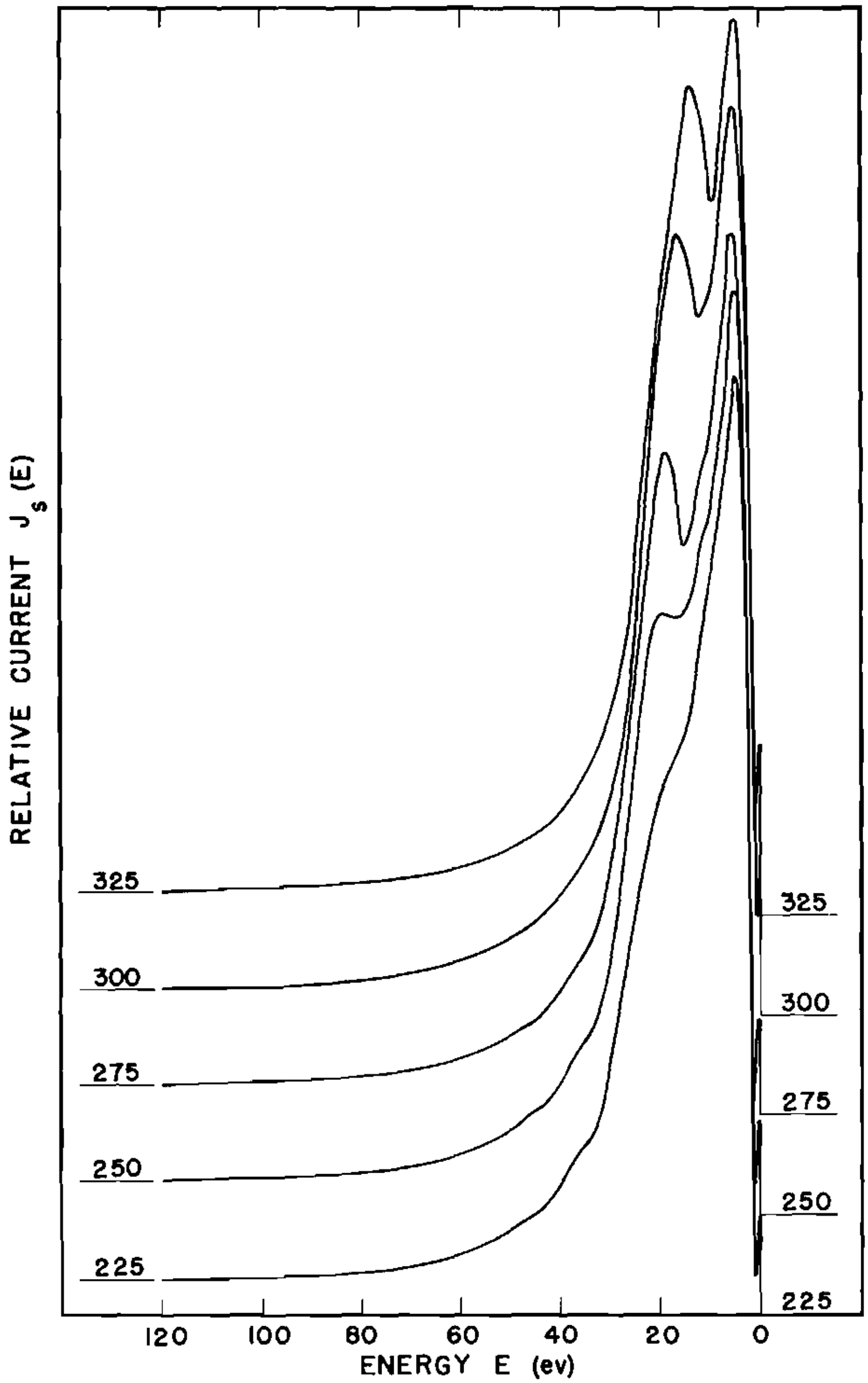

Figure 16. Sequence of True Secondary Energy Distribution Curves Showing Build Up of Auger Peak at 19 ev with Increasing Primary Energy for Tungsten with Carbon near the Surface.

CHAPTER V

CONCLUSIONS AND RECOMMENDATIONS

The main results of this investigation may be summarized as follows. The elastic and inelastic scattering of slow electrons from solid surfaces has been reviewed; the various scattering mechanisms and their interrelationships have been identified with emphasis on the interpretation of experimental data. Apparatus has been developed which can be used to obtain both LEED patterns and secondary electron energy distributions from the same experimental surfaces. LEED patterns from the tungsten (110) surface have been used along with mass spectra for desorbed species to identify previously reported two-dimensional adsorption structures for this surface of tungsten. Features in the secondary electron energy distributions have been explained in terms of collective excitations, umklapp processes and Auger emission. These energy distributions have been compared with LEED patterns corresponding to known adsorption states for the (110) tungsten surface to determine the effects of changes in surface conditions on these distributions. Finally, the Auger distributions have been used to detect impurities on or near the surface which could not be detected by LEED to demonstrate the potential usefulness of the inelastic scattering as a tool for surface studies complementary to LEED. These methods, results and interpretations have also been described in several publications by Tharp and Scheibner.[81-83]

A more quantitative experimental analysis of some features in the energy distributions was precluded by an inherent limitation in energy resolution and by the fact that measurements could not be made at discrete points in the pattern. These problems are currently being overcome in a revised version of the instrumentation which combines with LEED a high-resolution electron spectrometer, and experimental measurements can easily be extended to angular distributions and studies of excitation lifetimes. Other problems which have been suggested during this research and which have not received adequate treatment are mentioned below.

The elastic diffraction of slow electrons has not been described exactly, although explanations of positions of reflections in LEED patterns can frequently be made as discussed above. At present the results of the more recent theoretical developments are not easily accessible to experimentalists because of mathematical complexities and because of a lack of uniformity in notation. A careful review of these methods is needed which perhaps proceeds from simple physical concepts to a coherent development of theoretical models which may not be exact, but which are now recognized as being potentially quite useful for analyzing experimental data.

Rapid advances in the experimental techniques developed in LEED studies and now used to investigate a variety of adsorbate-substrate combinations have been made as indicated by Lander.[8] However, the details of procedures for preparing samples and producing atomically clean surfaces or known adsorption structures are not generally included in publications although these techniques may be of great practical importance.

The connection between the inelastic scattering mechanisms and diffraction intensities for slow electrons has been recognized as significant,[8] but even the more exact treatments[37] consider these inelastic effects only in an average manner as an effective absorption or ignore them entirely. A study in depth of the dependence of diffraction intensities on these inelastic processes would, therefore, be appropriate, particularly in view of the detailed understanding of the inelastic mechanisms which is now being obtained studying surfaces comparable to those used in LEED investigations.

Interband type transitions and plasmon resonances have usually been treated independently, although these processes are for some materials strongly coupled. In such a case the plasmon frequency is shifted significantly because of interband transitions, with the result that interpretations of energy loss data may become quite difficult. This is particularly true for the first transition series metals for which there is no satisfactory theoretical formulation. Interpretations for samples exhibiting this coupling are facilitated by considering the energy loss function obtained from optical reflectivity data. Normally, however, optical data from well defined surfaces are not available, and it would be desirable to make both electron scattering and optical measurements on the same surfaces for comparison. A thorough study of this coupling would require looking at a number of experimental samples selected to display a shifted plasma frequency for known interband transitions; these samples would include metals exhibiting phase transitions, liquid metals and alloys with varying compositions.

The existence of a surface plasmon was first suggested by Ritchie[62] in calculations based on the dielectric model for a metal foil. Further discussion was given by Stern and Ferrell[70] for the case of a surface bounded by a dielectric medium, but most of the theoretical investigations of collective excitations have dealt mainly with bulk plasmons. The dielectric theory is important because it brings together the plasmon excitations and interband transitions. However, the agreement of theoretical predictions for the surface plasmon with experimental data is at best qualitative, and a more exact description of this surface effect is needed.

Interband transitions occur in which momentum is conserved in the two-body interaction with electrons in a particular band excited to unoccupied levels in the same band or in higher lying bands in any of the Brillouin zones. Similar transitions, designated as umklapp processes, also occur in which momentum is not conserved in the two-body interaction; rather, there is an exchange of momentum with the lattice as a whole, and the momentum conservation law includes the reciprocal lattice vector. These two different classes of transitions are not generally differentiated in experimental data, although details of the scattered distributions should be quite different for the two cases. Clarifying the distinction between these processes would require careful measurements of the angular distributions of scattered intensities. These measurements would also be useful for exploring some aspects of the band structure of the samples considered.

In the case of back-reflection type scattering experiments, it has been shown that two scattering events are usually required in order for those electrons undergoing characteristic losses to be detected. The sequence of these scattering events can have a pronounced effect on the angular distribution of the collected electrons and can be determined readily by careful measurements of these distributions.

In measurements of characteristic losses for high-energy electrons the problem of excitation threshold is not encountered. Moreover, theoretical calculations of excitation probabilities for these processes do not take such a threshold for excitation into account. However, for low-energy incident electrons, a threshold is observed, and the theories must be extended to described this effect.

Other energy losses which may be important in describing the scattering of slow electrons include electron-phonon interactions and electron excitations of vibrational states of gases adsorbed on the surface. The latter excitations, which have been reported by Propst,[84] are important as a possible means of chracterizing the surface with regard to the nature of adsorbed species.

The distribution of secondary electrons emitted from the solid as a result of multiple inelastic processes has been much discussed, but contributions to these distributions resulting from bulk and surface plasmon resonances have not generally been included. Therefore, a theoretical summary of these contributions and careful measurements of energy and angular distributions for slow incident electrons should be carried out for metals and semiconductors.

Discrete processes giving rise to subsidiary maxima in the secondary distribution have been explained qualitatively. These maxima include electrons emitted as a result of umklapp processes and Auger electrons; the latter are particularly significant because of the connection with transition densities in the solid.

In the preparation of this dissertation, several aspects of the electron scattering problem were surveyed, and the usefulness of electron scattering as a tool for surface studies was demonstrated. However, many theoretical and experimental problems remain, and research in the areas suggested above would serve to further clarify the nature of electron interactions with solids.

APPENDIX A

THE COMPLEX DIELECTRIC CONSTANT

The interaction of charged particles with a degenerate electron gas can be treated by considering the complex dielectric constant of such a system as discussed by Lindhard,[69] Hubbard[60] and Ritchie.[85] Because of the importance of the frequency- and wavevector-dependent complex dielectric constant to the present work, a derivation of this quantity is presented below. Following Ritchie's development, the solid is treated as a neutral plasma, consisting of a uniform positive background (corresponding to the ion cores) and a gas of electrons moving in a common electric field to which they all give rise.

The wave equation of a system of electrons and an incident particle of charge + Ze can be written

$$\mathcal{H}\Psi = \left\{ \frac{-\hbar^2}{2m} \sum_i \nabla_i^2 - \frac{\hbar^2}{2M} \nabla_R^2 + \frac{e^2}{2} \sum_{i \neq j}\sum \frac{1}{|\bar{r}_i - \bar{r}_j|} \right. \tag{A-1}$$

$$\left. - Ze^2 \sum_i \frac{1}{|\bar{R} - \bar{r}_i|} \right\} \Psi = i\hbar \frac{\partial}{\partial t} \Psi ,$$

where $\bar{r}_i$, m and $\bar{R}$, M are the position vectors and masses of the ith electron and incident particle respectively. In writing this Hamiltonian, the electric charge neutrality of the solid has been taken into account.[57] Assume that the system wave function Ψ can be expressed as a product of the individual particle wave functions,

$$\Psi = \psi_R(\bar{R}, t)\ \Pi_i \psi_i(\bar{r}_i, t) \quad . \tag{A-2}$$

From Eq. (A-1) note that Ψ is separable in its spacial and time dependence so that this equation can be written

$$\mathcal{H}\Psi = E\Psi , \tag{A-3}$$

with Ψ depending only on spacial variables. Assume further that the spacial part of Ψ can be written as a product of the form (A-2) with only spacial parts of the single-particle functions considered. The Hartree equations can now be obtained by applying the variational principal to the Hamiltonian of Eq. (A-1) and requiring that these wave functions be such as to make the average energy stationary.[86]

The average value of the Hamiltonian is given by

$$\langle \mathcal{H} \rangle = \int \Psi^* \mathcal{H} \Psi \, dv \, . \tag{A-4}$$

The integration is over the spacial coordinates of all particles. Evaluating term by term one gets

$$\langle \mathcal{H} \rangle = \sum_i \int \psi_i^* f_i \psi_i d\bar{r}_i + 1/2 \sum_{i \neq j} \sum \int \int \psi_i^* \psi_j^* g_{ij} \psi_j \psi_i d\bar{r}_j d\bar{r}_i \tag{A-5}$$

$$+ \int \psi_R^* \left(- \frac{\hbar^2}{2m} \nabla_R^2 \right) \psi_R d\bar{R} ,$$

where f_i and g_{ij} are defined by the equations

$$f_i = - \frac{\hbar^2}{2m} \nabla_i^2 - Ze^2 \int \frac{|\psi_R|^2}{|\bar{R} - \bar{r}_i|} d\bar{R} , \tag{A-6a}$$

$$g_{ij} = \frac{e^2}{|\bar{r}_i - \bar{r}_j|} . \tag{A-6b}$$

Define the function I by

$$I = \langle \mathcal{H} \rangle - \sum_i \lambda_i \langle \psi_i | \psi_i \rangle , \tag{A-7}$$

the λ's being the undetermined multipliers. The variational principle is now applied to I, requiring

$$\delta I = I(\psi_i + \delta\psi_i) - I(\psi_i) = 0 . \tag{A-8}$$

This guarantees stationary values of $\langle \mathcal{H} \rangle$ and maintains normalized wave functions under the variation. Consider the case of $\delta\psi_i = 0$, $i \neq \ell$ and $\delta\psi_\ell \neq 0$. Making the proper substitutions one obtains

$$\delta I = \int \delta\psi_\ell^* (f_\ell - \lambda_\ell)\psi_\ell d\bar{r}_\ell + \int \psi_\ell^* (f_\ell - \lambda_\ell)\delta\psi_\ell d\bar{r}_\ell \tag{A-9}$$

$$+ \sum_{j \neq \ell} \int\int \delta\psi_\ell^* \psi_j^* g_{\ell j} \psi_j \psi_\ell d\bar{r}_j d\bar{r}_\ell$$

$$+ \sum_{j \neq \ell} \int\int \psi_\ell^* \psi_j^* g_{\ell j} \psi_j \delta\psi_\ell d\bar{r}_j d\bar{r}_\ell = 0 .$$

Using Hermitian property of f_ℓ, this equation can be written

$$\delta I = \int \delta\psi_\ell^* \left\{ (f_\ell - \lambda_\ell) + \sum_{j \neq \ell} \int \psi_j^* g_{\ell j} \psi_j d\bar{r}_j \right\} \psi_\ell d\bar{r}_\ell \tag{A-10}$$

$$+ \text{ complex conjugate} = 0 .$$

As the variation $\delta\psi_\ell^*$ is arbitrary, this last equation is satisfied by setting the part written explicitly equal to zero, in which case the complex conjugate is also zero. Finally, for arbitrary $\delta\psi_\ell^*$, the value of the integral is zero only if the integrand vanishes at every point, and one has

$$\left\{ -\frac{\hbar^2}{2m}\nabla_\ell^2 + e^2\sum_{j\neq\ell}\int \frac{|\psi_j|^2}{|\bar{r}_\ell - \bar{r}_j|}\,d\bar{r}_j - Ze^2\int \frac{|\psi_R|^2}{|\bar{r}_\ell - \bar{R}|}\,d\bar{R} \right\}\psi_\ell = \lambda_\ell\psi_\ell \,. \tag{A-11}$$

These are the Hartree equations, with one such equation for each value of ℓ. The undetermined multipliers λ_ℓ have the form of energy eigenvalues for single-particle states. However, it should be noted that the λ_ℓ's are not measurable quantities and that a sum of the λ_ℓ's over all particles is much larger than the true system energy.[87] In any case, the ψ_ℓ's can be treated as separable functions in space and time, and Eq. (A-11) can be written

$$\left\{ -\frac{\hbar^2}{2m}\nabla_\ell^2 + e^2\sum_{j\neq\ell}\int \frac{|\psi_j|^2}{|\bar{r}_\ell - \bar{r}_j|}\,d\bar{r}_j - Ze^2\int \frac{|\psi_R|^2}{|\bar{r}_\ell - \bar{R}|}\,d\bar{R} \right\}\psi_\ell = i\hbar\frac{\partial}{\partial t}\psi_\ell \,, \tag{A-12}$$

where $\psi_\ell(\bar{r}_\ell, t) = \psi_\ell(\bar{r}_\ell)\exp(-i\lambda_\ell t/\hbar)$.

Define the potential Φ_ℓ by

$$\Phi_\ell(\bar{r}_\ell, t) = -e \sum_{j \neq \ell} \int \frac{|\psi_j|^2}{|\bar{r}_\ell - \bar{r}_j|} d\bar{r}_j + Ze \int \frac{|\psi_R|^2}{|\bar{R} - \bar{r}_\ell|} d\bar{R} . \tag{A-13}$$

Equation (A-12) can now be written

$$\left\{ -\frac{\hbar^2}{2m} \nabla_\ell^2 - e\Phi_\ell(\bar{r}_\ell, t) \right\} \psi_\ell(r_\ell, t) = i\hbar \frac{\partial}{\partial t} \psi_\ell(\bar{r}_\ell, t) . \tag{A-14}$$

Note that Φ_ℓ satisfies the Poisson's equation

$$\nabla_\ell^2 \Phi_\ell(\bar{r}_\ell, t) = 4\pi e \sum_{j \neq \ell} |\psi_j|^2_{\bar{r}_j = \bar{r}_\ell} - 4\pi Ze |\psi_R|^2_{\bar{R} = \bar{r}_\ell} , \tag{A-15}$$

as can be shown directly using the relationship

$$\nabla^2 \frac{1}{|\bar{X} - \bar{X}'|} = -4\pi \delta(\bar{X} - \bar{X}') . \tag{A-16}$$

Φ_ℓ is the self-consistent potential acting on the ℓth electron and is expressed as that solution of Poisson's equation which arises from the charge densities of all electrons in the medium except the ℓ th electron itself. It is desired, however, to have a single potential in which all particles move and to which they all give rise, and the effect of the ℓ th electron on itself must therefore be included. The field thus obtained is correct only in as much as the addition of one electron to a system in which the average electron density is $\sim 10^{23}$ electrons per cm^3 should not appreciably change the self-consistent potential.[85] Dropping the subscript ℓ and allowing the sum to include the ℓ th electron, Equation (A-15) becomes

$$\nabla^2 \Phi_{(\bar{r}, t)} = 4\pi e \sum_j |\psi_j|^2 - 4\pi Ze |\psi_R|^2 . \tag{A-17}$$

In this last expression the functions ψ_j and ψ_R are evaluated at the point $\bar{r}$.

Consider the Fourier expansion of an arbitrary function of space and time given by

$$f(\bar{r}, t) = \sum_{\bar{k}} \sum_{\omega} f_{\bar{k}, \omega} e^{i(\bar{k} \cdot \bar{r} + \omega t)} , \tag{A-18a}$$

$$\text{with } f_{\bar{k}, \omega} = \frac{1}{L^3 T} \int \int f(\bar{r}, t) e^{-i(\bar{k} \cdot \bar{r} + \omega t)} d\bar{r} \, dt . \tag{A-18b}$$

$f(\bar{r}, t)$ is assumed to be defined in a large cube of side L and in a time T long compared with electronic periods to be considered. Equation (A-17) can then be written in the Fourier representation as

$$k^2 \Phi_{\bar{k},\omega} = -4\pi e \sum_j |\psi_j|^2_{\bar{k},\omega} + 4\pi Ze |\psi_R|^2_{\bar{k},\omega} \cdot \qquad \text{(A-19)}$$

Noting that the term $\rho = -e \sum |\psi_j|^2_{\bar{k},\omega}$ represents a polarization charge density related to the electric field in the plasma, the frequency- and wavevector-dependent complex dielectric constant can be defined in direct analogy with classical ideas* by the equation

$$\epsilon_{\bar{k},\omega} k^2 \Phi_{\bar{k},\omega} = 4\pi Ze |\psi_R|^2_{\bar{k},\omega} . \qquad \text{(A-20)}$$

It should be pointed out that, although the complex dielectric constant exhibits a direct dependence on $\bar{k}$ and ω, the dependence on the related real space-time variables is not generally obvious, making Fourier space the natural space of definition for this quantity. Combining Eqs. (A-19) and (A-20) one obtains the result

---

*The polarization charge density is derived from the induced polarization $\bar{P}$; $\rho = -\nabla \cdot \bar{P}$. As usual, $\bar{P}$ is assumed proportional to the electric field E, which, in turn, is related to the potential Φ. Thus, $\bar{P} = -\chi \nabla \Phi$ and $\rho = \chi \nabla^2 \Phi$, where χ is the electric susceptibility. Finally, in the Fourier representation one has $\rho_{\bar{k},\omega} = -\chi k^2 \Phi_{\bar{k},\omega}$ making Eq. (A-20) obvious for ϵ and χ related by $\epsilon = 1 + 4\pi\chi$.

$$(\epsilon_{\bar{k},\omega} - 1)\, k^2\, \Phi_{\bar{k},\omega} = 4\pi e \sum_j |\psi_j|^2_{\bar{k},\omega} \,. \qquad \text{(A-21)}$$

This equation can be solved for $\epsilon_{\bar{k},\omega}$ by first expanding the single-particle wave functions ψ_j in terms of free-particle eigenfunctions and evaluating the expansion coefficients to first-order using time-dependent perturbation theory.

Assume the expansion

$$\psi_j(\bar{r}, t) = \frac{1}{\sqrt{V}} \sum_\ell f_\ell(t)\, e^{i(\bar{k}_\ell \cdot \bar{r} - \omega_\ell t)} \,. \qquad \text{(A-22)}$$

The Hartree equation is then written

$$\left\{ -\frac{\hbar^2}{2m} \nabla^2 - \lambda e\, \Phi(\bar{r}, t)\, e^{\gamma t} \right\} \psi_j(\bar{r}, t) = i\hbar \frac{\partial}{\partial t} \psi_j(\bar{r}, t) \,, \qquad \text{(A-23)}$$

where the term $e^{\gamma t}$ (γ a small positive constant) has the effect of turning on the perturbation interaction Φ. Substituting the expansion for ψ_j into Eq. (A-23) one gets

$$i\hbar \sum_\ell \dot{f}_\ell\, e^{i(\bar{k}_\ell \cdot \bar{r} - \omega_\ell t)} = -\lambda \sum_\ell e \Phi\, e^{\gamma t} f_\ell\, e^{i(\bar{k}_\ell \cdot \bar{r} - \omega_\ell t)} \,. \qquad \text{(A-24)}$$

The potential $\Phi(\bar{r},t)$ can be written

$$\Phi(\bar{r},t) = \sum_{\bar{k}'}\sum_{\omega'} \Phi_{\bar{k}',\omega'}\, e^{i(\bar{k}'\cdot\bar{r} + \omega' t)} . \tag{A-25}$$

Using this expression for Φ, multiplying Eq. (A-24) through by $e^{-i\bar{k}_m\cdot\bar{r}}$ and integrating both sides over the volume V, one obtains

$$\dot{f}_m = -\frac{\lambda}{i\hbar}\sum_{\ell}\sum_{\omega'} f_\ell\, e\,\Phi_{\bar{k}_m - \bar{k}_\ell,\,\omega'}\, e^{i(\omega_m - \omega_\ell + \omega' - i\gamma)t} . \tag{A-26}$$

Now consider the usual expansion for f_ℓ,

$$f_\ell = \sum_{s=0}^{\infty} f_\ell^{(s)}\lambda^s . \tag{A-27}$$

Equation (A-26) becomes

$$\sum_s \dot{f}_m^{(s)}\lambda^s = -\frac{\lambda}{i\hbar}\sum_s\sum_\ell\sum_{\omega'} f_\ell^{(s)}\lambda^s\, e\,\Phi_{\bar{k}_m - \bar{k}_\ell,\,\omega'}\, e^{i(\omega_m - \omega_\ell + \omega' - i\gamma)t} . \tag{A-28}$$

Taking only terms not involving λ one finds $\dot{f}_\ell^{(0)} = 0$; assuming the system to be initially in a state "j" characterized by wavevector $\bar{k}_j$ and frequency ω_j one can write $f_\ell^{(0)} = \delta_{j\ell}$. The terms involving λ to the first power then give

$$\dot{f}_\ell^{(1)} = -\frac{1}{i\hbar} \sum_{\omega'} e\,\Phi_{\bar{k}_\ell - \bar{k}_j,\ \omega'}\ e^{i(\omega_\ell - \omega_j + \omega' - i\gamma)t} . \qquad \text{(A-29)}$$

This equation can now be solved for $f_\ell^{(1)}$ by integrating over the time variable. The limits of integration are chosen to be $-\infty$ and t, as the term $e^{\gamma t}$ forces the perturbation to disappear at $t = -\infty$. The result obtained is

$$f_\ell^{(1)} = \sum_{\omega'} \frac{e\ \Phi_{\bar{k}_\ell - \bar{k}_j,\ \omega'}\ e^{i(\omega_\ell - \omega_j + \omega')t}}{E_\ell - E_j + \hbar\,(\omega' - i\gamma)} , \qquad \text{(A-30)}$$

where γ has now been neglected in the exponential and $\hbar\,\omega_\ell$ and $\hbar\,\omega_j$ have been replaced by the free-electron energies which depend on the respective wavevectors $\bar{k}_\ell$ and $\bar{k}_j$. Recalling that $f_\ell = f_\ell^{(0)} + \lambda f_\ell^{(1)} + ---$, ψ_j can be expressed to first order as

$$\psi_j = \frac{1}{\sqrt{V}} \left\{ e^{i(\bar{k}_j \cdot \bar{r} - \omega_j t)} + \lambda \sum_\ell \sum_{\omega'} \frac{e\Phi_{\bar{k}_\ell - \bar{k}_j,\ \omega'}\ e^{i[\bar{k}_\ell \cdot \bar{r} - (\omega_j - \omega')t]}}{E_\ell - E_j + \hbar(\omega' - i\gamma)} \right\}$$

(A-31)

Having obtained ψ_j, it is possible to complete the calculation of $\epsilon_{\bar{k},\omega}$ using Eq. (A-21). The probability density for the jth electron $|\psi_j|^2$ is given by

$$|\psi_j|^2 = \frac{1}{V}\left\{1 + \lambda \sum_{\ell}\sum_{\omega'}\left[\frac{e\Phi_{\bar{k}_\ell - \bar{k}_j,\omega'}\, e^{i(\bar{k}_\ell - \bar{k}_j)\cdot\bar{r}}\, e^{+i\omega' t}}{E_\ell - E_j + \hbar(\omega' - i\gamma)}\right.\right. \tag{A-32}$$

$$\left.\left. + \frac{e\Phi^{*}_{\bar{k}_\ell - \bar{k}_j,\omega'}\, e^{-i(\bar{k}_\ell - \bar{k}_j)\cdot\bar{r}}\, e^{-i\omega' t}}{E_\ell - E_j + \hbar(\omega' + i\gamma)}\right]\right\} .$$

In this expression the terms involving λ^2 have been neglected, and λ is henceforth set equal to unity. The $\bar{k},\omega$ component of $|\psi_j|^2$ can now be evaluated directly using the definition (A-18b) and the orthogonality of the free-electron eigenfunctions.

$$|\psi_j|^2_{\bar{k},\omega} = \frac{1}{V}\left\{\frac{e\Phi_{\bar{k},\omega}}{E(\bar{k}_j + \bar{k}) - E(\bar{k}_j) + \hbar(\omega - i\gamma)} + \frac{e\Phi^{*}_{-\bar{k},-\omega}}{E(\bar{k}_j - \bar{k}) - E(\bar{k}_j) - \hbar(\omega - i\gamma)}\right\}$$

(A-33)

Noting that $\Phi^{*}_{-\bar{k},-\omega} = \Phi_{\bar{k},\omega}$ one can write

$$|\psi_j|^2_{\bar{k},\omega} = \frac{2me\,\Phi_{\bar{k},\omega}}{\hbar^2 V}\left\{\frac{1}{k^2+2\bar{k}\cdot\bar{k}_j+\frac{2m}{\hbar}(\omega-i\gamma)} + \frac{1}{k^2-2\bar{k}\cdot\bar{k}_j-\frac{2m}{\hbar}(\omega-i\gamma)}\right\}. \tag{A-34}$$

Summing over all electrons and substituting into Eq. (A-21), the complex dielectric constant can be written

$$\epsilon_{\bar{k},\omega} = 1 + \frac{8\pi me^2}{\hbar^2k^2V}\sum_j\left\{\frac{1}{k^2+2\bar{k}\cdot\bar{k}_j+\frac{2m}{\hbar}(\omega-i\gamma)} + \frac{1}{k^2-2\bar{k}\cdot\bar{k}_j-\frac{2m}{\hbar}(\omega-i\gamma)}\right\}. \tag{A-35}$$

Replacing the sum over particles by a sum over states and defining $F(E_n)$ to be the normalized density of states in the undisturbed plasma, one finally gets

$$\epsilon_{\bar{k},\omega} = 1 + \frac{2m^2\omega_p^2}{\hbar^2 k^2}\sum_n F(E_n)\left\{\frac{1}{k^2+2\bar{k}\cdot\bar{k}_n+\frac{2m}{\hbar}(\omega-i\gamma)} + \frac{1}{k^2-2\bar{k}\cdot\bar{k}_n-\frac{2m}{\hbar}(\omega-i\gamma)}\right\} \tag{A-36}$$

where ω_p is the classical oscillation frequency of the gas given by

$$\omega_p^2 = \frac{4\pi e^2 N}{mV} \quad . \tag{A-37}$$

This result for the complex dielectric constant is the same as that obtained by Lindhard,[69] and except for notational differences it is identical to Ritchie's expression.[85] The dielectric constant thus calculated has the property that it may be employed for any value of the wavevector $\bar{k}$ and is capable of describing both the collective properties of the electron gas and the properties of the individual electrons in the gas.

BIBLIOGRAPHY*

1. L. H. Germer, Physics Today 17, 19 (July 1964).

2. C. J. Davisson and L. H. Germer, Phys. Rev. 30, 705 (1927).

3. H. E. Farnsworth, Phys. Rev. 40, 684 (1932); numerous publications since 1932.

4. W. Ehrenberg, Phil. Mag. 18, 878 (1934).

5. E. J. Scheibner, L. H. Germer and C. D. Hartman, Rev. Sci. Instr. 31, 112 (1960).

6. L. H. Germer and C. D. Hartman, Rev. Sci. Instr. 31, 784 (1960).

7. J. J. Lander, F. C. Unterwald, J. Morrison, Rev. Sci. Instr. 33, 782 (1962).

8. J. J. Lander, in Progress in Solid State Chemistry, Vol. 2, p. 26, Pergamon Press, New York, 1965.

9. L. Austin and H. Starke, Ann. Physik 9, 271 (1902).

10. K. G. McKay, Advances in Electronics 1, 65 (1948).

11. H. Bruining, Physics and Applications of Secondary Electron Emission, McGraw-Hill, New York, 1954.

12. L. Marton, L. B. Leder and H. Mendlowitz, Advances in Electronics and Electron Physics 11, 183 (1955).

13. R. Kollath, in Encyclopedia of Physics, Vol. 21, p. 232, Springer, Berlin, 1956.

14. A. J. Dekker, in Solid State Physics, Vol. 6, p. 251, Academic Press, Inc., New York, 1958.

---

*Abbreviations herein follow the form recommended by the American Institute of Physics.

15. O. Klemperer and J. P. G. Shepherd, Advances in Physics 12, 355 (1963).

16. J. A. Becker, Phys. Rev. 23, 664 (1924).

17. E. Rudberg, Proc. Roy. Soc. A127, 111 (1930).

18. E. Rudberg, Phys. Rev. 50, 138 (1936).

19. G. Ruthemann, Ann. Physik 2, 113 (1948).

20. L. Marton, Phys. Rev. 66, 159 (1944).

21. J. Hillier and R. F. Baker, J. Appl. Phys. 15, 663 (1944).

22. G. Möllenstedt, Optik 9, 499 (1949).

23. L. J. Hayworth, Phys. Rev. 48, 88 (1935); 50, 216 (1936).

24. O. Hachenberg and W. Brauer, Advances in Electronics and Electron Physics 11, 413 (1959).

25. R. Kollath, Ann. Physik 1, 357 (1947).

26. J. J. Lander, Phys. Rev. 91, 1382 (1953).

27. G. A. Harrower, Phys. Rev. 102, 340 (1956); 104, 52 (1956).

28. L. B. Leder and J. A. Simpson, Rev. Sci. Instr. 29, 571 (1958).

29. W. E. Spicer and C. N. Berglund, Rev. Sci. Instr. 35, 1665 (1964).

30. J. A. Becker, in Solid State Physics, Vol. 7, p. 379, Academic Press, Inc., New York, 1958.

31. H. D. Hagstrum, Phys. Rev. 96, 336 (1954).

32. L. H. Germer, R. M. Stern and A. U. MacRae, Metal Surfaces, ed. by W. D. Robertson and N. A. Gjostein (A.S.M. Ohio, 1963) p. 287.

33. R. M. Stern, Appl. Phys. Letters 5, 218 (1964).

34. J. W. May, L. H. Germer and C. C. Chang, J. Chem. Phys. 45, 2383 (1966).

35. J. Anderson and P. J. Estrup, J. Chem. Phys. 46, 563, 567 (1967).

36. C. J. Powell, J. L. Robins and J. B. Swan, Phys. Rev. 110, 657 (1958).

37. E. G. McRae, J. Chem. Phys. 45, 3258 (1966).

38. S. Miyake and K. Hayakawa, J. Phys. Soc. Japan 21, 363 (1966).

39. R. D. Heidenreich, Fundamentals of Transmission Electron Microscopy, Interscience Publishers, New York, 1964.

40. E. A. Wood, J. Appl. Phys. 35, 1306 (1964).

41. P. W. Palmberg and W. T. Peria, Surface Sci. 6, 57 (1967).

42. K. Hirabayashi and Y. Takeishi, Surface Sci. 4, 150 (1966).

43. M. von Laue, Phys. Rev. 37, 53 (1931).

44. M. Lax, Rev. Mod. Phys. 23, 287 (1951); Phys. Rev. 85, 621 (1952).

45. H. S. W. Massey and E. Burhop, Electronic and Ionic Impact Phenomena, Oxford University Press, New York, 1952, 2nd ed.

46. S. Raimes, Research 9, 374 (1956); Reports on Progress in Physics 20, 1 (1957).

47. H. Fröhlich, Ann. Physik 13, 229 (1932).

48. E. Rudberg and J. C. Slater, Phys. Rev. 50, 150 (1936); see also references 17 and 18.

49. D. E. Wooldridge, Phys. Rev. 56, 562 (1939).

50. A. J. Dekker and A. van der Ziel, Phys. Rev. 86, 755 (1952).

51. A. van der Ziel, Phys. Rev. 92, 35 (1953).

52. E. M. Baroody, Phys. Rev. 101, 1679 (1956).

53. A. Ia. Viatskin, Soviet Phys. Technical Phys. 3, 2038, 2252 (1958).

54. H. Bethe, Ann. Physik 5, 325 (1930).

55. C. Kittel, Introduction to Solid State Physics, John Wiley and Sons, Inc., New York, 1967, Third edition; see especially p. 63.

56. L. I. Schiff, Quantum Mechanics, McGraw-Hill Book Company, Inc., New York, 1955; see especially pp. 197-198.

57. D. Bohm and D. Pines, Phys. Rev. 82, 625 (1951); 85, 338 (1952); 92, 609 (1953); D. Pines, Phys. Rev. 92, 626 (1953).

58. D. Pines, Rev. Mod. Phys. 28, 184 (1956).

59. P. Nozièrs and D. Pines, Phys. Rev. 109, 741, 762 (1958); 113, 1254 (1959).

60. J. Hubbard, Proc. Phys. Soc. A, 67, 1058; 68, 441, 976 (1955).

61. J. Neufield and R. H. Ritchie, Phys. Rev. 98, 1632 (1955).

62. R. H. Ritchie, Phys. Rev. 106, 874 (1957).

63. E. J. Williams, Kgl. Danske Videnskab, Mat.-fys. Medd. 13 (1935).

64. J. D. Jackson, Classical Electrodynamics, John Wiley & Sons, Inc., New York, 1962; see especially p. 47.

65. H. Raether, in Springer Tracts in Modern Physics, Vol. 38, p. 84, Springer-Verlag, New York, 1965.

66. L. K. Jordan and E. J. Scheibner, Surface Sci. 5, 57 (1968).

67. Reference 64; see especially p. 311.

68. F. Bloch, Z. Physik 81, 363 (1933); Helv. Phys. Acta I, 385 (1934).

69. J. Lindhard, Kgl. Danske Videnskab. Selskab, Mat.-fys. Medd. 28, No. 8 (1954).

70. E. A. Stern and R. A. Ferrell, Phys. Rev. 120, 130 (1960).

71. G. F. Amelio and E. J. Scheibner, Surface Sci., to be published.

72. G. F. Amelio, J. Math. Phys., to be published.

73. G. F. Amelio, Ph.D. Thesis, to be submitted, Dept. of Phys., Georgia Institute of Technology.

74. O. H. Zinke, Phys. Rev. 106, 1163 (1957).

75. J. A. Simpson, Rev. Sci. Instr. 32, 1283 (1961).

76. W. L. Bond, J. Sci. Instr. 38, 63 (1961).

77. A. Schrader, Ätzheft, Gebrüder Borntraeger, Berlin, 1957.

78. L. F. Mattheiss, Phys. Rev. 139, 1893 (1965).

79. American Institute of Physics Handbook, McGraw-Hill Book Co., Inc., New York, 1963, p. 9-152.

80. Reference 79; see p. 7-138.

81. L. N. Tharp and E. J. Scheibner, J. Appl. Phys. 38, 3320 (1967).

82. E. J. Scheibner and L. N. Tharp, Surface Sci. 8, 247 (1967).

83. L. N. Tharp, E. J. Scheibner and R. P. Woodward, Rev. Sci. Instr.; to be published.

84. F. M. Propst and T. C. Piper; to be published.

85. R. H. Ritchie, Phys. Rev. 114, 644 (1959).

86. J. C. Slater, Quantum Theory of Molecules and Solids (Vol. I), McGraw-Hill Book Co., Inc., New York, 1963; see especially Appendix 4.

87. S. Raimes, The Wave Mechanics of Electrons in Metals, North Holland Publishing Co., Amsterdam, 1963; see especially Chapter 4, p. 103.

VITA

Lester Neal Tharp was born August 4, 1941 in McRae, Georgia, the son of Mr. and Mrs. O. N. Tharp. In March, 1962 he married the former Cynthia Ann Knapp of Atlanta, Georgia; they have three children.

Mr. Tharp attended the McRae-Helena Elementary School and Telfair County High School. He entered the Georgia Institute of Technology in 1959; he received the B.S. degree in Physics in 1963 and the M.S. degree in Physics in 1965.

While an undergraduate, Mr. Tharp was employed by the Engineering Experiment Station of the Georgia Institute of Technology as a Student Assistant. In July, 1963 he became a Graduate Research Assistant, and in July, 1966 he was appointed to the staff as a Research Physicist.

He is a member of Sigma Pi Sigma, Pi Mu Epsilon, Phi Kappa Phi, and Sigma Xi.